



University of Evora

ARCHMAT

(ERASMUS MUNDUS MASTER IN ARCHaeological MATerials Science)

A multi-analytical protocol combining EDXRF, SEM+EDS, μ XRD and Monte Carlo simulations applied to analyse non-destructively Portuguese corroded copper coins

E. Güncem Diktaş, 36190

Nick Schiavon, University of Evora
(Supervisor)



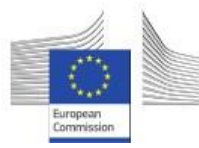
Antonio Brunetti, Università degli Studi di Sassari
(Co-Supervisor)



José Mirão, University of Evora
(Co-Supervisor)



Évora, October 2017



University of Evora
ARCHMAT
(ERASMUS MUNDUS MASTER IN ARCHaeological MATerials Science)

Um protocolo multi-analítico que combina as simulações EDXRF, SEM + EDS, μ XRD e Monte Carlo aplicadas para analisar não destrutivas as de moedas de cobre portuguesas corroídas

Güncem Diktaş, 36190

Nick Schiavon, University of Evora
(Supervisor)



Antonio Brunetti, Università degli Studi di Sassari
(Co-Supervisor)



José Mirão, University of Evora
(Co-Supervisor)



Évora, October 2017

TABLE OF CONTENTS

ABSTRACT.....	v
RESUMO	vi
ACKNOWLEDGEMENTS.....	vii
1. INTRODUCTION	1
1.1. COINS AS HISTORIC ARTEFACTS.....	1
1.1.2. A BRIEF HISTORY OF COINAGE	3
1.1.2 NUMISMATICS IN PORTUGAL	4
1.2. HISTORICAL BACKGROUND OF THE COINS	4
1.3. CORROSION	9
1.3.1. COPPER CORROSION IN DIFFERENT ENVIRONMENTS.....	18
1.3.2. BURIED COPPER CORROSION IN DIFFERENT ENVIRONMENTS.....	22
2. MATERIALS AND METHODS	25
2.1. MATERIALS.....	25
2.2. METHODOLOGY	28
2.2.1. X-RAY FLUORESCENCE ANALYSIS	28
2.2.2. X-RAY DIFFRACTOMETER TECHNIQUE AND μ XRD.....	29
2.2.3. SCANNING ELECTRON MICROSCOPE	29
2.2.4. MONTE CARLO SIMULATION.....	29
2.2.5. MECHANICAL CLEANING OF THE COPPER COINS	32
3. RESULTS AND DISCUSSION.....	34
3.1. μ XRD.....	34
3.2. SEM-EDS.....	44
3.3. MC SIMULATION	55
3.4. EDXRF	60
4. FINAL REMARKS AND FURTHER WORKS	69
5. REFERENCES	71
ANNEX	79
WORKING PRINCIPLES OF APPLIED ANALYTICAL TECHNIQUES.....	79
1. X-RAY FLUORESCENCE ANALYSIS	80

2. X-RAY DIFFRACTOMETER TECHNIQUE AND μ XRD	81
2.1. QUALITATIVE PHASE ANALYSIS WITH X – RAYS DIFFRACTION (XRD).....	82
3. SCANNING ELECTRON MICROSCOPE	83
4. MONTE CARLO SIMULATION	89
APPENDIX.....	105

ABSTRACT

Performing quantitative analyses on archaeological and cultural heritage metallic artefacts is challenging due to their complex multi-layered internal structure. “Layers” may include

- a) Original metal and/or alloy substrate (gold, silver, bronze etc.)
- b) Surface patinas enriched in corrosion products sulphides, oxides and/or chlorides compounds
- c) Protective treatments applied in past conservation interventions
- d) Soil derived incrustations from archaeological burial environment.

To obtain compositional data on the metal substrate, usually these layers have to be removed but this not always possible due to the inherent fragility of the corroded artefacts as it is the case in particular with copper objects such as coins. The setting up of a non-destructive protocol is therefore important. In this study, a protocol combining SEM-EDS, μ XRD, EDXRF and Monte Carlo simulations has been tested on a series of Portuguese coins from the 12th to the 19th centuries found at Largo das Olárias and Travessa do Jordão in Lisbon.

1. Analyze non-destructively the corrosion patterns and patinas developed on the surface Portuguese Copper coins from a Lisbon archaeological site (Largo das Olarias) SEM+EDS, μ XRD and portable EDXRF
2. Apply the mineralogical and chemical data obtained during the analytical sessions to run Monte Carlo simulations of EDXRF spectra
3. Assess the feasibility of the combined non-destructive protocol in obtaining a reliable quantitative estimation of the metal substrate composition without the need to remove the surface corrosion patinas.

Keywords: SEM-EDS, μ XRD, EDXRF, Monte Carlo, Copper, Coins, Corrosion

RESUMO

Realizar análises quantitativas em artefactos metálicos arqueológicos de património cultural é um desafio devido à sua estrutura interna com múltiplas camadas. Essas ‘‘Camadas’’ podem incluir:

- a) Substrato original de metal e / ou liga (ouro, prata, bronze etc.)
- b) Patinas de superfície enriquecidas em produtos de corrosão compostos de sulfetos, óxidos e / ou cloretos
- c) Tratamentos de protecção aplicados em intervenções de conservação passadas
- d) Incrustações derivadas do solo do ambiente de enterro arqueológico.

Para obter dados de composição sobre o substrato metálico, geralmente essas camadas devem ser removidas, porém isso nem sempre é possível devido à fragilidade inerente aos artefactos corroídos, como é o caso em particular de objectos de cobre como as moedas. A criação de um protocolo não destrutivo é, portanto, importante. Neste estudo, um protocolo que combina as simulações SEM-EDS, μ XRD, EDXRF e Monte Carlo foi testado numa série de moedas portuguesas dos séculos XII ao XIX encontradas num Largo das Olárias e Travessa do Jordão em Lisboa.

1. Analisar de forma não destrutiva os padrões de corrosão e patinas desenvolvidas na superfície de moedas de cobre portuguesas de um sítio arqueológico de Lisboa SEM + EDS, μ XRD e EDXRF portátil.
2. Aplicar os dados mineralógicos e químicos obtidos durante as sessões analíticas para executar simulações Monte Carlo dos espectros EDXRF.
3. Avaliar a viabilidade do protocolo não destrutivo combinado na obtenção de uma estimativa quantitativa confiável da composição do substrato metálico sem a necessidade de remover as patinas de corrosão superficial.

Palavras-chave: SEM-EDS, μ XRD, EDXRF, Monte Carlo, Cobre, Moeda, Corrosão

ACKNOWLEDGEMENTS

I wish to express the deepest gratitude to my supervisor professor Nick Schiavon and my co-supervisors Antonio Brunetti and José Mirão for their guidance, advice, criticism and encouragements throughout this research.

I really would like to express my gratefulness to Professor Andre Teixeira and Tiago Gil Curado from the University of Lisbon for their kind support and provision of the samples.

I would also like to thank everyone in the HERCULES Lab for their assistance and my fellow ARCHMAT students.

Finally, special thanks to my mother who always supported and encouraged me, to my father who whenever I called tried to make me smile, to my friends for, maybe not physically, being there for me.

1. INTRODUCTION

1.1. COINS AS HISTORIC ARTEFACTS

The conservation and valorisation of cultural heritage is of fundamental importance for our society, since it is witness to the artistic and industrial legacies of human societies. The information that can be gathered from such materials is a valuable source to understanding the past. A large component of this consists of material cultural assets that are often exposed to harmful long-term effects of environmental pollution, inappropriate handling, and intrinsic physicochemical instability. In the case of metallic artefacts such as coins, one of the main problems is the preservation of archaeological objects taken out of excavation and stored in museums or deposits.

During burial, artefacts react with the environment and become covered with corrosion products of different compositions, mainly in dependence of the chemical composition of the artefact and of the soil components. The most common alteration products of copper and copper alloys are: oxides, sulphides, basic sulphates, chlorides, hydrochlorides, basic green carbonates, and oxalates. Among them, corrosion products containing chlorides are considered very dangerous because copper and copper alloys which have been buried or recovered from a wet site can suffer from the effects of chloride salts, resulting in the development of the so-called bronze disease.

Coins are an important source of information for many disciplines such as history, archaeology, art history and similar social sciences. In addition to their highly artistic and cultural value, the textual and iconographic information embossed on the coins yield information regarding their date of production (i.e. minting), location and in most cases political purpose. While, throughout the history many different objects have been used for commercial activities, their durability, availability and material value has made coins the most widely used form of exchange. It is clear that coins have been one of the most significant tools of valuable materials throughout history until today. The value of the coin is related to its production materials. Coins were originally produced using precious and noble metals, like gold, silver and some valuable

amalgams such as electrum (Tekin, 2000). With time, usage of precious metals decreased and copper (Cu) alloys became the default material in coin production.

First studies on coins were undertaken by European collectors and date back to the middle ages. Focus of these first studies was on the artistic value of the coins while scientific approaches to analyse coins emerged from the end of the 18th century onwards (Atlan, 1984). The term “numismatics” etymologically rooted in the Ancient Greek word “*nomisma/noummos*” and in Latin “*nummus*” meaning “coin”. The discipline of numismatics is based on the examination of metal parts used as payment instruments in commercial and statutory exchange transactions, recorded by authorized public authorities. In addition, medals, coins, money substitutes, which are traded like coins and money in terms of their appearance, and various objects are also within the scope of numismatics (Morrisson, 2002). Numismatic is an important science for reconstructing historical periods, when it is discussed where, when and how it is printed, the number and circulation, its role in economic life, and its compliance with the law. It is also closely tied with the birth of archaeology and compatible with its development. This frees the coins from the hands of collectors and interpret their general state of view by linking the relationship with known texts and events (Morrisson, 2002)

Cultural heritage objects can yield invaluable insights into human past and should be managed carefully. The last decades have witnessed the emergence of multi-disciplinary approaches for interpretation of archaeological materials to answer research questions relating to human material and cultural past. In particular, grouped under the term “archaeometry”, the scientific analyses of these materials with historic interest aim to determine the chemical and physical properties of archaeological artefacts. The internal structure or elemental concentration of the archaeological artefact is highly important, because it has the characteristic fingerprint of the artefact. With the possibilities yielded by these new methodologies various research questions relating to authentication, provenance, cultural context, economic circumstances and the human interactions with its local environment, can be developed and addressed. In most cases, these methodologies include non or micro invasive techniques that result in the minimal degree of alteration on these immensely valuable objects.

Within this framework, Portuguese coins from different periods and with varying degrees of corrosion were selected for analysis. Documentation of the samples was carried out according to their typology, source and by taking their photographs. For each sample, all possible analytical methods including XRF, μ -XRD and SEM-EDS were applied to obtain data relating

to the chemical and mineralogical compositions. Following, the data was processed through Monte Carlo simulation with XRMC code package for the simulation of the compositional data.

1.1.2. A BRIEF HISTORY OF COINAGE

Coin can be described as a paying tool made of metal with a circular shape. Before coinage became the dominant tool of commercial activity, many other objects and materials such as various metals, bovines, tripod cauldrons (metal), axes, sea shells, metal rings, iron paddles, copper axes, iron swords and even raw copper ingots were used for trading (Einzig, 1966). First coins were minted during the 7th century BC by the Lydians. Lydian Civilization was located in western Asia Minor (between Gediz and Menderes Rivers) (Tekin, 2000). Among the ancient writers, it was Herodotus, who lived in the 5th century BCE, to mention the origins of coin production in Asia Minor. The invention of coin ended the diversity of paying tools in terms of material selection and standardized it. From the ancient written sources and archaeological findings, gold, silver, copper and bronze were used in the minting of coin in ancient time (Tekin, 2000). In Asia Minor, the first coins to be minted were electrum (from in Latin), which is a naturally occurring alloy of gold and silver, with trace amounts of copper and other metals (Caley, 1964). The gold content of naturally occurring electrum in western Asia Minor ranges 70% - 90%. However, gold content of electrum used in Ancient Lydian coinage was found to be 45 % – 55% (Millman, 2015). The changes in the gold might be due to economic reasons. In Classical Greece and during the Hellenistic Period, coins minted were of mainly silver or bronze and partly gold. Until the Roman period, silver was the most important metal in Greece. After the late antiquity, the main metal for the coin production became copper. The increase in copper usage was came result of progressive extinction of precious mineral deposits used in antiquity (Einzig, 1966)

In general, from the Classical Greece onwards coins were used as political tools to convey the corporate image of city states, politicians and military leaders. The inscriptions and figures encountered on both sides of ancient coins, therefore reflect tremendous amounts of information in relation to political and economic circumstances of the period.

Furthermore, the inscriptions engraved on coinage can yield information such as:

- Name of the city state or political entity that minted the coin,
- The date of the minting as well as the political figure that commissioned the minting
- Name and status of the people who undertook the minting of a certain group of coinage
- Type of the coin
- Name of coin moulder,
- Date (from the Hellenistic period onwards)
- Unit (from Hellenistic period onwards, but rarely) (Tekin; 2000).

1.1.2 NUMISMATICS IN PORTUGAL

The researchers who undertake a study of Portuguese numismatics face a significant challenge posed by the absence of a systematic or annotated bibliography, since, during their research they need a large number of articles, booklets, magazine, catalogues that make up the “patchwork” of numismatics over the last hundred and fifty years.

The most important, although not-dated, printed source for Portuguese numismatic is still the *Descrição Geraç e Historica das Moedas Cunbadas em Nime dos Reis, Regentes e Governadores de Portugal*, by Augusto Carlos Teixeira de Arago, published between 1894 and 1880. In addition, researchers can also refer to two general books, *Da Numismatica em Portugal*, Jose Liete de Vasconcelas (1923) and *Cartilha da Numismatica Portuguesa*, Pedro Batalha Reis (1925-56), as well as a limited number of monographs by Joaquim Ferraro Vaz. Batalha Reis and Damiao Peres, almost all published between 1943 and 1964 (Marques, 1982).

1.2. HISTORICAL BACKGROUND OF THE COINS

The coins analysed were recently discovered in rescue excavations in Lisbon at two sites: Largo das Olarias and Travessa do Jordão. The results of these excavations are yet to be published by the archaeologists and the information presented in the following paragraphs are derived from the notes of the archaeologists in charge. The archaeological context of both sites, Largo das Olárias and Travessa do Jordão (Figure 1) have urban characteristics and located within the city limits. The formation layers of the site consist three distinctive strata representing (1) a burial environment (cemetery), (2) pottery production (characterised by kilns) and (3) signs of

urbanization. During the rescue excavations, the context of the cemetery stratum yielded 600 hundred human skeletons, belonging to the Jewish and Muslim inhabitants of the settlement.

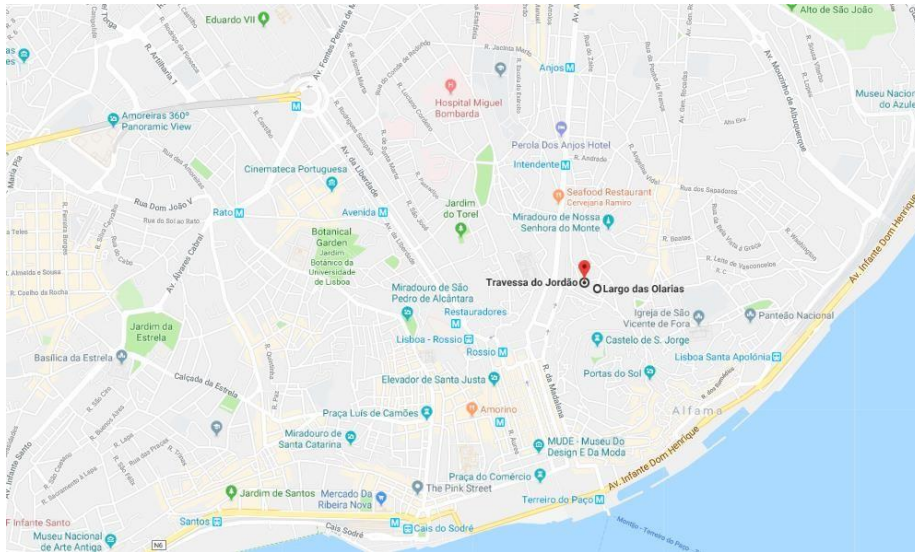


Figure 1: The map of Largo das Olarias and Travessa do Jordão

(<https://www.google.com/maps/place/Largo+das+Olarias,+Lisboa/@38.716697,9.1356713,17z/data=!3m1!4b1!4m5!3m4!1s0xd1933888d057467:0x5371a10b412a71ec!8m2!3d38.7169544!4d-9.1333144>)

Having the knowledge of this cemetery context is important for scientists in understanding the local soil composition, since the presence of human bones change the soil characteristics of the area, ultimately altering the corrosion mechanisms that any buried metal artefacts may undergo.

The discovery of the kiln remains over the first cemetery layer indicated that the area was used for pottery production. In fact the, very name of the site, *Largo das Olarias* (English: pottery square) indicate the past connection of the site with pottery production. During the period between the late 18th and early 19th centuries, the population of Lisbon grew, leading to the extension of the city limits. For these new building activities, the preparation of the area, in other words, the flattening of the topography was important. In this process, if the ground is uneven, loose or has unfavourable soil stratification characteristics the area must be prepared first. During such preparations, it was not uncommon to transport soil from other locations of the city. From the archaeological point of view, the importance of the foreign soil might not be as big as it is from an archaeometric perspective. Since the properties of soil and stratigraphic layers are changed, the expected corrosion mechanism and products were also changed.

The 37 coins that are the subject of this study were collected from different layers mentioned above by the archaeologists from the University of Lisbon. For the analysis of these coins, it is

very helpful to have knowledge about “old recipes” that help researchers in comparing the data and results (of the old recipes) with those of the actual samples. While it is difficult to encounter an exact recipe for the material composition of Portuguese coins, through the written sources and references it can be possible to draw some inferences (Aragão, 1877).

Several of the analysed coins can be grouped under three different types: *dinheiro* (8), *ceitil* (6) and *real* (4). This classification was created by Tiago Gil Curado, based on the imprints, official seals of the king and the shape of the coins.

Dinherio

The *dinheiro* or *dẽiro* in old Portuguese (meaning a coin of little value) was used from 12th to late 15th century. D. Afonso I was the first one who issued the coins and it was used until the D. João I. After *dinheiro*, until the republic the *real/réis/rei* was used.

It was the Romans who introduced the monetary system of *librae*, *solidi* and *denarii*. King Charlemagne of France reintroduced the system to Europe and the Portuguese system was based on this. The system was not based on a decimal hierarchy but to the weight of the metal. For the coin, different metals were used over the years, gold, silver or bronze, which all had different values. The original *librae* indicated a pound of silver. Portugal has gained independence after the Battle of Ourique on 25 July 1139 by Afonso Henriques as King Alfonso I (1128-1185) was recognized by the King of León and Castile Afonso VII in 1143, and by Pope Alexander III in 1179. After the Pope’s approval, king adopted the *dinheiro* as a currency of Portugal and it was used until 1433.

The main characteristic of the *dinheiro* coin is the large cross that it bears –a feature common in medieval coinage. The other face of the coin has five shields arranged to form a cross, each of them with five dots, in memory of the five Moorish kings defeated by Alfonso I at the battle of Ourique (Aragão, 1877).

The Charlemagne’s monetary reform was based on the *livre Carolingienne* in silver subdivided in 20 *sous* or 240 *deniers*. The British pound, the Italian *lira*, the Spanish *dinero* and the Portuguese *dinheiro* were all derived from French *denier* (Aragão, 1877).

As for the counting units, 12 *dinheiros* equalled one *soldo* and 20 *soldos* were equal to one *libra*: the denomination of half a *dinheiro* was called *mealha*. New coins introduced in the following centuries were the gold *morabitino*, introduced by Sancho I (1185-1211) from the Spanish

maravedí and equivalent to 15 soldos, and the silver tornês, introduced by the King Dinis one century later which worth 5½ soldos (<https://www.moedanumismatica.com/coins/portugal.html>).

Ceitel

The ceitel was a copper coin introduced in the reign of D. Afonso V and produced in very large numbers under From D. Afonso V to D. Sebastião ceitils were used. They have a very uniform typology and easily identifiable by the Castle that adorns the obverse. The uniformity of typology multiplies in hundreds of different styles and variants. The rarity varies greatly within each reign, although it is to be admitted that the reigns of D. João II and D. Sebastião will be the least common. In addition, there are styles that are always rare, such as the "crowned", the "border" or the mythical Arabic, the only one that does not feature a castle (Magro, 1986).

Real

In 1380 D. Fernando I introduced the gold dobra and the silver real. The name real is derived from the Spanish silver coin called *nummus realis*. D. João I (1385-1433) introduced a new real called *real branco*, in bullion equals the 70 soldos (840 dinherios), adopted by his successor, D. Duarte in 1433. Also *real preto* which is one tenth of *real branco* was issued in copper. Under the rule of D. Manuel I (1495-1521), copper *real* coins was started minting, which also the name was *real branco* was simplified to *real*. In 1580s last real coins were minted. Until 1750, the smallest coins was the 1½ réis and then until 1875 the smallest circulating denomination became the three réis coin (Aragão, 1877). The denominations of 3, 5, 10, 20 and 40 réis were in copper, denominations of 50, 60, 100, 120, 240 and 480 réis were in silver, and 480, 800, 1200, 1600, 3200 and 6400 réis were in gold. The standard gold coin was 6400 réis, called *peça*, which increased its value to 7500 réis after 1826. For the minting of the coins, the decimal system was adopted in 1837. First copper was used and after 1882 bronze for 3, 5, 10 and 20 réis denominations, silver coins for 50, 100, 200, 500 and 1000 réis denominations, and gold 1000, 2000, 2500, 5000 and 10,000 réis denominations. The 50 and 100 réis denominations were issued in cupro-nickel in 1900. The first banknote of Portugal was issued in 1847 by the Banco de Portugal. In 1854, the gold standard with a ratio of 1000 réis = 1.62585 grams fine gold was adopted and maintained until 1891 (<https://www.moedanumismatica.com/coins/portugal.html>).

Coin minting in Portugal always has been an exclusive privilege of the kings and the state. In ancient times, Romans, Swabians, Visigoths and Arabs produced coinage in areas that are part of modern Portugal. The origins of the Lisbon mint can be traced to the very beginning of the Portuguese nationality (1139 AD). The Casa da Moeda (Lisbon Mint) was established in the 12th century as the Royal Mint of Portugal and Assay Office of Precious metals. The Mint had been publicly owned company since 1972, when it merged with the Imprensa Nacional (Government Printing Office), founded in 1978 as The Royal Printing House (Trigueiros, 1995). As previously mentioned the money mainly minted in Lisbon but when the more money required, other mints were also used. The list can be seen below on the the Table 1.

Table 1: Chronological list of Portuguese mints

D. Afonso I	Braga and Coimbra	Governadores	Lisbon
D. Sancho I	Braga	D. Antonio	Lisbon and Goa
D. Afonso II	Braga and Lisbon	D. Filipe I	Lisbon and Goa
D. Sancho II	Lisbon	D. Filipe II	Lisbon and Goa
D. Afonso III	Lisbon and Coimbra	D. Filipe III	Lisbon and Goa
D. Dinis	Lisbon	D. João IV	Lisbon, Porto, Evora and Goa
D. Afonso IV	Lisbon	D. Afonso VI	Lisbon, Porto and Goa
D. Pedro I	Lisbon	D. Pedro II	Lisbon, Porto, Goa, Diu, Bahia, Rio de Janeiro, Minas Gerares and Mozambique
D. Fernando	Lisbon, Porto, Crunha, Miranda, Çamora and Tuy	D. João V	Lisbon, Porto, Goa, Diu, Bahia, Rio de Janeiro, Minas Gerares and Mozambique
D. João I	Lisbon, Porto and Evora	D. José I	Lisbon, Goa, Diu, Bahia, Rio de Janeiro, Minas Geraes and Mozambique
D. Duarte	Lisbon and Porto	D. Maria I	Lisbon, Goa, Diu, Bahia, Rio de Janeiro,

			Minas Geraes and Mozambique
D. Afonso V	Lisbon, Porto, Evora and Ceuta	D. João VI	Lisbon, Goa, Diu, Bahia, Rio de Janeiro, Minas Geraes and Mozambique
D. João II	Lisbon and Porto	D. Pedro IV	Lisbon
D. Manuel	Lisbon, Porto, Coehim, Goa, Malaca and Ceuta	D. Miguel	Lisbon, Goa and Diu
D. João III	Lisbon, Porto, Coehim and Goa	D. Maria II	Lisbon, Porto, Angra, Goa, Diu and Mozambique
D. Sebastião	Lisbon, Porto, Coehim and Goa	D. Pedro V	Lisbon, Goa and Diu
D. Henrique	Lisbon	D. Luiz	Lisbon and Goa

The fact that the coin is a finished product of an organised industrial process shouldn't be forgotten. Since the first coin, various techniques used to make coins, from primitive hammering to steam powered coining press in the 19th century.

1.3. CORROSION

The corrosion of metals is the degradation of the metallic structure at its surface through chemical reactions of the metal with species of the environment. In contrast to mechanical wear, corrosion is principally a chemical process. The surface of nearly all ancient metal objects which are buried in soil, immersed in fresh or in salt water or exposed to air, rain and sun, will certainly be affected by corrosion. The surface alteration may be quite thin and superficial or it may be so complete that nearly none of the original metal remains. Eventually, the metal reverts to mineral forms. Most corrosion phenomena are electrochemical in nature. They imply two or more electrode reactions: the oxidation of a metal (anodic partial reaction) and the reduction of an oxidising agent (cathodic partial reaction) (Selwyn, 2004). Furthermore, the corrosion process also requires an ionic connection (an electrolyte) between the anode and cathode to allow the flow of ionic species. In most corrosion processes, this ionic connection is provided

by water, e.g. condensation from humid air, rain, or seawater. Whenever the relative humidity is higher than 65 %, there is enough absorbed water on most clean metal surfaces to approach the behaviour of bulk water and support electrochemical reactions. Damp soil or a damp deposit may also hold water against the surface of metal..

Corrosion is the process of a metal returning to its thermodynamically stable state. For most metals, the formation of the oxide or sulphide states are the natural processes that carry the metals to their natural state. These processes are electrochemical reactions that occurs according to the laws of thermodynamics (Schweitzer, 2009).

Corrosion is a time and temperature depended, and a good knowledge of chemistry and electricity is required to thoroughly understand such phenomena. They also explain the establishment of the corrosion reactions, rates, the effects of ion and corrodent concentrations and also reversible and/or non-reversible reactions (Schweitzer, 2009)

During the corrosion of a metal surface, two types of reactions occur: one is anodic and the second one is cathodic, both reactions involving charge transfer reactions.



The metal cations released at the anode may enter the environment as aqueous ions and precipitate away from the metal. Therefore, the metal continues to corrode. The metal is then in a so-called “active” state. Alternatively, the metal cations may react immediately with anions in the environment and form corrosion products (carbonates, oxides, hydroxides, sulphates, etc.) which adhere to the surface of the metal. Sometimes there is a progressive growth of the surface minerals which increases at the expense of the metallic core; in other cases, the mineralisation is compact, stable, and tends to inhibit further change. The metal is then said to be in a “passive” state (Selwyn, 2004). In each case, the electrons produced by the metal oxidation half-reaction at the anode must be simultaneously consumed by a balancing reduction half-reaction at the cathode. In aqueous solutions, this reaction is usually the reduction of hydrogen ions or the reduction of oxygen. However, in general, the species co-reducing may

be any species in the corrosive electrolyte reducing at a more positive potential than the metal system (Selwyn, 2004; Hamann, Hamnett, & Vielstich, 2007).

A chemical reaction will occur only if the Gibbs free energy change (ΔG) is negative. For electrochemical reaction, the Gibbs free energy is calculated from,

$$\Delta G = -nFE$$

where n is the number of electrons, F is Faraday's constant, and E is the cell potential.

Total potential of the corrosion is the difference between the half reactions.

$$E = \text{Cathode half-cell} - \text{Anode half-cell}$$

The potentials of the oxidation and reduction is measured from the standard half-cell potential (SHE) chart (Table 2), where the potentials relative to the H^+/H_2 (Schweitzer, 2009).

Table 2: Standard Oxidation–Reduction Potentials 25°C, Volts vs. Hydrogen Electrode (Bardal, 2004).

25°C, Volts vs. Hydrogen Electrode	
Redox Reaction	Oxidation- Reduction Potential
$Au = Au^{3+} + 3e^-$	+1.498
$O_2 + 4H^+ + 4e^- = 2H_2O$	+1.229
$Pt = Pt^{2+} + 2e^-$	+1.2
$Pd = Pd^{2+} + 2e^-$	+0.987
$Ag = Ag^+ + e^-$	+0.799
$Fe^{2+} = Fe^{3+} + e^-$	+0.788
$Fe^{3+} + e^- = Fe^{2+}$	+0.771
$O_2 + 2H_2O + 4e^- = 4OH^-$	+0.401
$Cu = Cu^{2+} + 2e^-$	+0.337
$Sn^{4+} + 2e^- = Sn^{2+}$	+0.15
$2H^+ + 2e^- = H_2$	0.0000
$Pb = Pb^{2+} + 2e^-$	-0.126
$Sn = Sn^{2+} + 2e^-$	-0.136
$Ni = Ni^{2+} + 2e^-$	-0.250

$\text{Co} = \text{Co}^{2+} + 2\text{e}^{-}$	-0.277
$\text{Cd} = \text{Cd}^{2+} + 2\text{e}^{-}$	-0.403
$\text{Fe} = \text{Fe}^{2+} + 2\text{e}^{-}$	-0.440
$\text{Cr} = \text{Cr}^{3+} + 3\text{e}^{-}$	-0.744
$\text{Zn} = \text{Zn}^{2+} + 2\text{e}^{-}$	-0.763
$\text{Al} = \text{Al}^{3+} + 3\text{e}^{-}$	-1.662
$\text{Mg} = \text{Mg}^{2+} + 2\text{e}^{-}$	-2.363
$\text{Na} = \text{Na}^{+} + \text{e}^{-}$	-2.714
$\text{K} = \text{K}^{+} + \text{e}^{-}$	-2.925

When the potential difference is higher, the force to run the reaction is also higher. For the corrosion, there should be a completed circuit, which controlled by Ohm's Law:

$$I = E/R$$

From equation, if the R (resistance) were infinite, corrosion will not occur and if the R is zero, the rate of corrosion will be infinite (Schweitzer, 2009).

Corrosion of metals are more complicated than what is expected from standard half-cell series. Just looking at the oxidation and reduction potentials of a metal, the occurrence of corrosion cannot be predicted, because during corrosion various reactions run at the same time. The formation of corrosion products largely depends on the electrochemical potential of the system and the pH. This correlation can be represented with Pourbaix diagram, where potential is plotted on the y axes, pH on the horizontal x axis, and similarly to phase diagrams a range of axes indicate what corrosion products are stable given the particular values of the two variables (Pourbaix 1966). It does not indicate corrosion rates but acts as a guide to system dynamics, indicating conditions in which the material is immune to corrosion, undergoes active corrosion and when passivation occurs. In terms of artefacts coming from archaeological contexts several complications occur that render Pourbaix diagrams less of a direct indication to the conditions under which the product may have formed. The burial or deposition environment is potentially significantly more dynamic and complex to be represented with such a diagram in a meaningful way. The presented diagrams include influences of the presence of sulphates, carbonates and chlorides in a solution, in order to illustrate their role in the thermodynamic process. However,

in practice, the corrosion products found are not limited to those covered in the diagrams. They are, nevertheless, an extremely useful tool for understanding the thermodynamic processes occurring during the interaction between an artefact and the environment. The diagram is a graphical representation of Nernst's equation for the various reactions (Jones, 2004).

The potential–pH diagram has three zones:

1. Immunity zone. Under these conditions of potential and pH, metal remains in metallic form.
2. Corrosion zone. Under these conditions of potential and pH, metal corrodes.
3. Passive zone. Under these conditions of potential and pH, protective layers form on metal and further corrosion does not take place (Schweitzer, 2009).

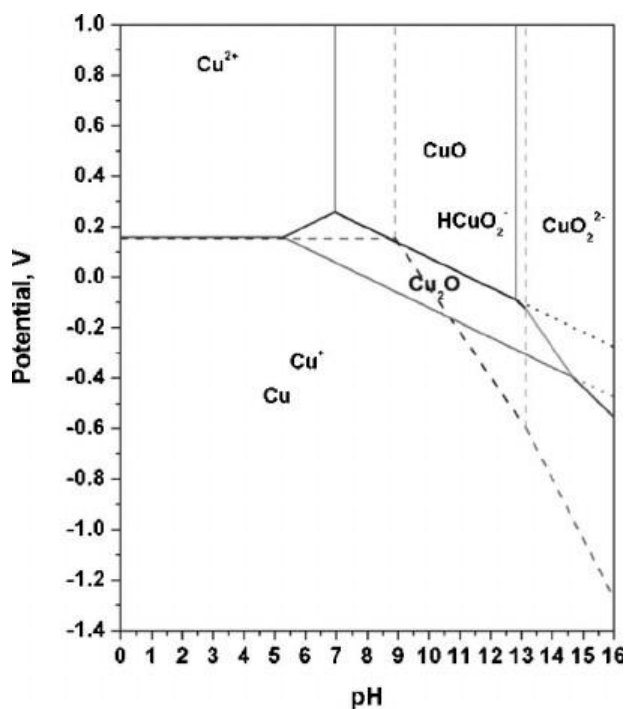


Figure 2: Pourbaix diagram of copper in Cu-H₂O system at 25°C (Pourbaix, 1966)

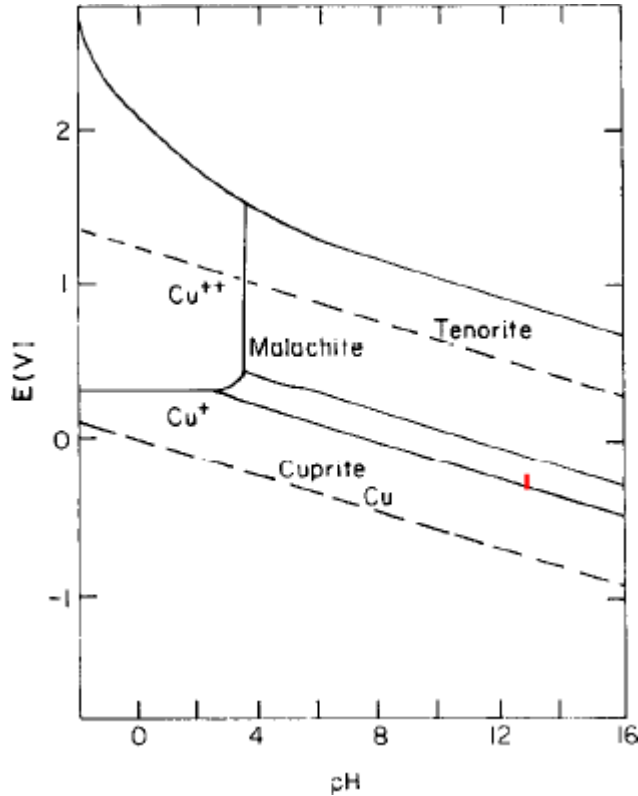


Figure 3: Pourbaix diagram of copper in Cu-Cl-O₂ system at 25°C (Pourbaix, 1966)

The main objectives of the Pourbaix diagrams are listed below:

1. To show the directions of the various reactions at given pH and potential.
2. To make a basis for estimation of the corrosion product compositions at various pH and potential combinations.
3. To show which environmental pH and potential changes will reduce or prevent corrosion.

In Figure 2 and 3 Pourbaix diagram of copper in H₂O system and Cl-O₂ system at 25°C can be seen at 25°C (Pourbaix, 1966). Corrosion can happen in different environments which is the most important element in corrosion processes. All external factors that lead the metal and alloy corrosion can be sum up under the environment topic, because “environment” provides the fluids, which are making the charge transfer reactions possible. The transfer of the reactants to the corrosion site and removal of corrosion products is possible because of the environment. During the transportation of ionic species between the anodic and cathodic sites, it provides the medium. Atmosphere (urban and industrial), freshwater, marine, underground and military can count as a different environments that affect the corrosion process differently (Cramer and Covino, 2006)

From the archaeological point of view it is better the focus on specifically corrosion in buried environments. Almost all the metal artefacts were found in buried environments, because they were lost, abandoned and sacrificed with time (Fjaestad et al., 1998)

Environmental pollutants, other archaeological materials, geography, microorganism in the soil, vegetation, land use, soil chemistry and physical properties and the presence or absence of water and air are the variables that can affect the corrosion process and products of buried metals together with the type of a metal (Fjaestad et al., 1998).

Water

The corrosion of buried metal artefacts is electrochemical; water is the electrolyte, and dissolved species (salts, gases) affect the corrosion rate. The amount of water available can range from water vapour at various relative humidities to fluid water under immersed conditions (Harris and Eyre, 1994). When metal artefacts sink to the bottom of rivers, lakes, harbours, or the ocean, they are surrounded by water and may become partially or completely buried in sediment. When metal artefacts are buried in soils, they can be located below the water table, where the soil particles are completely surrounded by water, or they can be buried above the water table, where the space between soil particles is filled with moist air and other gases (Wilmott and Jack, 2000). Variations in the water table can further complicate the corrosion process of metal artefacts. Above the water table, the compactness and water content of soils are important; clays retain moisture within capillaries, whereas sandy soils drain quickly (Harris and Eyre, 1994).

Dissolved salts

The dissolved salts increase the conductivity of water while lowering the soil resistivity. They also accelerate electrochemical reactions, which fasten the corrosion on metal surface (Wilmott and Jack, 2000). On the other hand, if metal surface has a insoluble protective layer, the rate of corrosion slows down. Soluble salts can be found in groundwater, lakes, and oceans. The freshwaters has the lowest concentration. When the waters are subject to a high rate of evaporation the concentration of dissolved salts increases (Rowlands, 1994). Soil solutions associated with calcareous (limestone, dolomite) soils are high in magnesium, calcium, and carbonate ions (Harris and Eyre, 1994). When the net direction of water movement is upward in the arid regions, evaporation at the soil surface originate the precipitation of salts containing various cations (e.g., sodium, potassium, magnesium, calcium) and anions (e.g., carbonates,

chlorides, sulphates). (Wilmott and Jack, 2000). Metal artefacts that were buried under these conditions are usually covered with salts and metal carbonates and/or sulphates (Raiswell, 2001). Chloride, sodium, sulphate, magnesium, calcium, and potassium are the main ionic components in seawater (Florian and Florian., 1987) Human activities can alter the dissolved salts concentration in the soil (Fjaestad et al., 1998).

Dissolved Gases

Oxygen and carbon dioxide are the main dissolved gases in surface waters. They are derived from the atmosphere, biological activity and/or the decomposition of organic material. The gas solubility decreases with the increasing temperature (North and MacLeod, 1987).

Oxygen

Reduction of oxygen gas is common cathodic reaction for the buried metal artefacts. In aerated damp environments, it is more likely that metals to be heavily corroded than in low-oxygen environments. Because of local turbulence and photosynthesis, surface waters exposed to the atmosphere generally become saturated with oxygen (solubility 2.7×10^{-4} M) (Raiswell, 2001). For the soils that the diffusion of air is restricted, oxygen gas is only slowly incorporated into water. Low oxygen levels exist in stagnant, waterlogged soils (clay, peat bogs) and under marine sediments and concretions, which actually these conditions are less corrosive to buried metal artefacts. Although under the anaerobic conditions, if sulphate-reducing bacteria are exist, corrosion can occur (Fjaestad et al., 1998).

Carbon dioxide

Carbon dioxide dissolves in water and produce carbonic acid, H_2CO_3 (Raiswell, 2001). The dissolution of atmospheric CO_2 and the aerobic decay of organic matter introduce carbon dioxide gas into the water. Biological activities removes oxygen and generates carbon dioxide (Wilmott and Jack, 2000). If the atmosphere is the only source of carbon dioxide, the water become slightly acidic (pH 5.6). When carbon dioxide is produced by the breakdown of organic matter, then the concentration of dissolved carbon dioxide is increased, and the pH becomes more acidic (e.g., pH 4.9) (Raiswell, 2001). Seawater's pH range is between 7.5 and 8.3 by the buffering action of the bicarbonate (HCO_3^-)-carbonate (CO_3^{2-}) equilibrium (North and MacLeod, 1987).

Sulphate-Reducing Bacteria (SRB)

SRB grow in near-neutral, anaerobic environments where source of sulphate ions, such as decomposing organic matter exists (Dexter, 2003). These bacteria can be found in waterlogged soils; in mud at the bottom of rivers, lakes, marshes, and estuaries; and under deposits on metals in freshwater and seawater (Dexter, 2003).

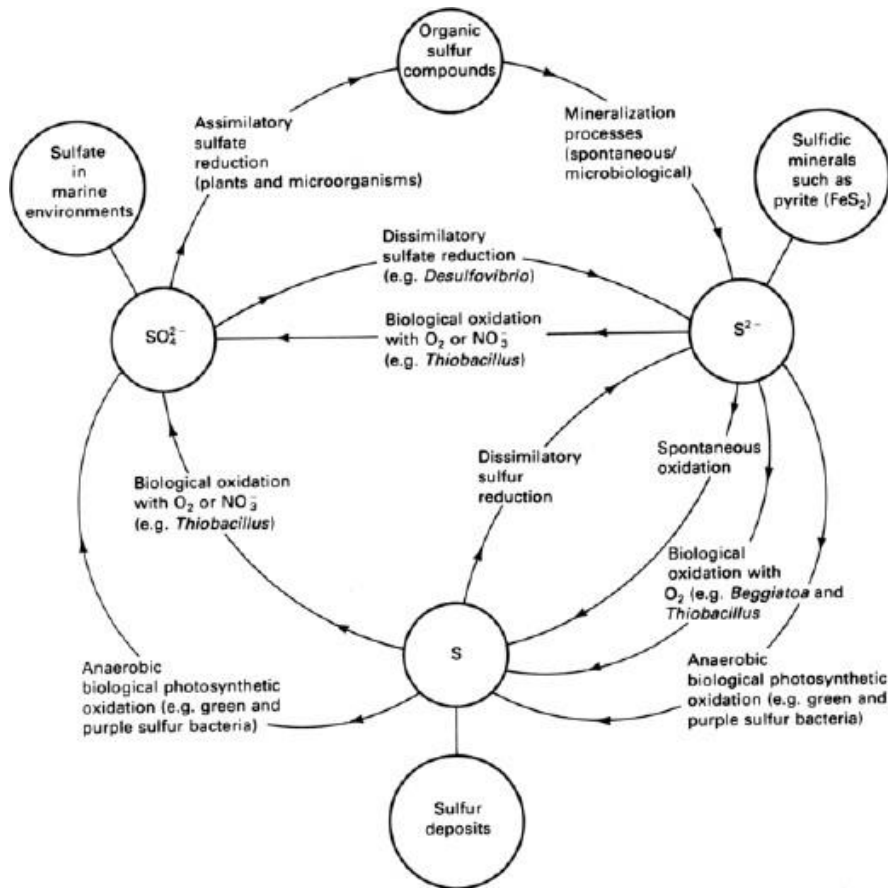
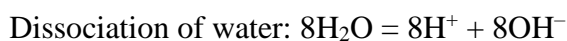


Figure 4: The sulphur cycle showing the role of bacteria in oxidizing elemental sulphur to sulphate and in reducing sulphate to sulphide. (Microbial Corrosion, Proceedings of the Conference)

These bacteria promote reduction of present sulphate to sulphide according to given reactions below.



When the bacteria grows on a metal surface, it consume hydrogen atoms produced at cathodic sites and reduce sulphate (SO_4^{2-}) ions to sulphide (S_2^-) ions then the sulphide ions react directly with metal ions to form metal sulphides (Dexter, 2003). When SRB are located in close proximity to metals, then the sulphide ions dissolve as HS^- ($>\text{pH } 7$) or H_2S ($<\text{pH } 7$) and diffuse to the metal surface (Protopopoff and Marcus, 2003) In marine sediments, typically 50 cm depth the maximum SRB populations can be observed. If decaying organic material is present, SRB can be located at greater depths (North and MacLeod, 1987). In some cases, even though conditions are favourable, SRB might remain inactive. The inactivity of the SRB was attributed to tannins in the soil (Tylecote, 1979). The formation of local deposits of metal sulphides can accelerate the corrosion rate. The pits creates discontinuous sulphide film is present and the discontinuity resulted in galvanic effect on the metal surface (Wilmott and Jack, 2000).

pH

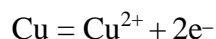
Generally pH of most environments changes between 4 and 9, although for some cases it can be a lower or higher (Turgoose, 1993). When organic material decompose and organic acids produce, the environment become acidic ($\text{pH}<7$) (Garrels and Christ, 1965). Rainwater, waterlogged soils, and bogs are mostly acidic ($\text{pH } 3$ to 6) (Raiswell, 2001). Oxidation of metals and the dissolution of corrosion products are encouraged by acidic environments. In general, alkaline soils are less aggressive to metals, whereas acid soils are more aggressive (Tylecote, 1979). Dissolution of inorganic compounds creates alkaline environments ($\text{pH}>7$) (Raiswell, 2001). For example, dissolution of calcium carbonate in the soils, results in alkaline environment (Wilmott and Jack, 2000). The seawater is alkaline ($\text{pH } 7.5$ to 8.3) because of the buffering action of the bicarbonate-carbonate equilibrium (North and MacLeod, 1987) but in the marine sediments, because of the SRB activity, pH might be neutral.

1.3.1. COPPER CORROSION IN DIFFERENT ENVIRONMENTS

Primary use of copper since the antiquity was for water systems, not only because it has high corrosion resistivity but also it is biostatic, which means bacteria will not grow on the surface. Copper has many alloys, brasses and bronzes can be count as the main ones. Copper provide higher strength and corrosion resistance to the alloy. The most common additions for alloying are zinc, tin, and nickel (Cramer and Covino, 2006).

The corrosion of copper can be classified according to the corrosive environment to which an artefact is exposed. For archaeological bronzes, five corrosive environments can be considered: atmospheric conditions, indoor museum environment, soil (burial) conditions, marine environment, and post-excavation environment (Scott, 2002; Selwyn, 2004). Depending on the environment, different corrosion products are formed; for example malachite is typically formed in soil, brochantite in the atmosphere, and atacamite in seawater. However, objects can be corroded in different environments during certain stages in their lifetime. This means that archaeological artefacts are usually associated with complex corrosion mechanisms and that different corrosion compounds can be formed during exposure to different environments. Furthermore, even apparently identical objects discovered only a few metres apart on the same site, can be corroded in totally different ways since chemical defects such as damage, segregations and inclusions, as well as structural defects, such as grain boundaries, dislocations and stresses within the materials, might influence the occurring corrosion phenomena.

The anodic reactions for copper are



and in a neutral aerated aqueous solution\ the cathodic reaction is



An overview of common copper minerals and corrosion products is given in Table 3, followed by a brief description of the corrosion products which are most relevant to this work.

Table 3: Some corrosion products identified on archaeological copper alloys

Chemical name	Mineral name	Chemical formula	Color
Oxides and hydroxides			
Copper oxide	Cuprite	Cu_2O	Red
Carbonates			
Copper carbonate hydroxide	Malachite	$\text{Cu}_2\text{CO}_3(\text{OH})_2$	Green
Copper carbonate hydroxide	Azurite	$\text{Cu}_3(\text{CO}_3)_2(\text{OH})_2$	Blue
Copper sodium carbonate trihydrate	Chalconatronite	$\text{CuNa}_2(\text{CO}_3)_2 \cdot 3\text{H}_2\text{O}$	Blue
Chlorides			
Copper chloride	Nantokite	CuCl	Pale gray
Copper chloride dihydrate	Eriochalcite	$\text{CuCl}_2 \cdot 2\text{H}_2\text{O}$	Blue-green
Copper chloride hydroxide	Atacamite	$\text{Cu}_2\text{Cl}(\text{OH})_3$	Green
Copper chloride hydroxide	Clinoatacamite	$\text{Cu}_2\text{Cl}(\text{OH})_3$	Green
Copper chloride hydroxide	Paratacamite	$\text{Cu}_2\text{Cl}(\text{OH})_3$	Green
Copper chloride hydroxide	Botallackite	$\text{Cu}_2\text{Cl}(\text{OH})_3$	Green
Phosphates			
Calcium copper sodium chloride phosphate pentahydrate	Sampleite	$\text{CaCu}_5\text{NaCl}(\text{PO}_4)_4 \cdot 5\text{H}_2\text{O}$	Blue-green
Copper hydroxide phosphate	Libethenite	$\text{Cu}_2(\text{OH})(\text{PO}_4)$	Green
Sulfides			
Copper sulfide	Chalcocite	Cu_2S	Black
Copper iron sulfide	Chalcopyrite	CuFeS_2	Yellow
Copper sulfide	Geerite	$\text{Cu}_{1.6}\text{S}$	Black
Copper sulfide	Digenite	$\text{Cu}_{1.8}\text{S}$	Blue-black
Copper sulfide	Djurleite	$\text{Cu}_{1.96}\text{S}$	Black
Copper sulfide	Covellite	CuS	Dark blue
Sulfates			
Copper hydroxide sulfate	Brochantite	$\text{Cu}_4(\text{OH})_6\text{SO}_4$	Green
Copper hydroxide sulfate	Antlerite	$\text{Cu}_3(\text{OH})_4\text{SO}_4$	Green
Copper hydroxide sulfate monohydrate	Posnjakite	$\text{Cu}_4(\text{OH})_6\text{SO}_4 \cdot \text{H}_2\text{O}$	Light blue
Copper iron hydroxide sulfate tetrahydrate	Guildite	$\text{CuFe}(\text{OH})(\text{SO}_4)_2 \cdot 4\text{H}_2\text{O}$	Yellow-brown
Copper chloride hydroxide sulfate trihydrate	Connellite	$\text{Cu}_{19}\text{Cl}_4(\text{OH})_{32}(\text{SO}_4) \cdot 3\text{H}_2\text{O}$	Blue

Copper oxides

The most widely occurring alteration product of ancient copper and its alloys is cuprite (Cu_2O). Cuprite typically has a lustrous dark red to orange red colour, although it may exhibit a range of colours; yellow, orange, red or dark brown, depending on impurities, non-stoichiometry and particle size. Cuprite occurs over a wide range of conditions; it can form on a bronze by exposure to moist air, by tarnishing in use, or during burial. For the majority of bronzes, cuprite is the corrosion layer which immediately overlays the original metallic surface. Usually most of the cuprite is concealed beneath overlaying green basic copper salts.

Tenorite is usually a dull black cupric oxide (CuO) and a rare component of natural patinas. When it is present as a patina constituent, it usually indicates that the object has been subjected to heating before or during burial (Scott, 2002).

Copper carbonates

Only two of the copper carbonate minerals are important as corrosion products; these are the green malachite ($\text{Cu}_2(\text{OH})_2\text{CO}_3$) and the blue azurite ($\text{Cu}_3(\text{OH})_2(\text{CO}_3)_2$). The two minerals are often identified in bronze patinas formed during land burials. Their formation on buried copper alloys is promoted by high levels of carbonate ions in groundwater (Selwyn, 2004). Furthermore, malachite and azurite are also found as minor phases in corrosion products formed during outdoor exposure or sea burial and as post-excavation alteration products of other minerals (Scott, 2002). Malachite usually forms smooth, dark green compact layers on the surface of a bronze.

Malachite can be a significant component of patinas that have developed during corrosion of copper alloys buried into the soil, where it usually forms over an initial cuprite layer. The formation of azurite is favoured at higher carbonate levels. However, azurite is less stable than malachite and may be converted to it in the presence of moisture through the loss of carbon dioxide. Probably for this reason, azurite is less common than malachite. Azurite sometimes occurs on objects as a compact, continuous, dark blue layer, but more frequently as fine crystal aggregates scattered among patches of malachite (Scott, 2002; Selwyn, 2004).

Copper chlorides

The most important copper chlorides in bronze corrosion are nantokite (CuCl), and the copper trihydroxychlorides: atacamite, paratacamite, clinoatacamite and botallackite, all of which are isomers of $\text{Cu}_2(\text{OH})_3\text{Cl}$ (Scott, 2002). Nantokite is a naturally occurring, pale grey, wax-like mineral with low solubility in water. It forms under conditions of high chloride ion concentration, acidity and low oxygen conditions. In moist air, nantokite is unstable and it reacts with oxygen and water to produce copper trihydroxychlorides and hydrochloric acid. The main copper chloride hydroxides, also called basic copper chlorides, are atacamite ($\alpha\text{-Cu}_2\text{Cl}(\text{OH})_3$) and

and paratacamite ($\gamma\text{-Cu}_2\text{Cl}(\text{OH})_3$). These are naturally occurring minerals with the same chemical formula but different crystal structures, and they both have green colours. On outdoor bronzes, atacamite and paratacamite are mostly found in sheltered and partly exposed areas.

These are areas not readily washed by rain, where enough chlorides could accumulate (Scott, 2002; Selwyn, 2004).

Chloride containing corrosion products are normally associated with a marine environment. However, the copper chlorides catch the most attention for their role in bronze disease. This term has long been used to describe the appearance of powdery light green spots on the surface of archaeological copper alloys after excavation. Objects exhibiting this form of corrosion were once said to be diseased or sick, and the cause was attributed to bacterial or fungal infection. However, it is now known that this corrosion is caused by chloride contamination. Bronze disease originates from the existence of cuprous chloride in close proximity to whatever metallic surface may remain. As long as the nantokite is isolated from the surrounding air by the outer layers of corrosion, it remains unreacted. However, if the protective outer material covering the nantokite is cracked, damaged, or even removed, the nantokite is exposed to the surrounding environment. Reaction with moisture and oxygen causes this unstable compound to convert to one of the copper trihydroxychlorides (Scott, 2002; Selwyn, 2004).

1.3.2. BURIED COPPER CORROSION IN DIFFERENT ENVIRONMENTS

TERRESTRIAL ENVIRONMENTS

Copper alloys typically form a cuprite layer first and a copper carbonate hydroxide layer after in soil (Scott, 2002). Because of the reaction between copper and $\text{CO}_{2(g)}$ in the humid air or dissolved in groundwater, malachite is very common corrosion product (Scott, 2002) The green patina on the archaeological bronzes, is the result of uniform growth of malachite on the surface. Another copper carbonate hydroxide is azurite, which is less common and stable and mostly form over the malachite as a discontinuous patches (Scott, 2002). When the soils rich in salt as a result of evaporation, chalconatronite can be identified on the surface (Woods and Garrels, 1986).

If the sites has high chlorine content, copper chloride hydroxides are sometimes identified on archaeological copper artefacts (Fjaestad et al., 1998). Nantokite, which is soft, has a grayish appearance like paraffin wax, and can be stained green (Gettens, 1970), can precipitate under

or within the cuprite layer when conditions have become sufficiently reducing and acidic because of the inward diffusion of environmental chloride ions toward the anodic regions on corroding copper (Scott, 2002).

Nantokite patina can cause a *bronze disease* (Figure 5), which can be defined as “the process of interaction of chloride-containing species within the bronze patina with moisture and air” (Scott, 1990) and also as “a progressive deterioration of ancient copper alloys caused by the existence of cuprous chloride (nantokite) in close proximity to whatever metallic surface may remain” (Scott, 2002). As long as nantokite is isolated from the surrounding air by protective corrosion patina, it remains unreacted but if the protective layer is cracked, damaged, or removed, when the nantokite is exposed to the surrounding environment, it can react with moisture in the air to form copper chloride hydroxides.

Two reactions for the oxidation and hydrolysis of nantokite are (Scott, 1990):

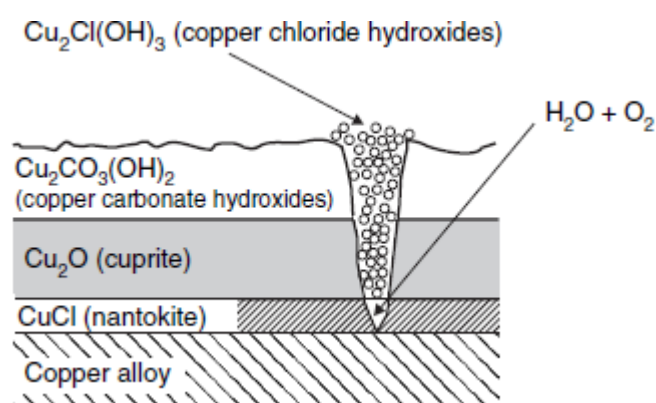


Figure 5: Schematic diagram of bronze disease on archaeological copper alloys (Organ R.M., 1970).

Copper chloride hydroxides and soluble ions, either hydrochloric acid or copper (II) chloride are the reaction products, both of which promote further corrosion of the remaining metal.

Bronzes with high tin content (from 20 to 25%), two different type of patina can be observe; compact and even and uneven and rough (Cronyn and Robinson, 1990). The bronzes with the even and compact patina are very precious because of their appearance. The selective dissolution of copper and cassiterite and other tin oxides formation reaction from the tin creates

the desired compact patina without using the original shape of the material since the change in the volume is negligible. The high-tin bronzes with the uneven and thick patina, usually contains copper chloride hydroxides and malachite covering the cuprite layer, which usually form under the high corrosion rate (Cronyn and Robinson, 1990).

MARINE ENVIRONMENTS

Under the aerated marine environments, atacamite, a copper chloride hydroxide, commonly forms. (Ref 57). Other than atacamite, other copper(II) chloride hydroxides, atacamite and paratacamite, rarely botallackite, can be identified on copper alloy artefacts (Scottt, 2002). The X-ray diffraction reference pattern of clinoatacamite (monoclinic) had been incorrectly assigned to paratacamite (rhombohedral) before and also it was misidentified as paratacamite (Jambor et al. 1996). In marine environment copper alloys, because of the pH conditions, which are rarely acidic and reducing enough for it to precipitate, nantokite is rarely found (North and MacLeod 1987).

ANAEROBIC ENVIRONMENTS

In anaerobic environments that presents sulphate-reducing bacteria, copper sulphides form on copper artefacts when they are exposed to hydrogen sulphide (Schweizer, 1994). There can be two patina observation, either thick and uneven (Duncan and Ganiaris, 1987) or thin uniform and protective (Schweizer, 1994). From reducing marine environments or waterlogged sites, copper sulphides such as chalcocite, covellite, digenite, djurleite, had been found on the corrosion patina (Schweizer, 1994). A copper-iron sulphide, chalcopyrite also found on copper alloy artefacts. This patina called pseudogilding, because of the gold-colour, that looks like gilding (Schweizer, 1994).

RARER CORROSION PRODUCTS

Depending of the soil properties, in some cases rarer corrosion products can be observe on copper surface. For example brochantite, antlerite, posnjakite can form in soils that are polluted because of the acid precipitation or in freshwater sediments (Nienhuis et al., 2016) In both marine and terrestrial environments, connellite patina formation can be observed. Where the phosphate ions are existent in the soil, either from the bones of phosphate-rich soils, the phosphate-containing copper corrosion products, libethenite and sampleite, have been identified on copper alloy artefacts (Fabrizi et al. 1989). Other than the soil, the copper alloy

composition is also another factor for identification of rare corrosion products. The alloy elements' corrosion products of also can be observed on the surface of copper artefacts. For example, Zn-rich copper alloys forms Smithsonite (zinc carbonate, ZnCO₃), copper alloys containing lead forms cerussite and pyromorphite or the bronze (Cu- Sn) patina is often has tin oxides (Angelini et al., 1993).

2 MATERIALS AND METHODS

2.1. MATERIALS

The coins studied were collected from University of Lisbon's excavations in Largo das Oleiros. The coins studied are from the period between 1143 and 1946. The age studied started with D. Afonso I and ended with the Republic. From the results of this study we will see the composition of the coins using non-destructive methods. Studied samples were of two types; undefined (classification can't be done because of the thick corrosion patina or it is broken into pieces) and defined coins (readable imprints and relatively thinner corrosion patina). The sample numbers, types, periods of the samples are shown in the Table 4.

Table 4 List of analysed coins from each king and the type of analysed coins.

Sample Number	Type	Period	Cronology
M9, M10, M11	Dinheiro	Unidentified	1143-1383
M7, M15(?), M29(?)	Dinheiro	D. Sancho II	1223-1248
M25*, M28*	Dinheiro	D. Fernando	1248-1383
M27	Real	D. João I	1385-1433
M22(?)	Ind.	D. Duarte	1433-1438
M6, M37(?)	Ceutil	D. Afonso V	1438- 1481
M1(?), M24, M25*, M28*	Ceutil	D. João III	1521-1557

M3, M4(?), M5(?), M9	Real	D. Sebastião	1557-1579
M17	Real	D. Maria I e D. Pedro III	1777-1786
M30	Reis	D. José I	1764
M8	X Centavos	República	
M2, M12, M13, M14, M16, M18, M20, M21, M23, M24, M26, M31, M32, M33, M34, M35, M36	Unidentified	Unidentified	Unidentified

Description of the stratigraphic units, where the coins found made by the archaeologist is listed below.

M1 - [1206]: Landfill. Dark brown deposit, clayey, fine grain, medium-compact homogeneous and with some small gravel and medium calcareous.

M2 - [1611]: Landfill. Reddish-brown, clayey, compact deposit, fine grain, homogeneous and with nodules of lime mortar.

M3 [619]: Landfill. Light green deposit, very compact, clayey, fine grain, homogeneous.

M4 / M5 [620]: Landfill. Dark brown, clayey, medium grain, loose, heterogeneous, with mortar nodules, peaks of coal, and some gravel of calcar.

M6 - [2106]: Landfill. Dark brown deposit, clayey sand. Medium grain, loose and heterogeneous.

M7 – [17]: Landfill. Yellowish deposit, clayey, fine grain, compact, homogeneous

M8: Surface collection.

M9 - [22]: Filling of grave. Yellowish-brown, heterogeneous, sandy-clay, medium-grained and not very compact.

M10 / M11 [69]: Filling of grave. Brownish-grey, loose, medium grain, sandy loam and heterogeneous deposit.

M12 / M13 – [1001]: Pottery dregs consisting of loose grey-brown sediment, medium grain, heterogeneous, clay-sandy, with many coals and fragments of rubefacto brick.

M14 - [1065]: Brown deposit with argillos compact, fine grain, homogeneous with peaks of coal.

M15 – [11239]: Landfill. Greenish deposit, clay-sandy, medium-compact, fine grain, homogeneous and with

M16 – [1103]: Landfill Brown, clayey, clayey, slightly compact, heterogeneous and medium grain sediment Contains large amounts of building ceramics, brick tile, arranged in a disorganized, but well compacted form.

M17 / M18 - [1110]: Landfill. A deposit that covered the entire area occupied by the survey 11. Brownish, heterogeneous, not very compact, medium grain, clayey sand and with some nodules of greenish clay.

M19 [1107]: Filling of the interior of the furnace Brownish greenish sediment, sandy although mixed with clayey nodules (remobilization of the geological substrate).

M20 – [11128]: Filling the inside of the oven. Reddish deposit with varied shades, sandy clay, heterogeneous, medium compact and medium grain. Corn peaks of coal, nodules of green and red clay and rubefacta building ceramics.

M21- [1134]: Landfill. Brown, sandy loam, heterogeneous, medium grain and medium compact. Includes nodules of yellowish clay, brown, orange-green, mortar bags, coal peaks, white stucco fragments and building ceramics.

M22 / M23 - [1317]: Landfill. Brown deposit, very loose, homogeneous, clayey erinaceous, fine grain.

M24 - [1154]: Filling the inside of the oven. Brownish deposit with green and reddish clay nodules, heterogeneous, loose, medium grain, clayey sand. With inclusions of large amounts of white stucco, peaks of coal, construction ceramics and detached glazing of the walls.

M25 / M26 [1402]: Landfill. Dark brown deposit, clay-sandy, coarse grain, heterogeneous, compact. With peaks of coal and small stones.

M27 / M28 [1605]: Filling of graves. Yellowish-brown deposit, loose fine / medium grain, not very compact, homogeneous, clay-sandy.

M29 - [1489]: Filling of grave. Dark brown, clayish, medium-compact, fine-grained, homogeneous deposit.

M30 / M31 - [1402]: Landfill. Dark brown, clay-sandy deposit, coarse grain, heterogeneous, compact. With peaks of coal and small stones.

M32 - [30]: Filling of graves. Yellowish-brown deposit, clayey, homogeneous, medium grain, medium-compact, with peaks of coal and greenish nodules and clay.

M33 – [157]: Filling of grave. Brown deposit with medium grain, not very compact and with peaks of yellowish, heterogeneous, argillaceous,

M33 – [157]: Filling of a grave. Grey-brown deposit with yellowish nodules, heterogeneous, clay-sandy, medium grain, not very compact and with peaks of coal.

M34 / M35 - [60]: Filling of graves. Grey-brown deposit with yellowish nodules, heterogeneous, clay-sandy, medium grain, not very greyish compact and with peaks of coal.

M36 - [1000]: Landfill. Yellowish brown, heterogeneous, medium grain, sandy argi, not very compact and with peaks of coal.

2.2. METHODOLOGY

2.2.1. X-RAY FLUORESCENCE ANALYSIS

The elemental analyses of the coins have been performed with a Bruker TRACER III-SD handheld spectrometer equipped with a rhodium tube and silicon drift detector. The operating conditions were 40 kV and 12.5 μ A current with an Al/Ti filter (304.8 μ m aluminum/25.4 μ m titanium) and 60 s acquisition time. Bruker S1PXRF v.3.8.30 software has been used for the acquisition of the spectra. In order to obtain compositional data on the original bronze alloy without removing the surface patinas, the EDXRF analyses were combined with XRMC-MC

Simulations later on.

After the mechanical surface cleaning of selected samples elemental analyses of the coins have been repeated with a Bruker TRACER III-SD handheld spectrometer equipped with a rhodium tube and silicon drift detector. The operating conditions were same as before, 40 kV and 12.5 μ A current with an Al/Ti filter (304.8 μ m aluminum/25.4 μ m titanium) and 60 s acquisition time. Bruker S1PXRF v.3.8.30 software has been used for the acquisition of the spectra.

2.2.2. X-RAY DIFFRACTOMETER TECHNIQUE AND μ XRD

Coins were analysed without any sample preparation. Bruker AXS D8 Advance diffractometer with DAVINCI design, equipped with Cu K α radiation source, a Göbel mirror assembly and LynxEye 1D detector, and operating with DIFFRAC.SUITE software package. The identification of the peaks for mineralogical composition, Bruker Eva Software in the X-Ray diffraction equipment was used.

2.2.3. SCANNING ELECTRON MICROSCOPE

For these work 37 coin samples were analysed in variable pressure mode. Variable Pressure Scanning Electron Microscope HITACHI S-3700N operated with an accelerating voltage of 20kV to collect X-Ray emissions from heavier elements. The coins were analysed under an air pressure of 40 Pa in the chamber. Compositional analysis performed in the same conditions, using a Bruker XFlash 5010 Silicon Drift Detector (SDD) with a resolution of 122eV at Mn K α . The Esprit 1.9 software from Bruker Nano GmbH Berlin, Germany was used for EDS analysis. For every coin, three different areas selected and SEM-EDS results were collected.

2.2.4. MONTE CARLO SIMULATION



Figure 6: Parameters used for the Monte Carlo simulation

Parameters, which used for the simulation, can be seen above (Figure 6) and with the describe parameters the simulated EDXRF spectra can be seen below (Figure 7).



Figure 7: End results of simulation

OriginPro was used to process the results that were obtain from the simulation. Original and simulated spectra were imported and graph plotted. The black line is belong to original spectra and the red one is simulated one (Figure 8).

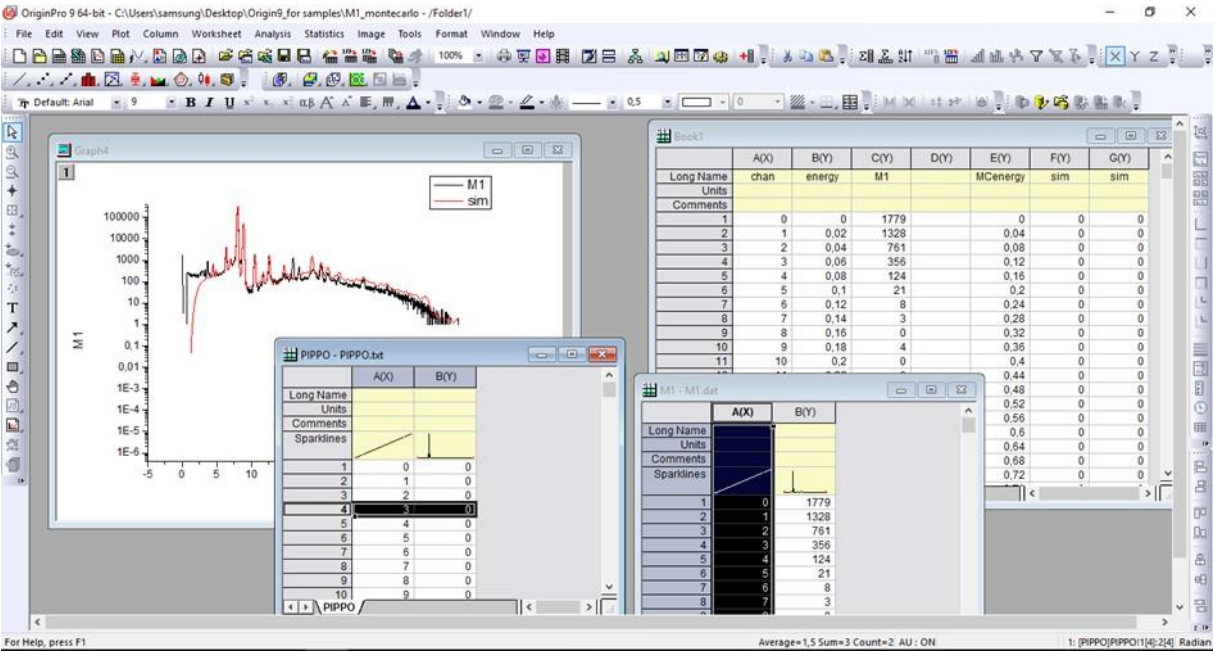


Figure 8: OriginPro during processing the simulation results for M1

```

composition_coin.dat - Not Defteri
Dosya Düzen Biçim Görünüm Yardım
; Composition file
;
Newdevice composition          ; Device type
Composition                    ; Device name

Phase Air                      ; Air
NElem 3                        ; Number of atomic species for this phase
7 76.000000                   ; Atomic number, weight percent of 1st element
8 23.000000                   ;
18 1.000000                   ;
Rho 0.000010

Phase Oxide
NElem 4
6 7.0
8 78.2
26 0.01
29 28.0
Rho 2.0

Phase Bronze
NElem 8
6 39.0
22 14.0
26 1.0
29 38.0
33 0.15
51 0.3
79 0.02
82 0.1
Rho 3.0

End

```

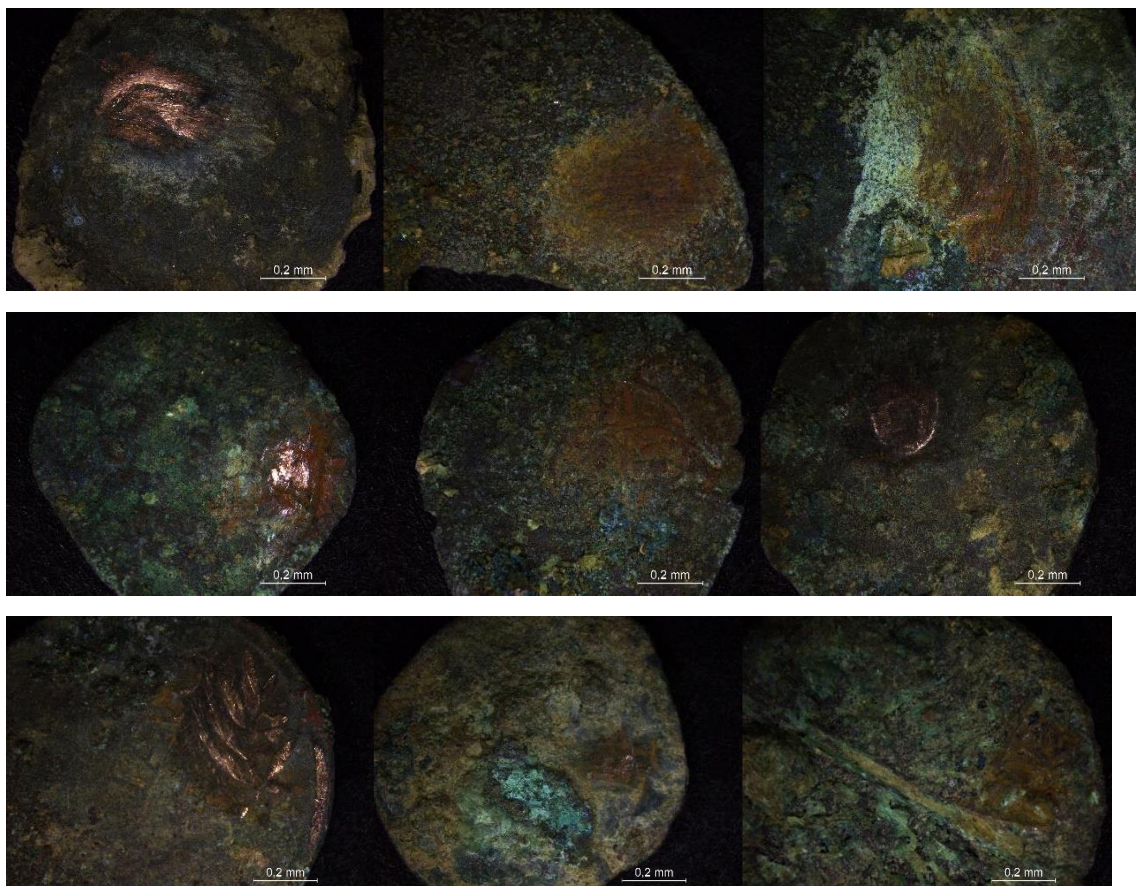
Figure 9: Composition_coin.dat file

The coins were presented to simulation as a two layer. One is the bulk (phase bronze) and the other is patina (phase oxide). The first column is the atomic number of the elements and the second one is the percentage in the patina or the bulk. During the every trial second column was updated according to matches with the original EDXRF spectra. Oxide layer has carbon, oxygen, copper and iron. Titanium, iron, copper, arsenic, silver, antimony, gold and lead were describe for the bulk composition.

2.2.5. MECHANICAL CLEANING OF THE COPPER COINS

The aim of the mechanical cleaning is to remove soil related incrustations, cuprous chlorides and reduce some of the corrosion products back to a metallic state. The mechanical cleaning is only applicable on objects with a metallic core. With careful application of the treatments, metal objects might stabilize and maintain a form closer to their original, corrosion-free appearance. If the procedures of cleaning is not followed with caution, the metal core might be scrape off with the corrosion layer. Tool marks, engraved lines, decorative elements and original shape of the object also can be affected by the misapplication of the procedures. (Hamilton D., 1999) (Methods for Conserving Archaeological Material from Underwater Sites)

After the general surface observation, each one of them underwent investigative cleaning under the microscope. To clean the coins, stainless steel scalpel and glass slide were used. The metal scalpel leaves residues on the surface during the cleaning, which can be confuse with the metals from the coin. To overcome this problem, glass slides used to clean remainings behind the scalpel.



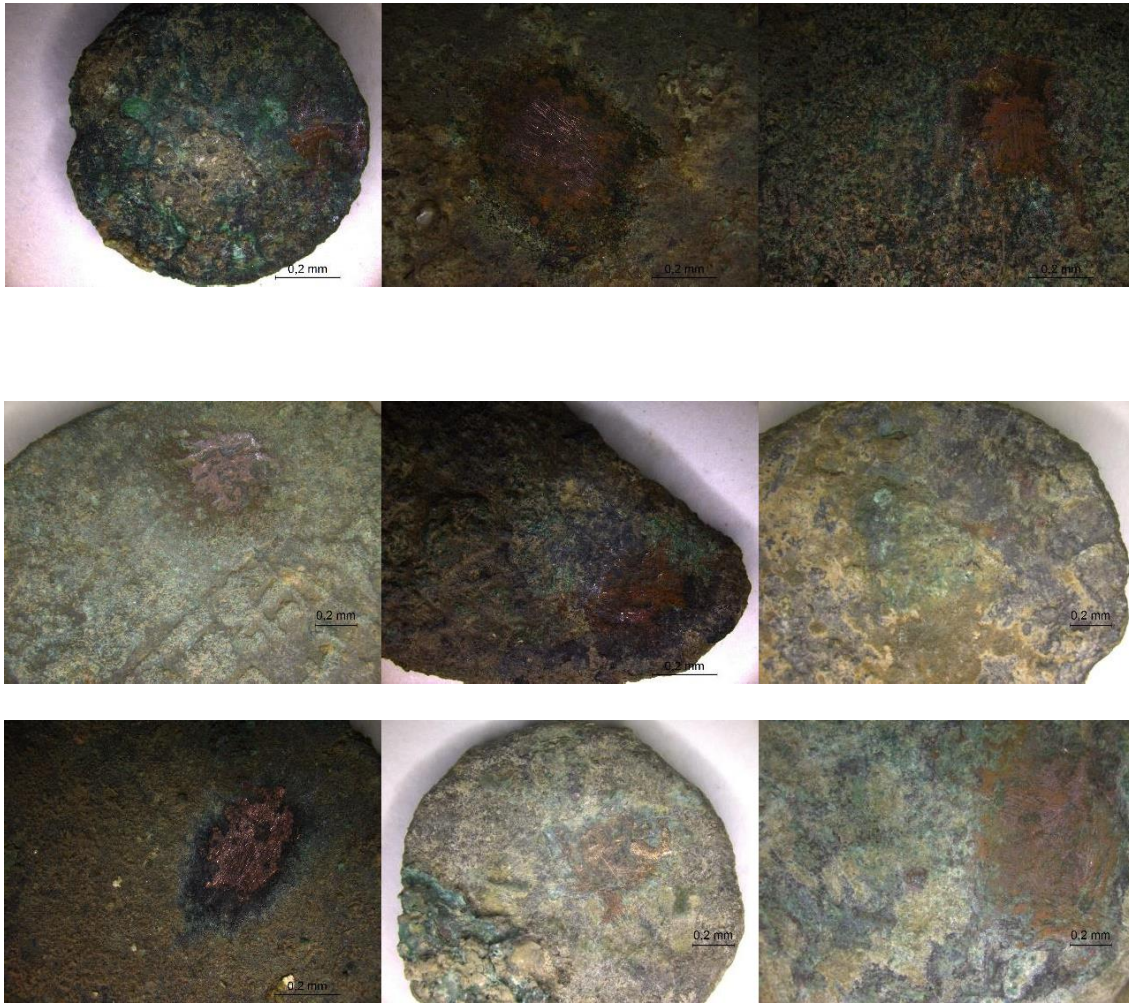


Figure 10: Optical microscope images of cleaned samples. From left to right: M1, M2, M3, M4, M5, M7, M8, M9, M12, M16, M17, M18, M19, M20, M23, M24, M26, M37

3. RESULTS AND DISCUSSION

3.1. μ XRD

All artefacts were covered by a brownish carbonate soil derived crust and a green oxidized corrosion patina that was firstly characterized by μ XRD. The results revealed that crystalline phases of the patina are mainly composed of cuprite (Cu_2O) and atacamite ($\text{Cu}_2\text{Cl}(\text{OH})_3$). The occurrence of quartz (SiO_2) and calcite (CaCO_3) can be a result of contamination from the soil. SEM-EDS investigation also allowed to characterize the superficial layers consisting of both

corrosion patina and soil-derived products, highlighting the difference with the bulk metal composition.

Since the coins were not chemically or mechanically cleaned, minerals from the soil were observed on all of the samples. While quartz (SiO₂) is the one found on every sample, there were other minerals found on different samples that are linked to the soil layer, where the coins were buried until the excavation. As mentioned earlier soil composition has a big influence on corrosion process but finding the corrosion mechanism affected by the soil properties is not the main objective of this work.

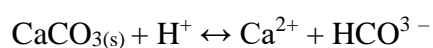
Table 5 List of minerals found on coins patina

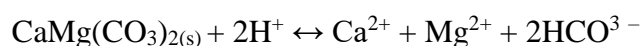
	Quartz	Muscovite	Kaolinite	Calcite	Dolomite	Montmorillonite	Albite	Biotite	Illite	Olivine	Gypsum	Anorthoclase	Gehlenite	Ankerite	Sanidine	Aragonite	Magnesium Silicate	Sodium Magnesium Aluminium Silicate	Magnesium Calcite	Sodium Magnesium Titanium Oxide
M1	X	X	X	X																
M2	X			X	X															
M3	X				X		X	X												
M4	X			X	X	X														
M5	X			X	X															
M6	X		X						X											
M7	X			X	X															
M8	X	X									X									
M9	X			X			X													
M10	X	X		X																
M11	X								X										X	
M12	X												X							
M13	X			X																
M14	X			X										X						
M15	X			X	X										X					
M16	X			X										X						
M17	X			X				X												

M18	X							X											
M19	X			X															
M20	X			X				X						X					
M21	X																		X
M22	X	X																	
M23	X	X																	
M24	X			X															
M25	X																		
M26	X																		
M27	X			X					X										
M28																			
M29	X							X			X								
M30	X			X	X														
M31	X			X	X														
M32	X																		
M33	X	X		X														X	
M34	X				X														
M36	X			X														X	
M37	X	X																	

On the patina quartz is found on every sample, which is the most common one to be found in the Earth's crust. It is also a significant component of many igneous, metamorphic and sedimentary rocks (<http://www.minerals.net/mineral/quartz.aspx>). Calcite (CaCO_3), a calcium carbonate related with copper objects in sea or land burials is the second most common soil mineral after quartz. It is found on the M1, M2, M4, M5, M7, M9, M10, M11, M13, M14, M15, M16, M17, M19, M20, M20, M27, M30, M31, M33, and M36. From the carbonate group another mineral, dolomite ($\text{CaMg}(\text{CO}_3)_2$), was also found on the patina. The carbonates dissolve in the groundwater overtime and keep the groundwater solution in the neutral to alkaline pH range. When metal surface is exposed to this solution, it precipitates on the surface in the form of hard white carbonate and act as a protective layer (Dong et al., 2000). M2, M3, M4, M5, M7, M15, M30, M31, M34 are the analysed coins that dolomite.

Dissolution/precipitation of carbonates occurs according to the following reactions:





Ankerite (Ca (Fe, Mg, Mn)(CO₃)₂) is a carbonate and has a very similar composition to dolomite found on the M14, M16. From the mica group muscovite, biotite and illite were found on the corrosion patina. The samples M1, M8, M10, M22, M23, M33, M37 have muscovite, M17, M18, M29, M30 have biotite and finally M6, M11, M20 have illite. For the M10, the muscovite peak is not matching exactly. This phenomenon can be explained by the special orientation of the mineral (Farquhar et al., 1997). Sanidine K(AlSi₃O₈) and albite Na(AlSi₃O₈) from the feldspar group minerals were also identified on the soil crust of the coins. Both are not very common minerals for the analysed copper coins. While albite was only found in three samples (M3, M9, M32), sanidine was found only in one (M15). Other rare minerals that were found on the patina are kaolinite (Al₂(Si₂O₅)(OH)₄) (M1 and M6), gypsum (CaSO₄ · 2H₂O) (M8), gehlenite (Ca₂Al(AlSiO₇)) (M12) and montmorillonite ((Na,Ca)_{0.33}(Al,Mg)₂(Si₄O₁₀)(OH)₂ · nH₂O)(M₄).

Table 6 List of corrosion products found on coins patina

	Copper	Cuprite	Tenorite	Atacamite	paratacamite	malachite	buttgembachite	copperchloridehydroxide	connellite	nantokite	digenite	copper zinc	copper gold zinc	chalcocite	Silver	silver oxide nitrate	magnesium silver	chlorargyrite	Iron oxide/wuestite/wustite	magnetite	cerrusite	potassium arsenate
M1	x	x																	x			
M2		x		x											x							
M3		x		x																		
M4		x		x	x														x			
M5		x		x	x																	
M6	x	x			x				x	x												
M7		x		x						x							x					
M8		x		x						x		x										

Cuprite (Cu_2O) is the red coloured copper oxide is found all of the coins, except M13, M16, M28, M34, M35 and M36. It is the first corrosion product of form on copper alloys when they react with the gaseous environment. It acts as a chloride exchange layer for the copper surface and actively participate in a secondary corrosion cycle. Diffractometry results showed that the corrosion patina has predominantly cuprite and substantial copper hydroxide chloride (mainly atacamite and paratacamite). These formation does not develop under anaerobic conditions but it is possible that the chloride ions had an accelerating influence (Tylecote, 1979).

Tenorite (CuO) was found on the M20 and M23. As previously mentioned, cuprite is the first patina layer on the copper and copper alloys. When the cuprite film continuous to grow on the surface, small black spots of tenorite starts appearing on the surface and then it spreads over the entire surface. On the Figure 11, it can be seen visually under the optical microscope. It is a rare corrosion product but the existence of it on the surface shows that the coins either before or during the burial were subjected to heating (Scott, 2002).

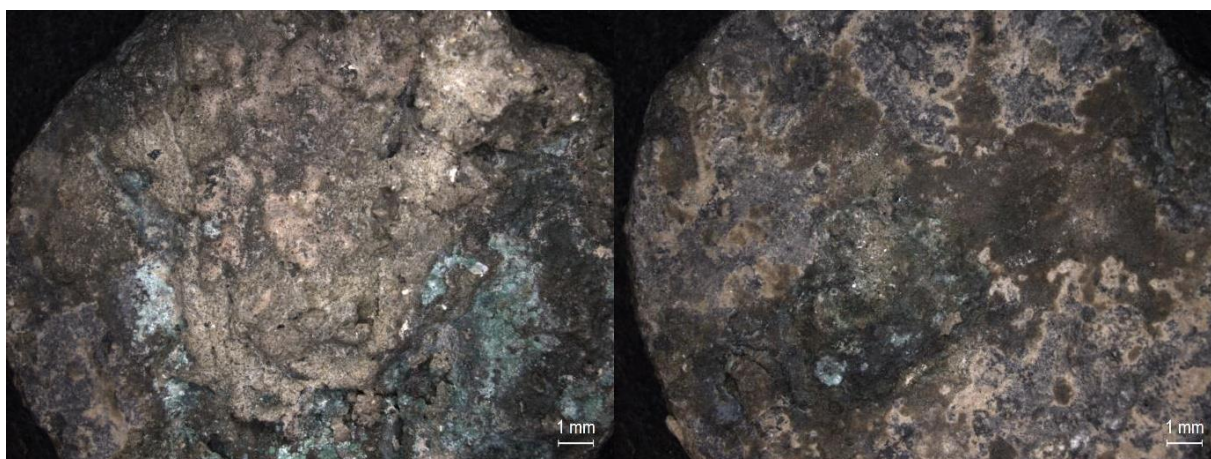
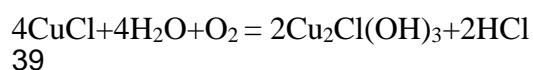


Figure 11: Optical microscope image of M23

Atacamite ($\text{Cu}_2\text{Cl}(\text{OH})_3$) (Figure 12) is the most common basic copper chloride on the corrosion patina for all the coins except M1, M6, M23 and M33. The green coloured atacamite forms on copper alloys exposed to an aerated marine environment (MacLeod, 1991). The autocatalytic reaction occurs, when the outer corrosion layers are removed from the surface which is the result of the contact of moisture with the cuprous chlorine layer (Walker, 1980). The reaction is known as bronze disease, which leads to the formation of paratacamite/atacamite.



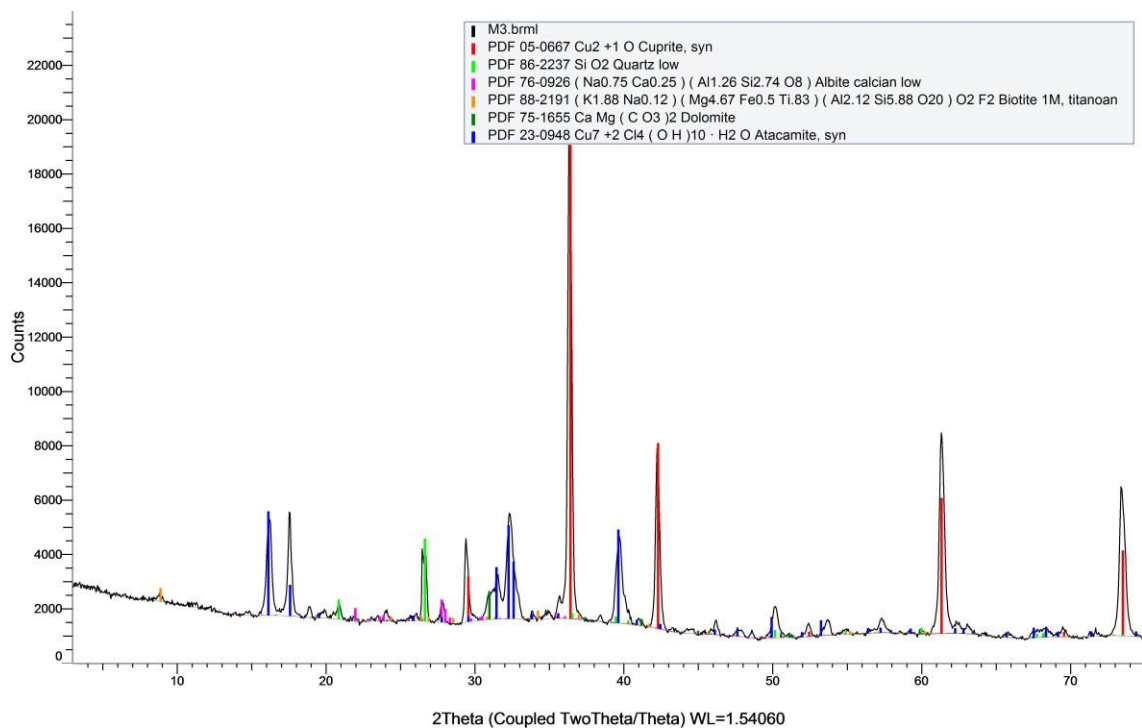


Figure 12: μ XRD pattern of M3

Another copper chloride hydroxide, paratacamite ($\text{Cu}_3(\text{Cu},\text{Zn})(\text{OH})_6\text{Cl}_2$) was also found on the samples M4, M5, M6, M9, M10, M11, M18, M21, M34 and M36. Atacamite and paratacamite were formed after a long contact period with a soil rich in chloride content at a high moisture level. They can also be formed as original corrosion products or as transformation products from nantokite, which oxidizes to red cuprous oxide cuprite and bright green atacamite. The atacamite often is altered to a paratacamite, they are identical in chemical composition but differing in crystal form. While atacamite is orthorhombic, paratacamite is rhombohedral (Ghoniem, 2011).

Nantokite (CuCl) was identified on the M6, M7, M8 and M21. Its colour, pale grey, was observed on the optical microscopy images. Because of the acidic conditions, nantokite patina is very rare for marine copper alloys (Cramer and Covino, 2006). Nantokite patina can cause a bronze disease, which can be defined as “the process of interaction of chloride-containing species within the bronze patina with moisture and air” (Scott, 1990) and also as “a progressive deterioration of ancient copper alloys caused by the existence of cuprous chloride (nantokite) in close proximity to whatever metallic surface may remain” (Scott 2002). Bronze disease is essentially a process that nantokite (CuCl), converts to one of the trihydroxychlorides

(atacamite or its dimorph paratacamite). Malachite ($\text{Cu}_2\text{CO}_3(\text{OH})_2$), copper carbonate was found on the corrosion patina of samples M9, M32, M34 and M37. Formation of malachite on the surface of copper alloys is very common because of the reaction between copper and carbon dioxide gas from humid air or dissolved ground waters percolating through damp soil (Scott, 2002). When it grows uniformly on the surface, the attractive green patina can be observed. On the OM photo of the M9 (Figure 13), it can be seen.

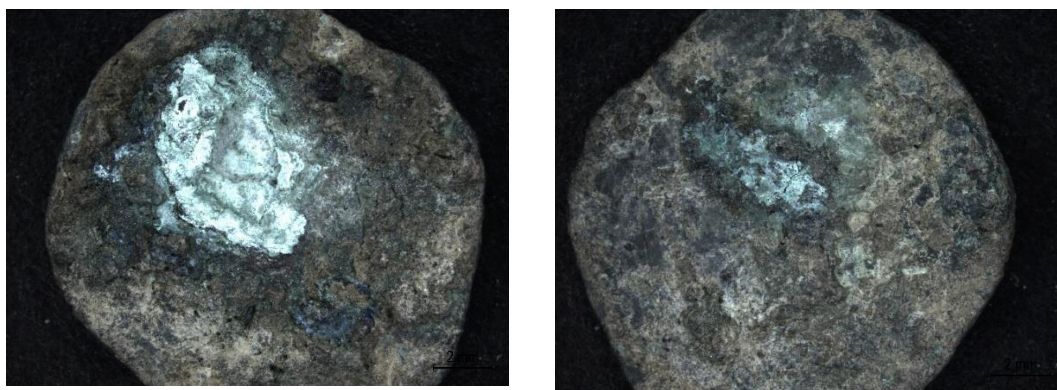


Figure 13: Optical microscope image of M9

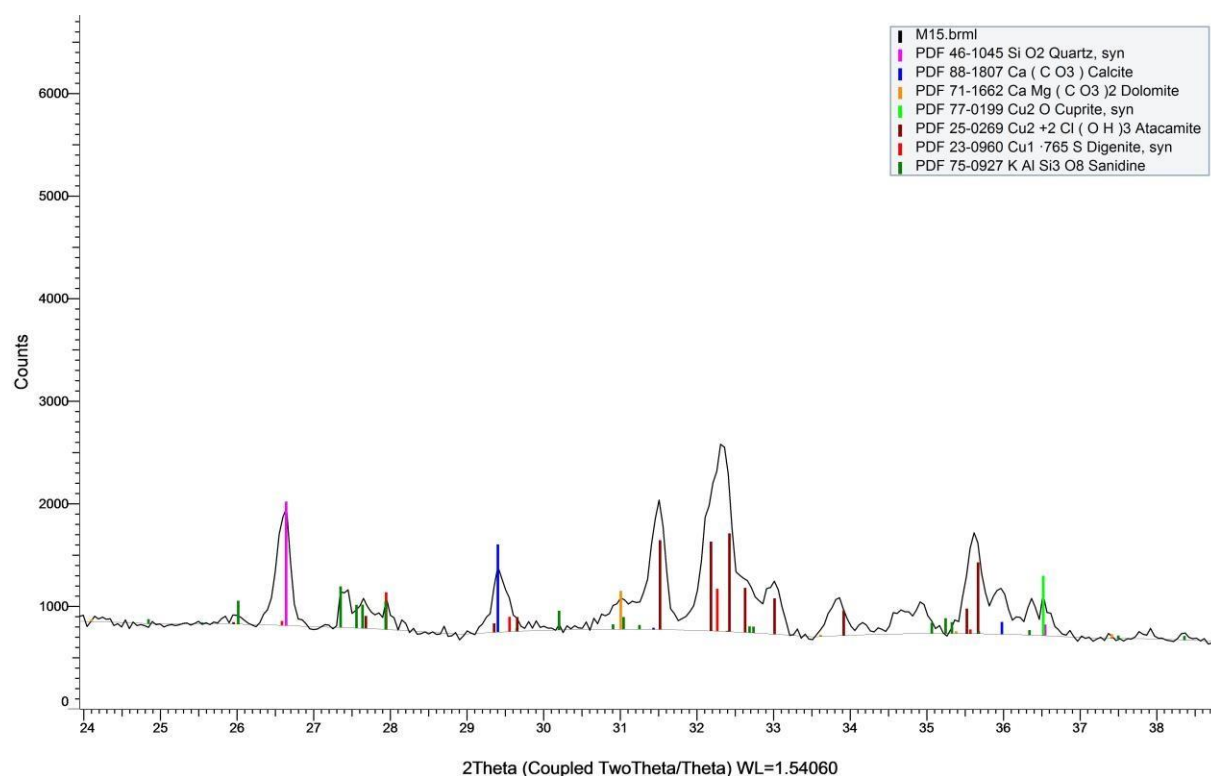


Figure 14: μ XRD pattern of M15

Copper sulphides namely chalcocite (Cu_2S) (M20), covellite (CuS) (M23) and digenite ($\text{Cu}_{1.8}\text{S}$) (Figure 14) (M15, M16 and M28) were also detected on the corrosion patina. There might be two possibilities to explain the presence of copper sulphides: bacterial activity or copper ores.

If the source of copper has S, it is common to detect copper sulphides. Although later with XRF analysis, no trace levels of S were found in the composition which means that bacterial activity is the reason. In burials, if the sulphate reducing bacteria (SRB) is existent, sulphide ions are produced. SRBs grow in near-neutral, anaerobic environments and promote reduction of present sulphate to sulphide. On the metal surface, SRB consume hydrogen atoms produced at cathodic sites and reduce sulphate ions to sulphide ions then the sulphide ions react directly with metal ions to form metal sulphides (Dexter, 2003). Connellite ($\text{Cu}_{19}(\text{OH})_{32}(\text{SO}_4)\text{Cl}_4 \cdot 3\text{H}_2\text{O}$) a copper sulphate was found on the corrosion patina of M5 and M27. Copper sulphites on the patina might transform into sulphate by oxidation after the coin is removed from the burial environment which might be the explanation for the presence on the patina. Also occurrence of connellite with the copper trihydroxychlorides is an evidence for saline environment crystallization (Scott, 2012). Buttgenbachite ($\text{Cu}_{19}(\text{NO}_3)_2(\text{OH})_{32}\text{Cl}_4 \cdot 2\text{H}_2\text{O}$), which is a complex hydroxyl nitrate was formed on the M24. Its molecular structure is very similar to connellite, while they have subtle differences in their X-ray structure (Frost et al. 2003).

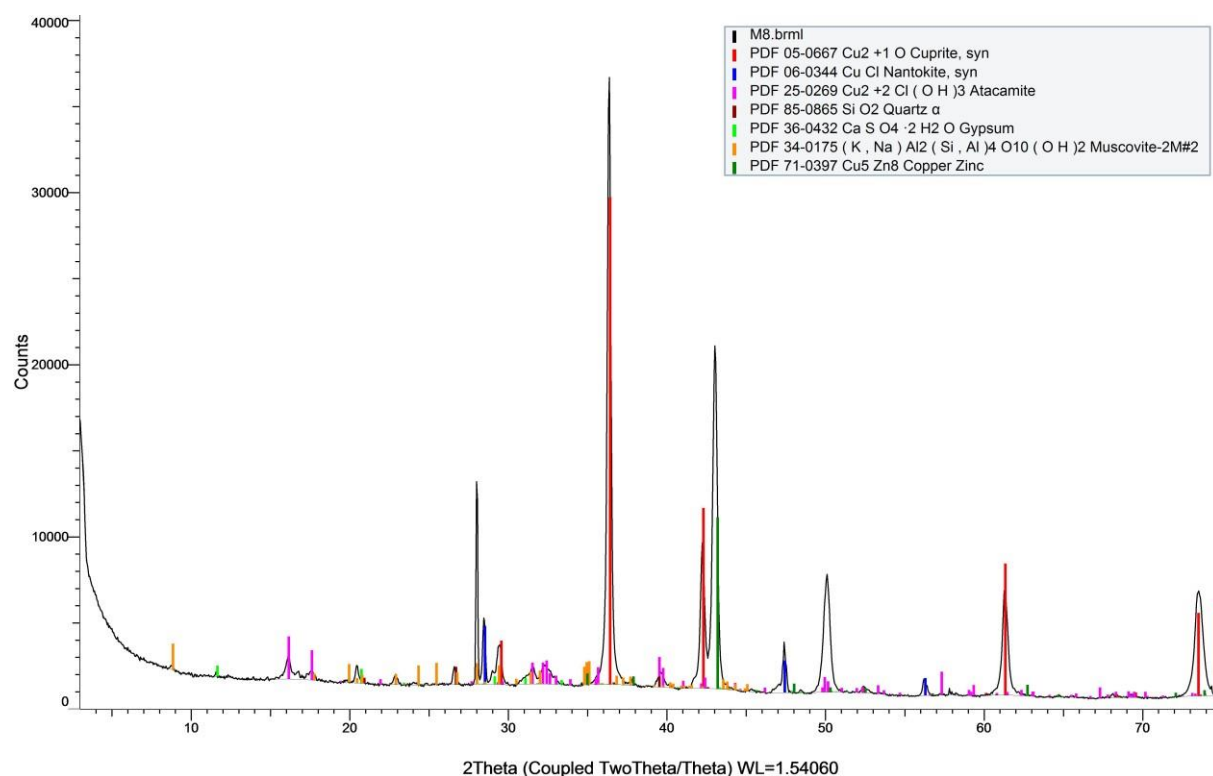


Figure 15: μ XRD pattern of M8

Copper - zinc (Cu_5Zn_8) is found on the M8 (Figure 15), which is the latest coin studied from the Republic and for the modern coins, zinc is very common element to be found. Zinc is also

found on the M21 in the form of $\text{Au}_{0.18}\text{Cu}_{0.37}\text{Zn}_{0.45}$. Later on, XRF confirmed the presence of zinc in the structure of M8

Pure copper was only observed on M6. After some selected samples were partly cleaned and analysed under XRF, it was found that most of the coins are made from copper only. The patina restrictions did not allow us to identify pure copper for the rest of the coins with μXRD .

Iron oxides (FeO), wuestite and wustite were found in samples M1, M4, M9, M16, M24, M27, M30, M37 as a corrosion products. Wustite (FeO) as a first layer might form under the magnetite (Fe_3O_4) layer. Only M32 has the formation of black coloured iron oxide, magnetite. (Grobner et al., 1980). It is known that copper and iron cannot be alloyed alone but existence of zinc in the composition can make the alloying possible, in case of the modern alloys (<https://fiskalloy.wpengine.com/wp-content/uploads/2012/03/C194-Copper-Fisk-Alloy.pdf>) (<https://qph.ec.quoracdn.net/main-qimg-25f0430082794993d29afe7bffa9b5d0>). Since our samples are archaeological artefacts, it is not possible to produce the high performance alloy. The reason for the presence of iron in the both patina and the core can be explained as an impurity from the soil and from the copper ore that were used. On M26's corrosion patina, cerrusite (PbCO_3) is detected, which confirm present of the lead on the alloy and during the corrosion process, lead was carbonated and formed the cerrusite.

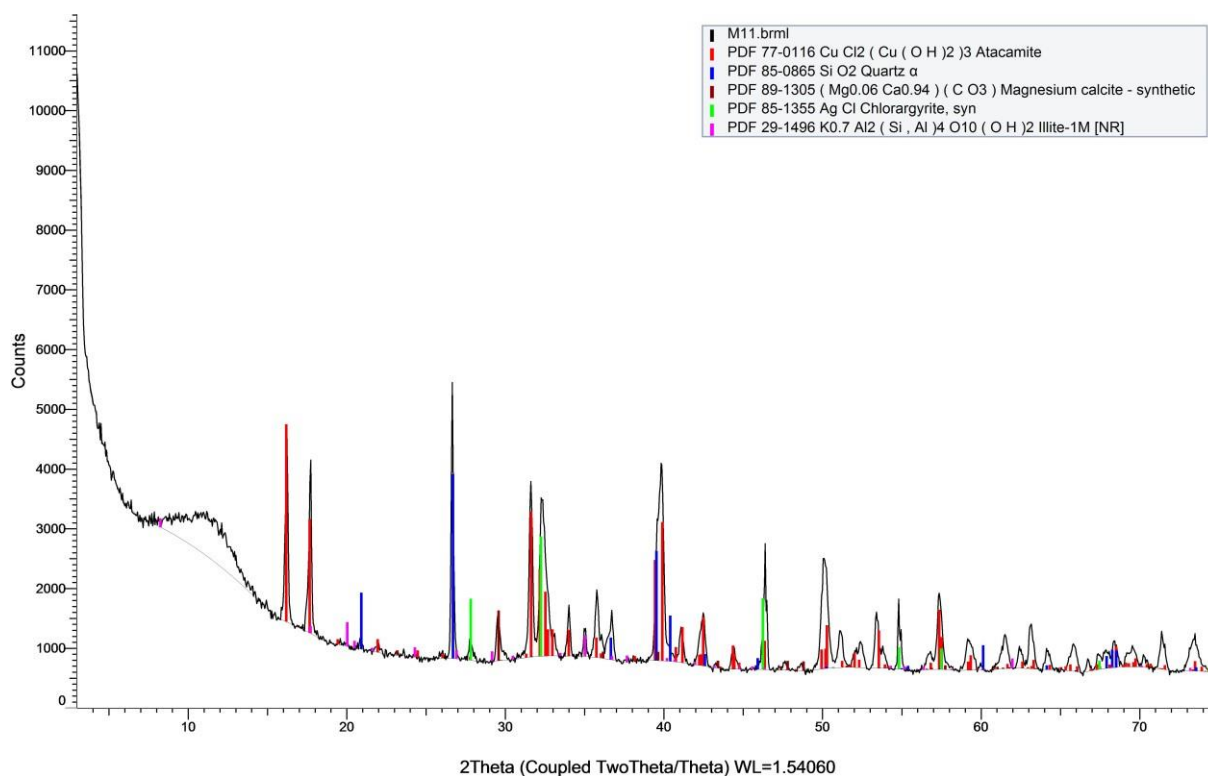


Figure 16: μ XRD pattern of M11

Historically it is known that silver-copper (billon) alloys were used to make Portuguese coins but for the samples that were studied, presence of silver was not common. Only 5 samples had silver or silver compounds. A small amount of pure silver was found only on M2. Other silver corrosion products, magnesium silver (Ag_3Mg) on M7, chlorargyrite (AgCl) on M11 (Figure 16) and M25 and finally silver oxide nitrate ($\text{Ag}_7\text{O}_8\text{NO}_3$) on M28 were also detected. The silver-copper alloys, because of the selective leaching, usually are covered with green copper compounds. Copper in the structure is removed from the alloy and deposited on the surface in the form of malachite or atacamite (Cronyn and Robinson, 1990).

3.2. SEM-EDS

The data obtained through SEM-EDS analyses show mainly the same elemental characteristics. Cl, K, C, O, Ca, Al, Mg, Si, P, Fe and Cu were detected in all samples. As previously indicated, since the samples were not cleaned, the coins have soil-derived minerals on their surface and Cl, K, Ca, Al, Mg, Si and P are the elements which are associated with the soil. In relation to this, the minerals associated with the soil layer; quartz, calcite, dolomite, ankerite, muscovite, biotite, illite, sanidine, albite, kaolinite, gypsum, gehlenite and montmorillonite were already found on μ XRD. Another soil related element, sodium is found on M24 only. With the SEM-EDS, these minerals cannot be specifically identified but their structural elements can be double checked to compare with μ XRD results. As mentioned in the introduction, the archaeological site revealed three main chronological layers with the first layer being the cemetery. Phosphorus, an element related to soil, is encountered abundantly during this study and their source is likely to have been the presence of the cemetery. When bones dissolve, they contribute to the elemental complexity of the soils, enriching it with elements such as phosphorus is one of them (Fabrizi et al. 1989). Furthermore, as indicated by Keeley for other archaeological contexts, fertilizers used in the area could be indicated as another source for the phosphorus (Keeley, 1981). On the other hand because the excavated area was an urban site, the fertilizers are out of consideration. For our samples, μ XRD did not detect any copper phosphates. It can be concluded that, the high P is from the soil and not belong to the corrosion patina.

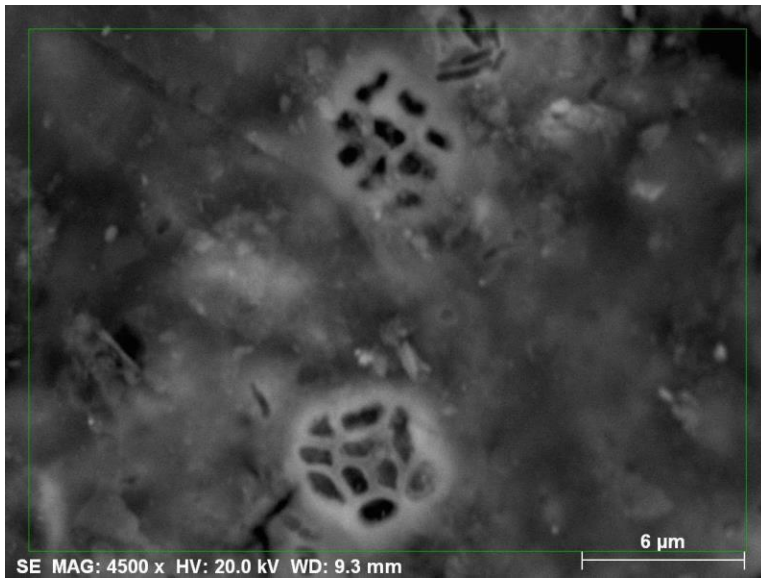


Figure 17: SEM-EDS backscattered electrons image of M1

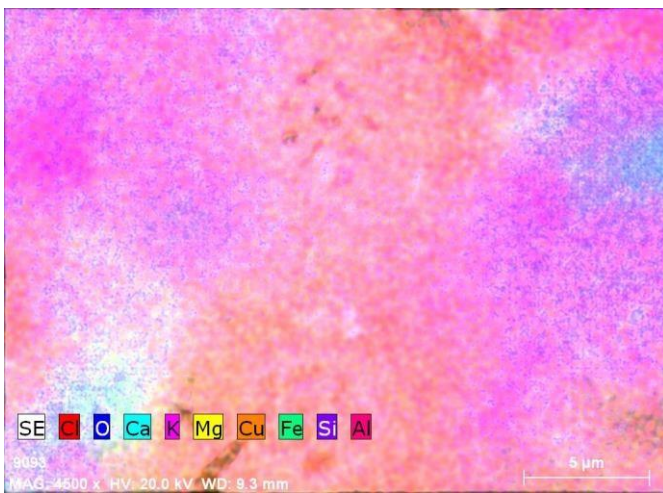


Figure 18: Mapping of M1

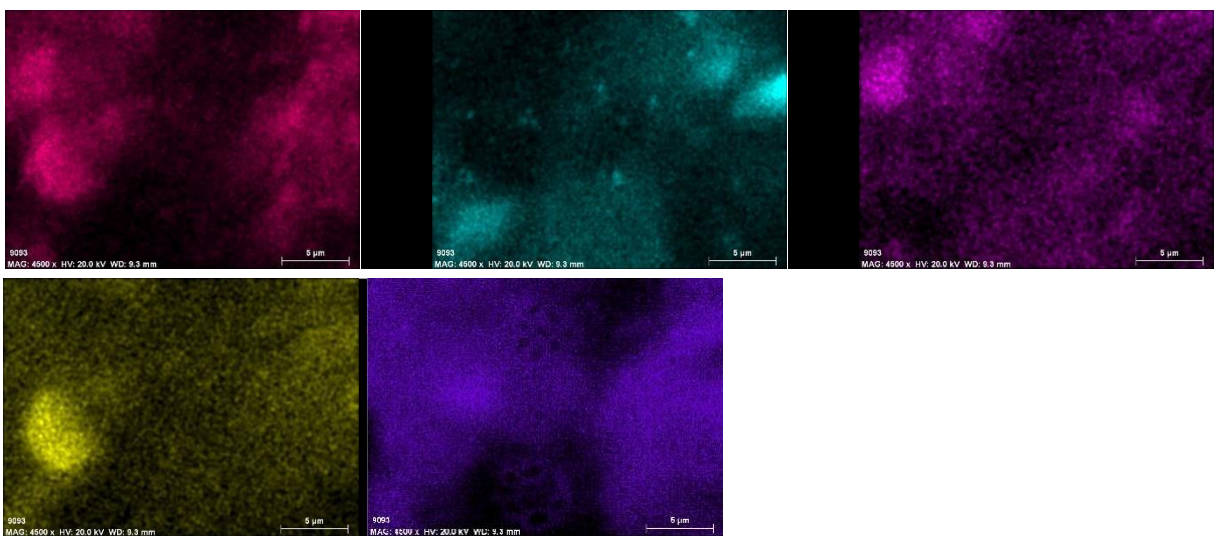


Figure 19: Mapping of five elements (Al, Ca, K, Mg and Si), their particular distribution within a chosen area

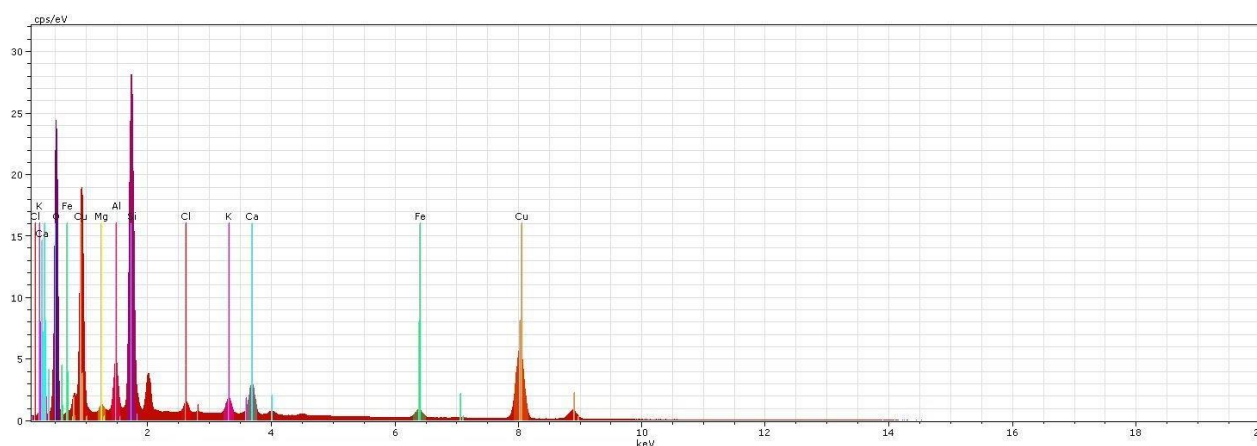


Figure 20: EDS spectrum of M1

In sample M1, quartz, muscovite, kaolinite and calcite are the minerals detected with μ XRD. With the elemental mapping of selected elements, where the minerals concentrate on the selected surface of identified. The violet area (Figure 18) represents quartz, turquoise is calcite, pink is kaolinite and finally purple is the muscovite (Figure 19). Copper chloride, a corrosion product, is not found on μ XRD but with elemental mapping, it can be seen as a reddish-orange on the map. The bright region on the bottom left is the iron oxide, which verifies the μ XRD results of M1.

Atacamite ($\text{Cu}_2\text{Cl}(\text{OH})_3$) was found on the corrosion patina for all the coins except M1, M6, M23 and M33 during the μ XRD analysis. Atacamite, green coloured corrosion product of copper forms on copper alloys exposed to an aerated marine environment (MacLeod, 1991). Atacamite forms after a long contact with rich chloride content soil at high moisture level. It can be secondary corrosion product after copper oxides or transformation product of nantokite, which oxidizes to red cuprous oxide cuprite and bright green atacamite. The atacamite often is altered to a paratacamite, they are identical in chemical composition but differing in crystal form. While atacamite is orthorhombic, paratacamite is rhombohedral (Ghoniem, 2011).

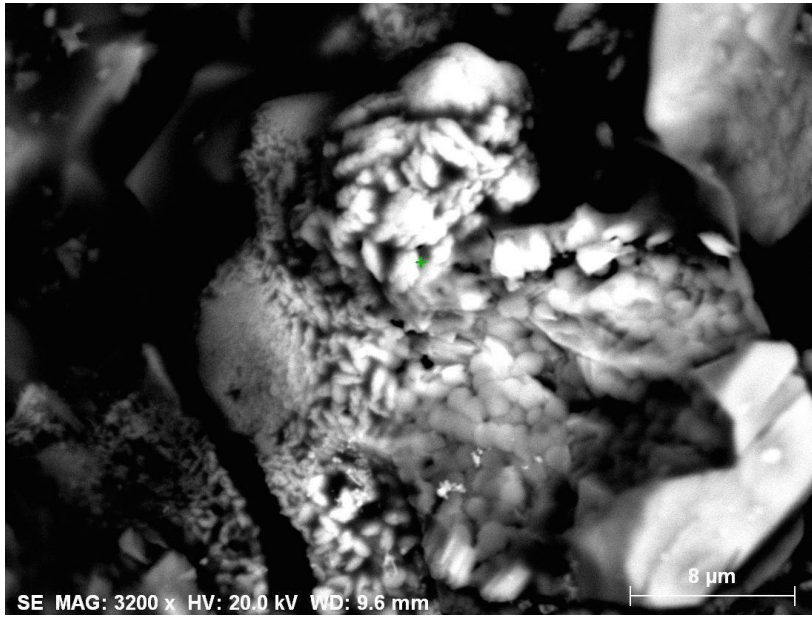


Figure 21: SEM-EDS backscattered electrons image of M11

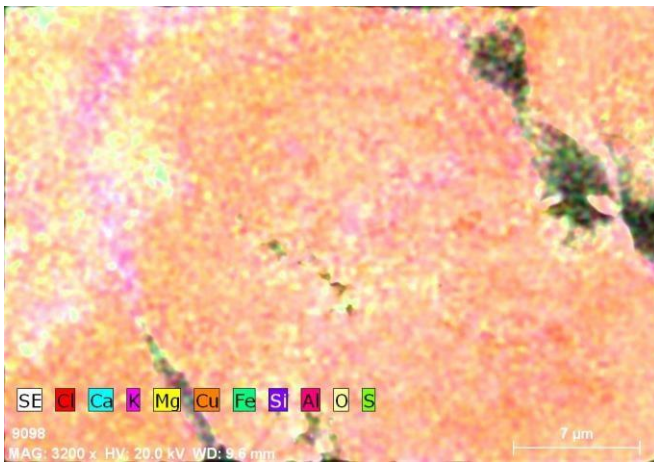


Figure 22: Mapping of M11

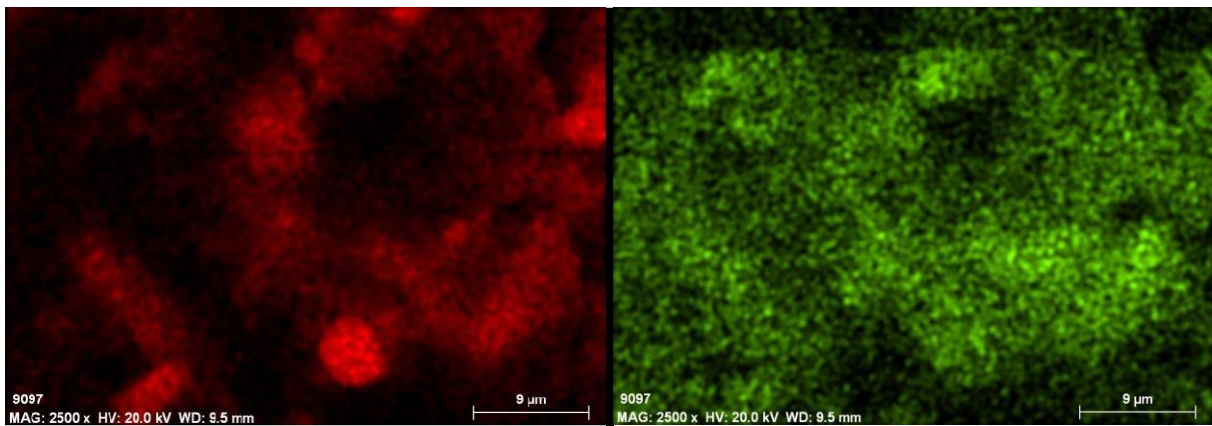


Figure 23: Mapping of two elements (Cl and S), their particular distribution within a chosen area

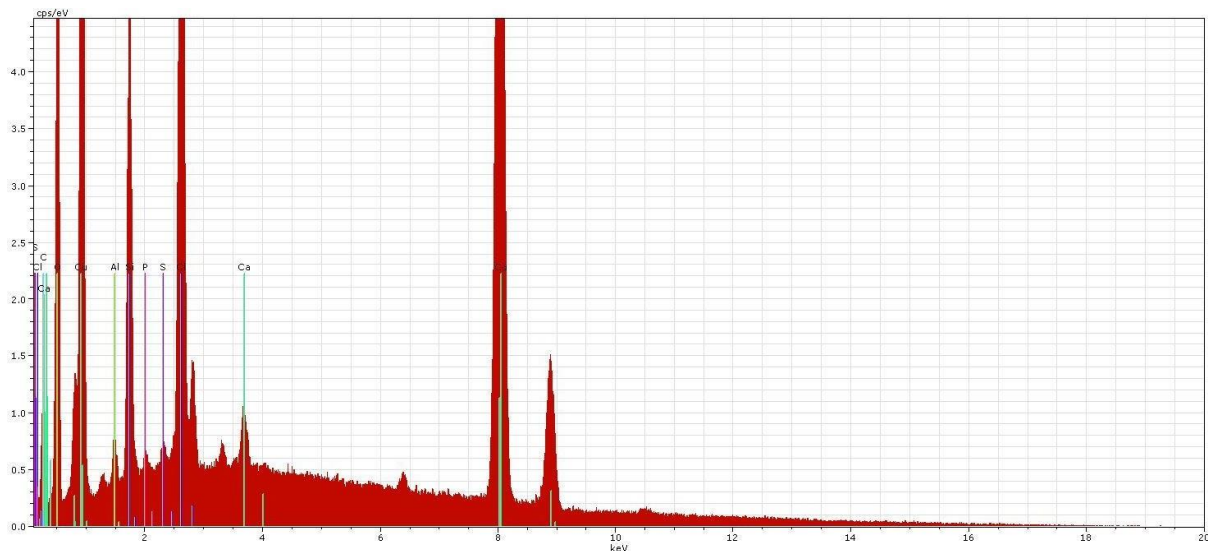


Figure 24: EDS spectrum of M11

The spectrum of M11 reports (Figure 24) that the spot of analysis captured an area consisted of two different corrosion products of copper, copper chloride and copper sulphide that are evident by the presence of high amounts of Cu, Cl and S with silica and other soil-related minerals. The fibrous habit of atacamite can be seen from the SEM image (Figure 23). Atacamite, quartz, magnesium calcite, chlorargyrite and illite are found during the μ XRD analysis. We can confirm the presence of quartz, magnesium calcite, illite and atacamite but unfortunately not chlorargyrite. On the other hand, M11 was one of the cleaned samples and the silver, which has the highest of all, in the composition was confirmed with XRF. Therefore, it was concluded that M11 is actually a silver alloy. Sulphur, the green colour on the map, indicates that the corrosion patina has copper sulphides such as chalcocite, covellite, digenite, djurleite (Schweizer, 1994).

On M15, M16, M20, M23 and M28's patina copper sulphides were detected with μ XRD, which was formed on the surface as a result of SRB activities. More coins with sulphur were found on SEM-EDS: M2, M4, M5, M7, M8, M11, M17, M18, M19, M20, M23, M25, M26, M28, M29, M34 and M35. Which proves that bacterial activity is actually more common than the initial thought. The bacteria grows on a copper's surface and consumes hydrogen atoms produced at cathodic sites and reduce sulphate ions to sulphide ions then the sulphide ions react directly with metal ions to form copper sulphides (Dexter, 2003). Chalcocite (M20), covellite (M23), digenite (M15, M16 and M28) and connellite (M5 and M27) detected on the corrosion

patina with the μ XRD. SEM-EDS shows that S is more common in the patina than initial thought.

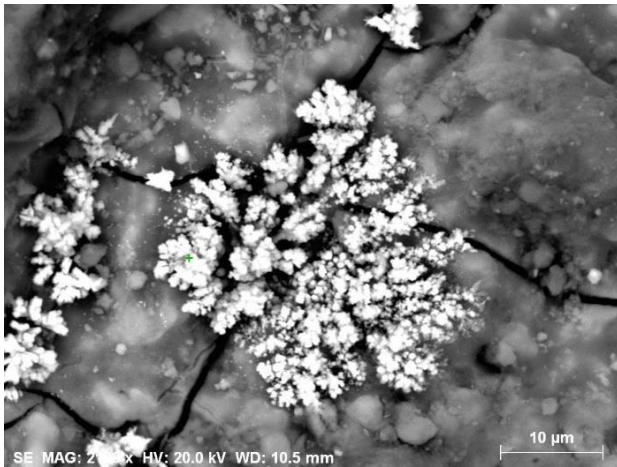


Figure 25: SEM-EDS backscattered electrons image of M19

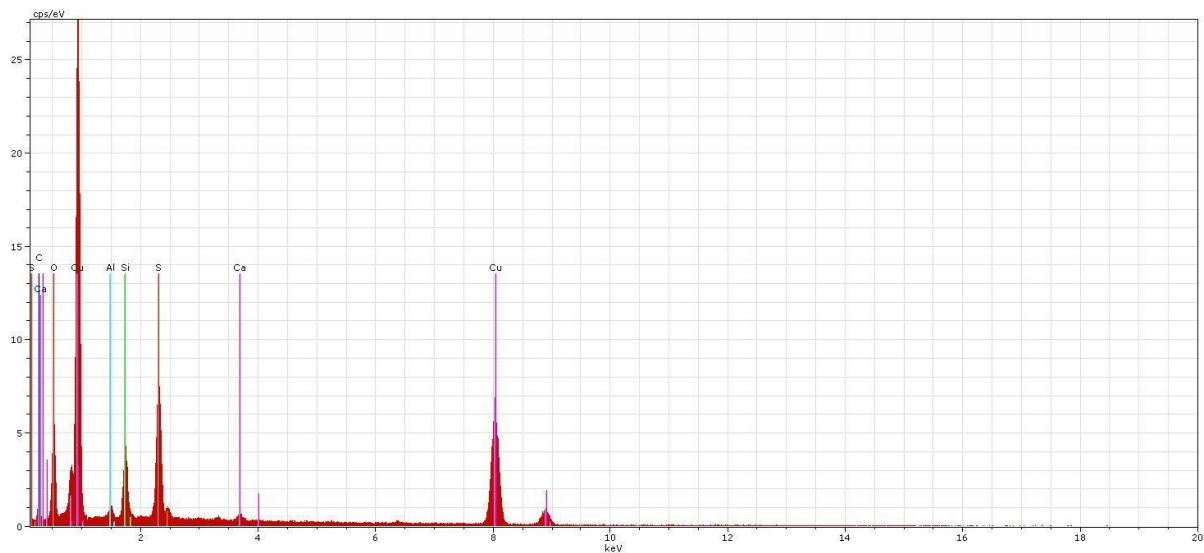


Figure 26: EDS spectrum of M19

EDS imaging shows spot analysis of M19 (Figure 26). The selected spot has high Cu and S, which indicates that the patina has either copper sulphide or copper sulphate. Also high Si and Ca on the EDS spectrum shows silica and calcite are on the outer patina of the coin. For these two mineral, μ XRD also shows the same results but for copper sulphide or copper sulphate not. Selecting different spots for μ XRD and SEM-EDS, might be the reason of different elemental and/or mineralogical analysis for the coins.

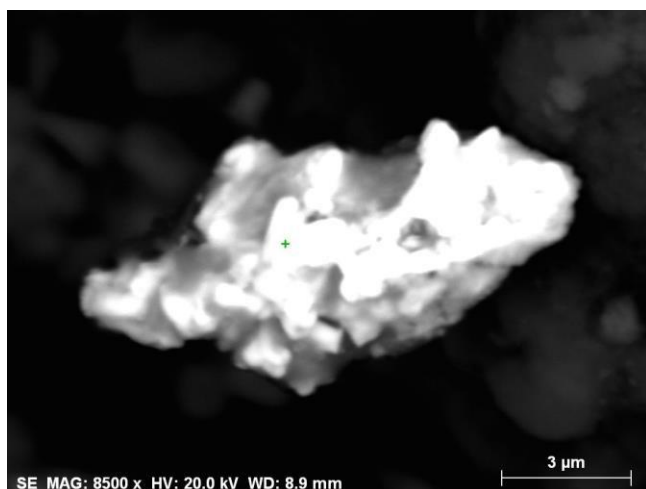


Figure 27: SEM-EDS backscattered electrons image of M19

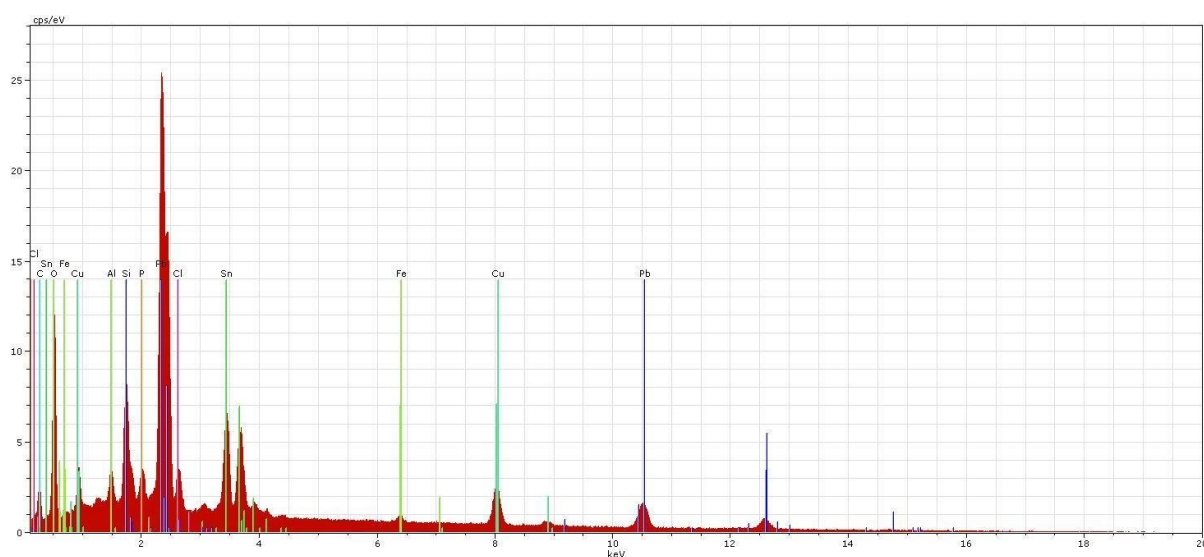


Figure 28: EDS spectrum of M19

Another spot analysis of M19 shows a high amount of Pb and Sn, besides Cu, Al, Si, P, Cl, C, O and Fe (Figure 28). Pb and Sn were detected on the cleaned section of M19 during XRF but both have trace level concentrations so it is concluded that these both were not alloying elements. The SEM image shows the bright lead globule (Figure 27). Cu, Cl, Si and O are the proof of the existence of atacamite, cuprite and quartz on the patina, which is the result from μ XRD.

M13, M14 and M32 have silver in the composition of the coin found from SEM-EDS results, which is different than μ XRD results. Also it does not match with the XRF results of the cleaned samples. The general difference between the samples is that for some of the coins, the period has already been identified while the rest belong to the unidentified type-period-chronology.

These 3 coins belong to second category. Since there were not enough written documents about composition, it might be helpful to identify the coins according to the existence of the silver in the composition. It is well-known that early period of Portuguese coins were made of silver-copper alloy. If the identified silver was an intentional alloying element, the content should increase from the core to the surface to 100% and gradually decreases in the corrosion layers. In the case of billion alloys, silver enrichment on the surface can be observed with time. The selective depletion or the leaching of copper from the surface to form corrosion products is the reason behind this phenomenon (Beck et al., 2008). Unfortunately, M13, M14 and M32, were not chosen for the further cleaning procedures, and therefore no further comments can be made about the original metal composition.

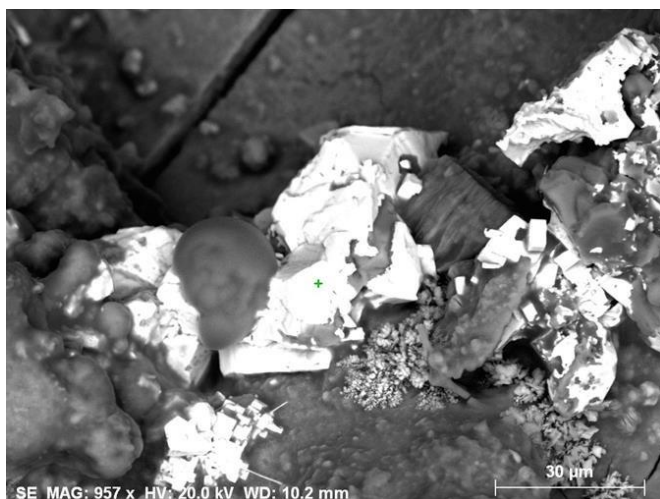


Figure 29: SEM-EDS backscattered electrons images of M32

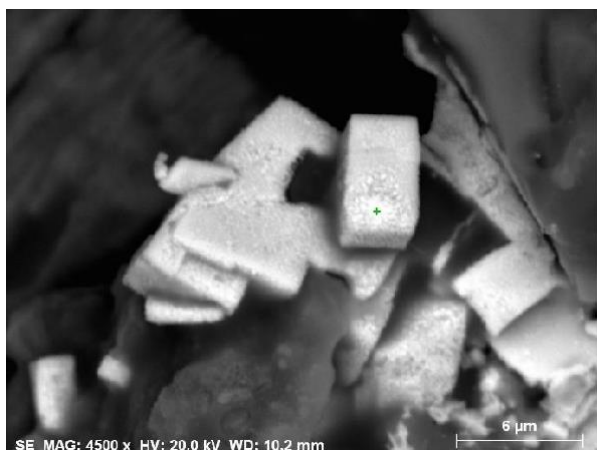


Figure 30: SEM-EDS backscattered electrons images of M32

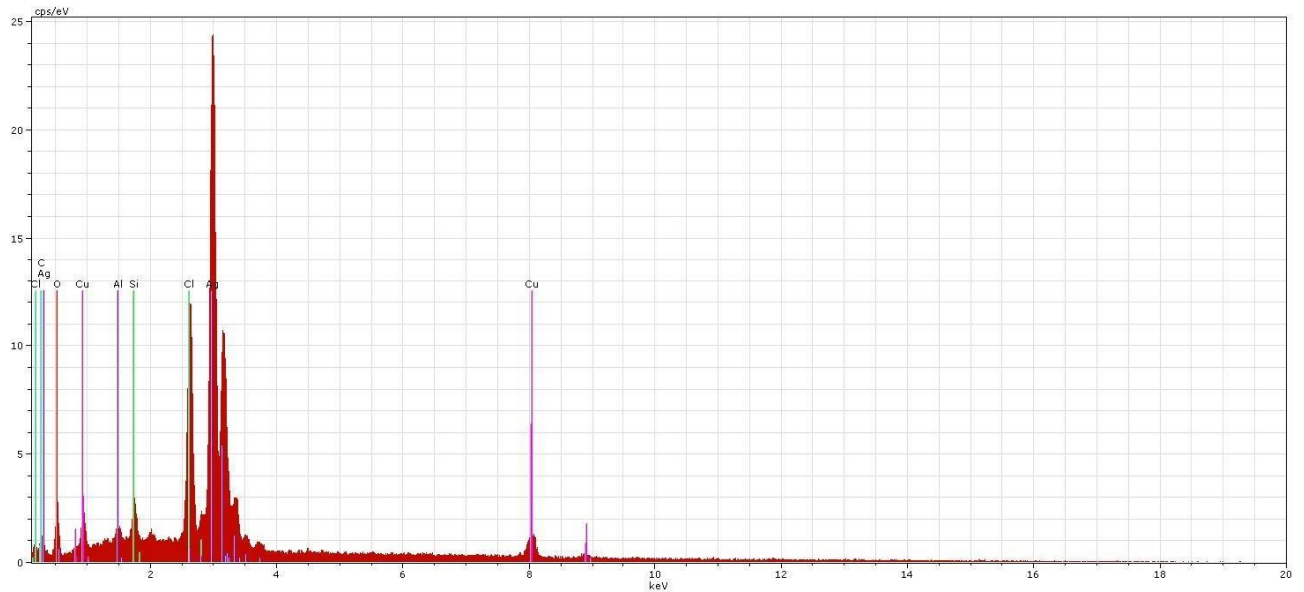


Figure 31: EDS spectrum of M32

In figure 29 and figure 30, SEM-EDS backscattered electrons image and the morphological details and the surface chemical composition of the patina of M32 can be seen. This finding is confirmed by the μ XRD diffraction pattern in the case of atacamite, silica, cuprite and malachite but not for Ag.

Titanium was found on M6, M9, M20, M23, M25, M26, M29 and M36. For the later Monte Carlo simulations, titanium was simulated in the alloy phase but not on the patina. It is likely for the titanium peak to be a copper escape peak at 4.51 keV but it might also indicate the presence of trace quantity of the element, where titanium $K\alpha$ energy is the same as the copper escape peak. For M20, same case was observed also for chromium, but it cannot be distinguished if it is an escape peak or a trace element (Couture-Rigert et al., 2012).

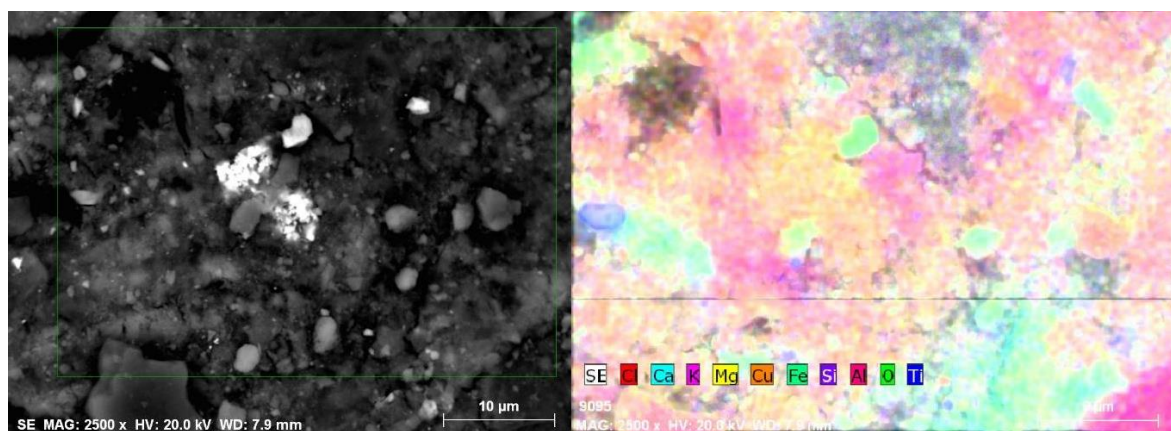


Figure 32: SEM-EDS backscattered electrons image of M20 and elemental mapping selected area

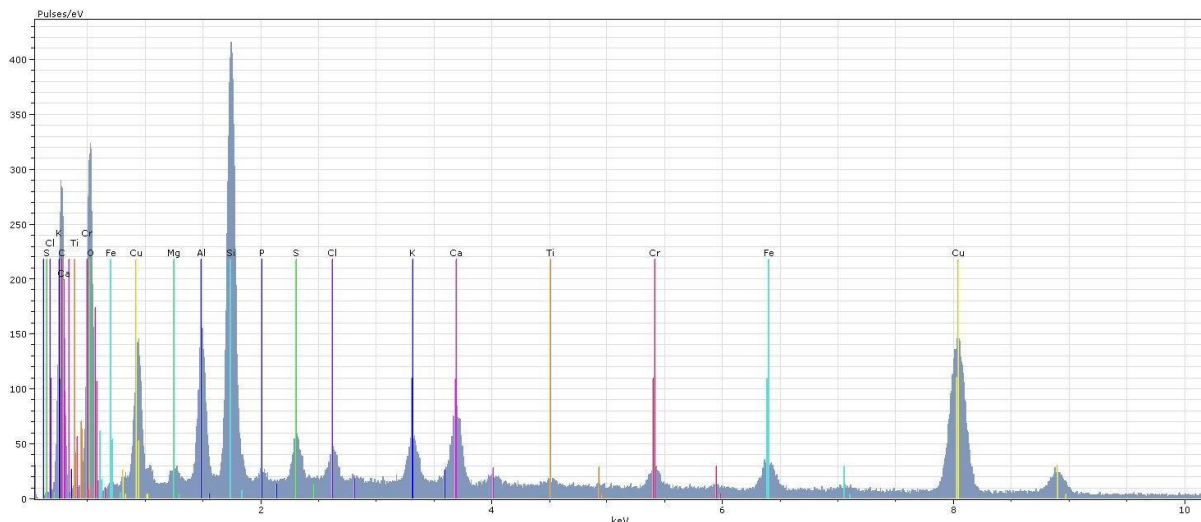


Figure 33: EDS spectrum of M20

Atacamite, cuprite, tenorite, calcite, quartz, aragonite, illite can be confirmed on the patina of M20 with the SEM-EDS results (Figure 33). The patina of the coin mainly consisted of soil derived minerals. The patina later on cleaned and following the cleaning of the patina surface, the elemental analysis showed that it was an arsenical bronze. Although On the other hand, both SEM-EDS and μ XRD were not capable to detect the As because of the thick patina layer.

Also M23 lead (Figure 34 and 35) has been detected which corresponds with μ XRD results. M23 was the only sample with Pb according to the μ XRD results (Figure 36). Later on it was found out that Pb was more common in the composition than initially thought belief. It was used as an alloying element to produce leaded-bronze coins in case of M23 and M26 according to XRF results. For the rest of the samples it was a trace element, which corresponds to the SEM-EDS and μ XRD results.

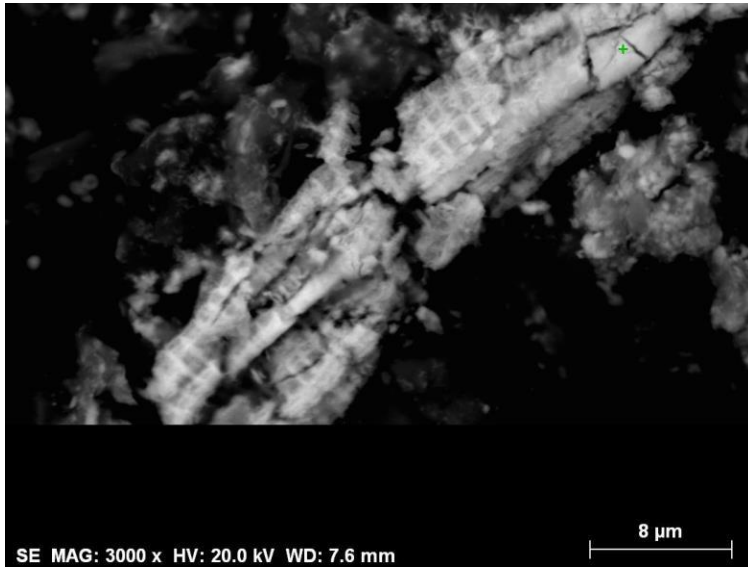


Figure 34: SEM-EDS backscattered electrons image of M23

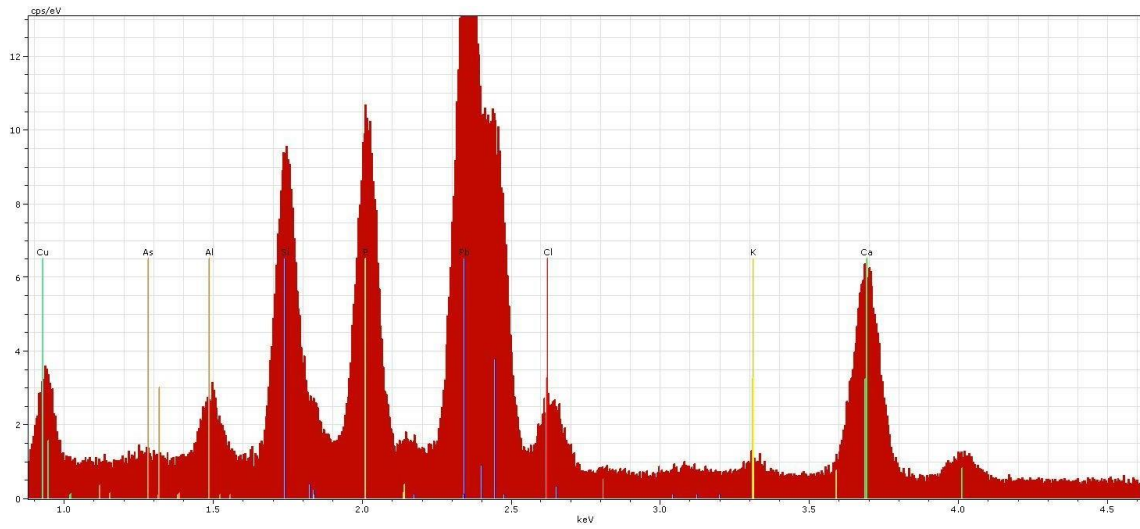


Figure 35: EDS spectrum of M23

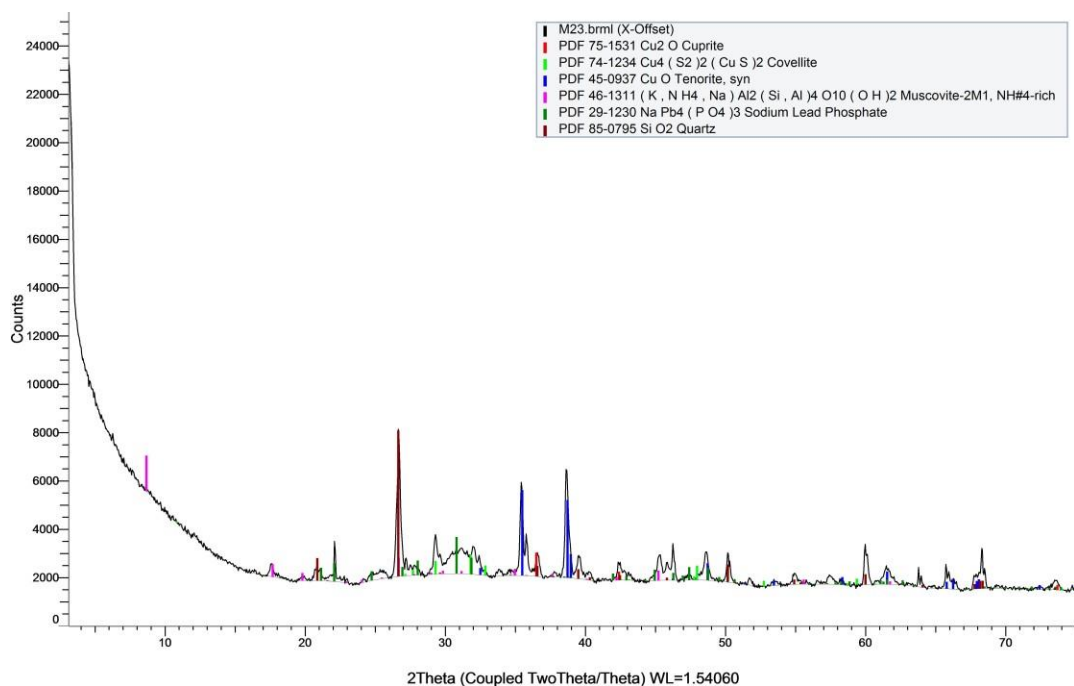


Figure 36: μ XRD spectrum of M23

3.3. MC SIMULATION

The experimental setup is composed of an X-ray tube under the operating conditions of 40 kV voltage and a of 12.5 μ A current equipped with a rhodium tube and silicon drift detector. Tube and detector can be positioned independently of each other allowing the geometry to be chosen according to the surface kind and the accessibility of the sample. The Monte Carlo code package, XRMC, needs several input-files that contain a description of the sample composition and the structures, the X-ray spectrum coming out from the X-ray tube, both in terms of energy as well as spatial distribution, and the detector description (size, structure and position).

After the elemental and mineralogical analysis of all the 37 coins, Monte Carlo simulation was applied to the XRF results. With the other techniques, SEM-EDS, μ XRD and XRF, we already gathered information about the elemental composition of the coins and also of the patina, both corrosion and soil related. For the simulation the main goal was to find out the composition and the patina thickness. The original and simulated spectra was superimposed on to each other using OriginPro. When two spectras match, it means that the simulated values are equal to the real values. In the case of our samples, we faced multiple difficulties and not having the numerical results was the main one. One simulation protocol takes 60-90 seconds to finish, which is not very long, but to have the best match, it takes a lot of iterations. Having 37 samples

with a very rough patina and a lack of experience with the simulation limited our success in the simulation.

Results from XRF were used for the simulation without prior interpretation. It creates the problem of not having enough elemental information before the simulation. If the results were interpreted before, it would be easier to create the data for the composition file. Since all the elements and their compositions were presented vaguely before the simulation, it took so much time to reach the original values. After having elemental match, described values in the quadric array file were changed. This file was for the thickness of the patina.

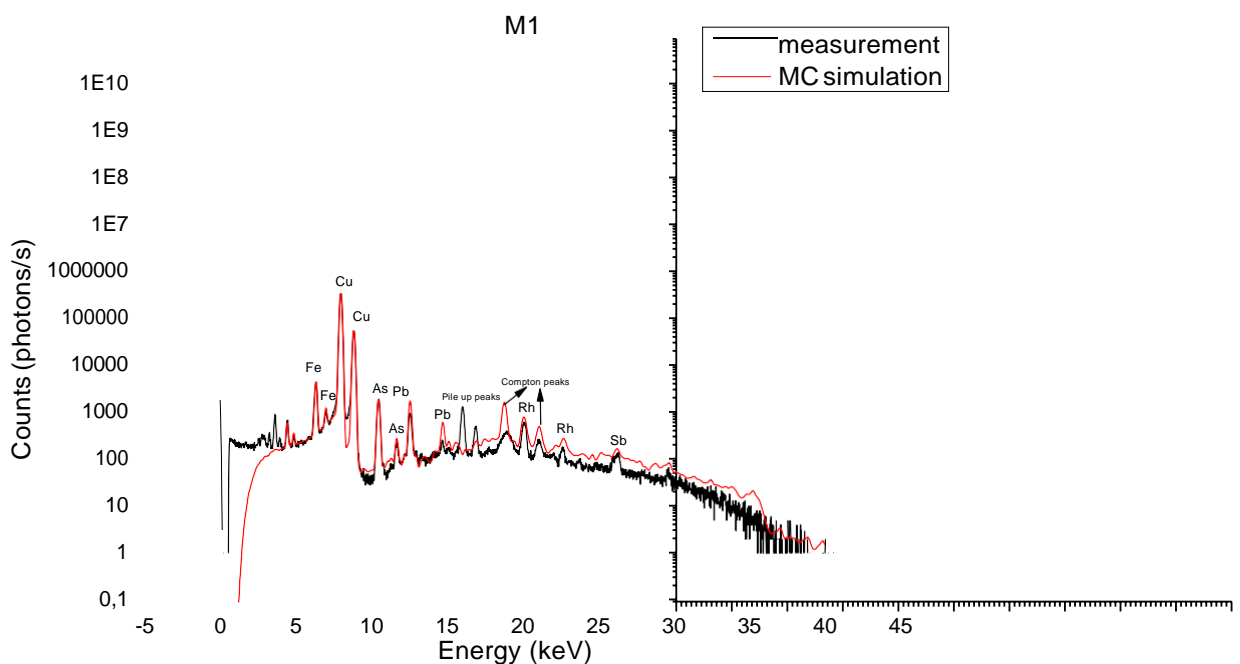


Figure 37: MC simulation and measured XRF spectra of M1

The unfinished results of M1 is presented above (Figure 37). Fe, Cu, As, Pb, Sn as well as Rh from the X-ray tube were found on the coin. Also copper pile-peaks and Compton peaks were detected. When two photons enter the detector at the same time, it results into pile-up or sum peaks. Both of the two photons will produce an electron cloud but they are counted as one large cloud. The sum of the two initial energies of the photos are the detected energy by the XRF. Pile-up peaks can be confused with other peaks, or can lead to wrong conclusions about the elements in the sample (Brouwer, 2003). As explained, pile-up peaks are mistakes, that is why they were not simulated, which is one of the pros of MC simulation. When incoming X-rays reflect from the sample instead of producing characteristic radiation, scattering happens. If

sample has light elements, it gives a high Compton scatter and vice versa (Brouwer, 2003). Compton peaks were not matched because of that reason. Since our main goal was to find the composition in the first place, only the elements from the coins were described and tried to be matched. While doing the simulation the presence of a rough patina, which creates the background on the surface, constrained us from achieving the best match. That was the main obstacle for the simulations. Even when the peak of the elements matched, the background did not match. Firstly, the compositions of the elements were tried to be matched and afterwards, the density and/or thickness values were changed to overcome the background problems. This problem occurred in all the coins.

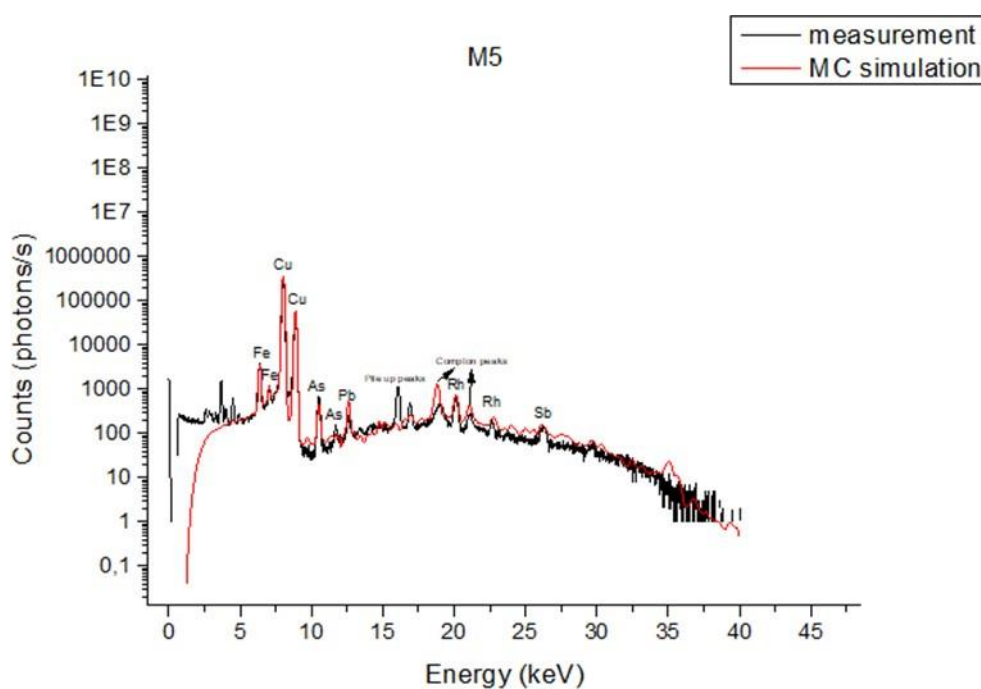


Figure 38: MC simulation and measured XRF spectra of M5

Coins have two patinas: corrosion, which is the first one on the metal surface and the patina covered with soil derived minerals. Only the corrosion layer was simulated as a “phase oxide” in the composition file along with the coin composition, which is the reason why the simulated spectra starts at a higher energy level than the original. To eliminate the soil crust and to assess the metallic elemental composition without cleaning the coin was the main goal of the study.

In the oxide phase of the input file, carbon, oxygen, copper, iron and lead were described. The input files we used for this work were altered from another study instead of creating new ones from scratch. Input files were created for bronze samples before. With the other analysis, it was

concluded that almost all the coins are made from pure copper, the “phase bronze” changed by us afterwards in the input file. For almost all the coins, “phase bronze” contains oxygen, titanium, iron, copper, antimony, lead and arsenic. Silver and zinc were found in a couple of samples. In that case these elements were added to the input file with expected concentrations and the simulation was re-run with the new elements.

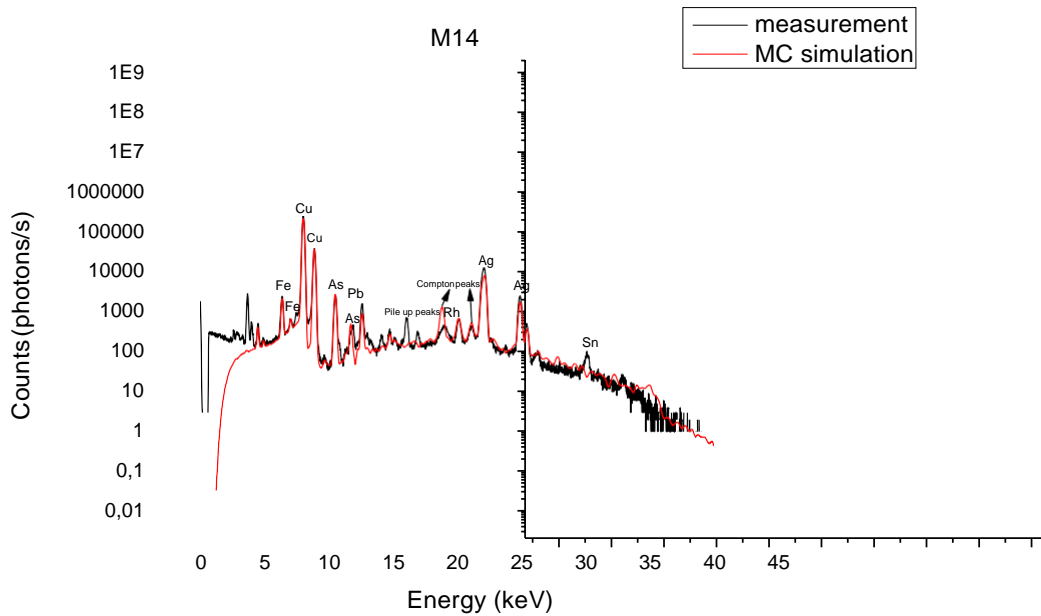


Figure 39: MC simulation and measured XRF spectra of M14

Silver can be seen on the M14 which the μ XRD couldn't detect (Figure 38). After MC simulations, 23 samples were selected to be partly cleaned for XRF and it was found out that for 4 samples Ag was the alloying element and for the others it was only a trace element. If we had the Ag-concentration of M14 from the simulation, we might had been able to compare the results and to maybe identify the chronology of the samples because only the early period portuguese coins has Ag as an alloying element.

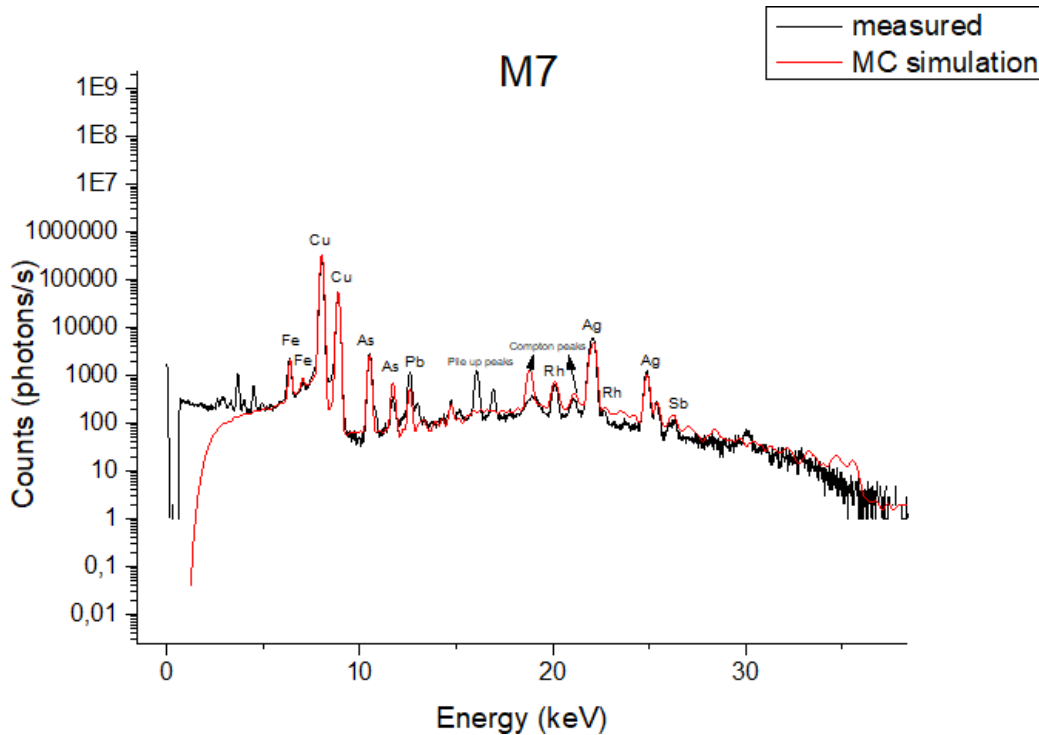


Figure 40: MC simulation and measured XRF spectra of M7

M7 was one of the cleaned samples and from the XRF results it can be said that M7 has billion alloy composition and MC simulation also showed the same but still the background is a problem for the spectrum (Figure 40). As and Pb peaks are not matching with the measured spectra, while Fe, Cu and Ag is showing a better match.

The large gap between the two copper $K\alpha$ and $K\beta$ lines, is observed on all the coin MC spectras. The reason for that is not totally clear. Any changes in the composition or quadric array file did not solve the problem. Simulated experimental conditions might be responsible for the problem but exactly which changes should be done was not known.

A spectrum of As K, overlapped with a Pb L line spectrum on both the original as well as the simulated spectrum. To overcome this problem, after matching the $K\alpha$ lines of both the elements, secondary peaks were checked and the concentration changes were made according to them. Finally, the simulation was run again. These steps were repeated until the best match for both the elements was achieved.

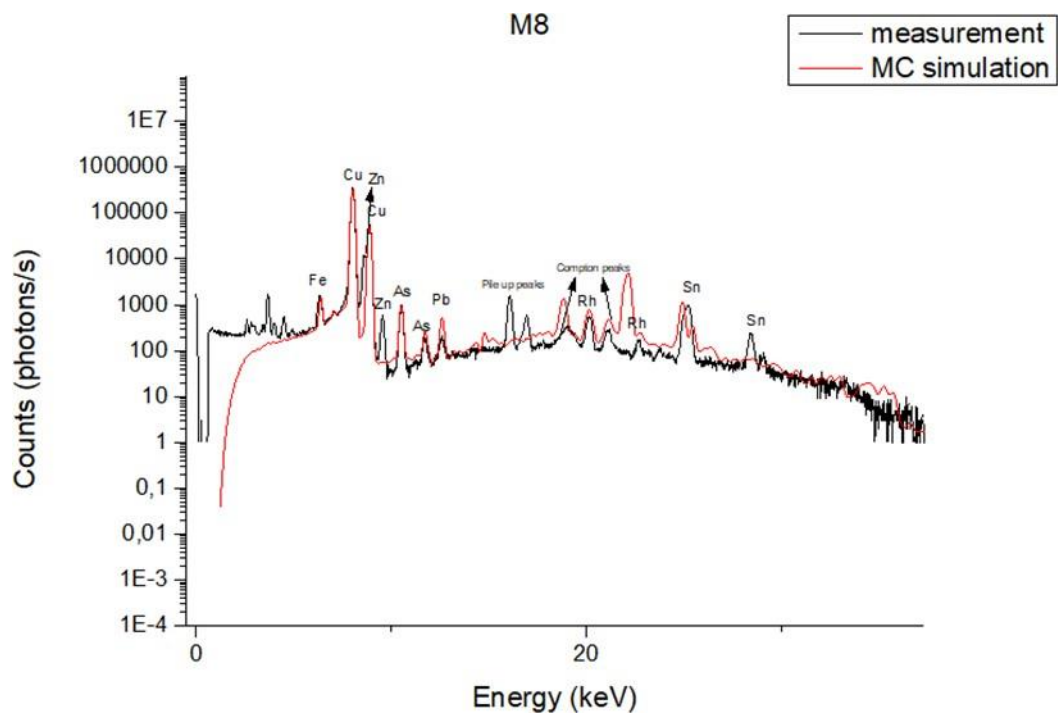


Figure 41: MC simulation and measured XRF spectra of M8

The unfinished simulation of M8 is presented above as Figure 41. μ XRD found copper and zinc in the coin and after cleaning XRF analysis also gave the same results with Sn, which shows that M8 is an alloy and not a pure copper coin. Using the same composition file was the problem in the case of M8. Later on Zn was added to the input file and the simulation was run again. This is an example of how important it is to have accurate input files to create the simulated real spectra.

Without prior knowledge it is very problematic to perform the simulation.

3.4. EDXRF

In this study 23 selected coin samples from Lagro das Olerias were examined. The elemental composition of alloying and trace elements were determined by XRF. Bruker Tracer III-SD has a spot size of approximately 7 mm². The samples were cleaned to have an area with those dimensions, which allows us to determine the exact composition of the coins without patina restrictions. The elemental composition of the samples are given in percentages. For all of the samples, the total of the elements does not sum up to 100 percent. Main reason is due to the highly oxidised condition of the coins. In some samples the sum is over 100 percent, due to experimental errors.

Table 7 List of elemental concentrations of coins

	<i>Cu</i> (%)	<i>Ag</i> (%)	<i>Fe</i> (%)	<i>Pb</i> (%)	<i>Zn</i> (%)	<i>As</i> (%)	<i>Sb</i> (%)	<i>Sn</i> (%)
<i>M9(1143-1383)</i>	97.420	1.763	0.311	0.404		0.184	0.452	0.187
<i>M11(1143-1383)</i>	92.591	6.300	0.126	0.331		0.158	0.045	0.449
<i>M7(1223-1248)</i>	92.058	5.594	0.150	0.891	0.080	0.488	0.183	0.556
<i>M28(1248-1383)</i>	98.270	0.059	0.286	0.085	0.104	0.525	0.361	0.310
<i>M27(1385-1433)</i>	96.067	1.695	0.215	0.126	0.118	0.413	0.631	0.736
<i>M22(1433-1438)</i>	97.501	0.042	0.364	0.629	0.131	0.112	0.649	0.572
<i>M37(1438-1481)</i>	98.508	0.070	0.161	0.527	0.152	0.080	0.256	0.245
<i>M1(1521-1557)</i>	97.567	0.034	0.320	0.892	0.150	0.495	0.303	0.239
<i>M24(1521-1557)</i>	98.258	0.041	0.183	0.868	0.139	0.150		0.299
<i>M3(1557-1579)</i>	97.910	0.030	0.012	1.135	0.097	0.203	0.351	0.261
<i>M4(1557-1579)</i>	98.677	0.019	0.105	0.460	0.114	0.142	0.278	0.204
<i>M5(1557-1579)</i>	98.555	0.038	0.282	0.210	0.119	0.111	0.379	0.305
<i>M19(1557-1579)</i>	98.338	0.033	0.177	0.306	0.142	0.108	0.480	0.416
<i>M17(1777-1786)</i>	98.894	0.079	0.086	0.442	0.163	0.317	0.019	0.936
<i>M30(1764)</i>	96.404	0.123	0.112	0.914	0.159	0.245	1.046	0.997
<i>M8(Republica)</i>	94.523	0.001	0.079	0.063	2.854	0.259		2.221
<i>M2</i>	98.717	0.024	0.151	0.332	0.142	0.116	0.297	0.221
<i>M16</i>	98.876	0.128	0.506	0.220	0.027	0.204	0.040	
<i>M18</i>	97.895	0.038	0.189	0.489	0.166	0.083	0.600	0.540
<i>M20</i>	95.094		0.352	0.120	0.048	4.385		
<i>M23</i>	84.252	0.054	0.376	6.600		0.117		8.539
<i>M26</i>	78.687	0.009	0.451	12.501	0.789		0.065	7.499
<i>M31</i>	98.409	0.055	0.078	0.290	0.140	0.087	0.509	0.433

In Table 7, detected elements in the coins were listed. Although most of the coins are pure copper, some other alloys were also observed. Chronologically the first alloy was billion (copper-silver) alloy. M9, M11, M7 and M27 have silver in the composition more than 1%. M8 is the newest coin of all and it has zinc and tin as alloying elements. Copper-tin alloy is called bronze and copper-zinc-tin is red brass. Likely the addition of two elements to make an alloy can be related to reach the colour wanted.

M23 and M26, which are not dated, are also not pure copper coins. Both coins are leaded-bronze. It is not possible to say that they are from the same period. Even though the alloying elements are same for both the coins, the concentrations are different.

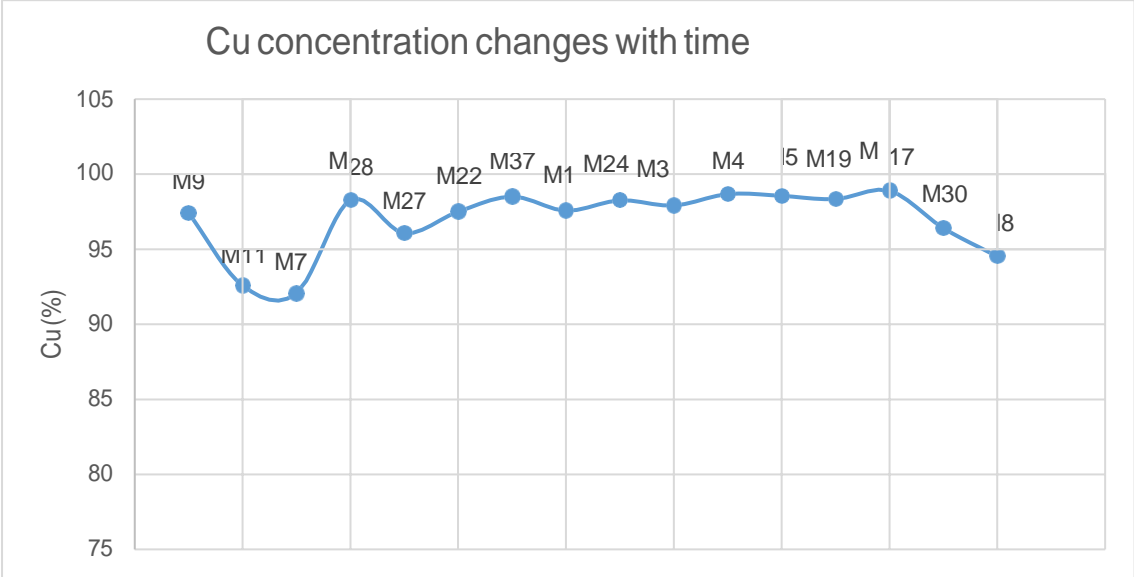


Figure 42: Cu concentration changes with time

Almost all of the coins were made out of pure copper and there are not big differences in copper percentages in the coins (Figure 42), except the alloyed ones. Some impurities and/or trace elements observed in the pure copper coins, which are related to copper ores that were being used. For the chronologically dated ones, historically between the billion and bronze alloys, there is no pattern to talk about gradual decrease or increase in the concentration of any element.

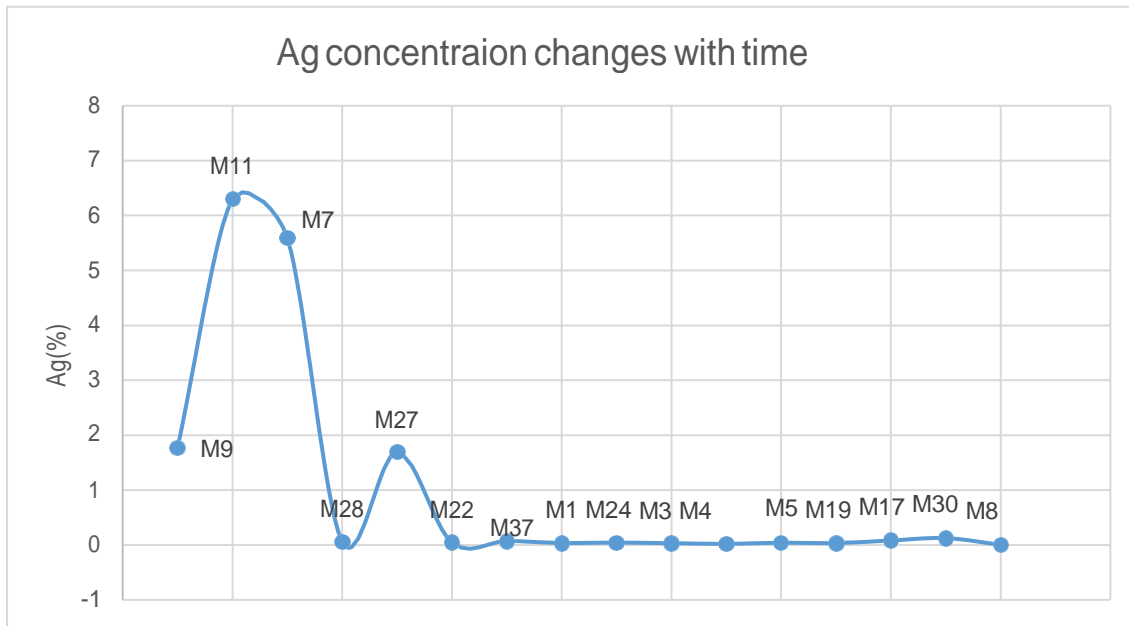


Figure 43: Ag concentration changes with time

In the early period Portuguese coins, silver was used as an alloying element (Figure 43). The time period for the dating of M9 and M11 is much larger as compared to others. From the silver concentration, it can be said that actually M7 and M11 might be from the same period before M9. There is a drastic change of silver in the coins with time, from alloying element to trace element, which can be easily related to economy. For the M11 and M7, silver is also found in the μ XRD, which was present in the uncleaned samples, in the form of chloargyrite (AgCl) in M11 and magnesium silver (Ag_3Mg) in M7.

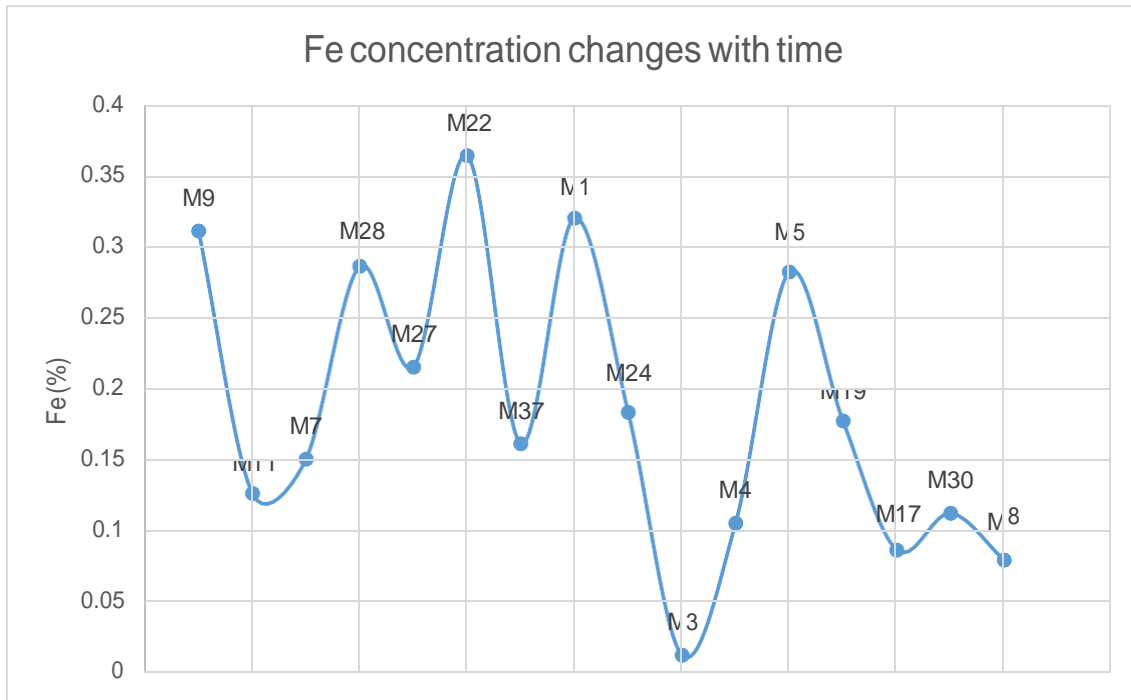


Figure 44: Fe concentration changes with time

Iron is the most important impurity in copper, because it forms segregates in the artefacts which corrodes away easily, since it has higher affinity for oxygen than copper (Özbal, 1985). For both dated and undated coins, iron concentrations are very low, which are trace levels. There are minor changes in the concentration of iron that might be explained by the usage of different copper ores (Figure 44).

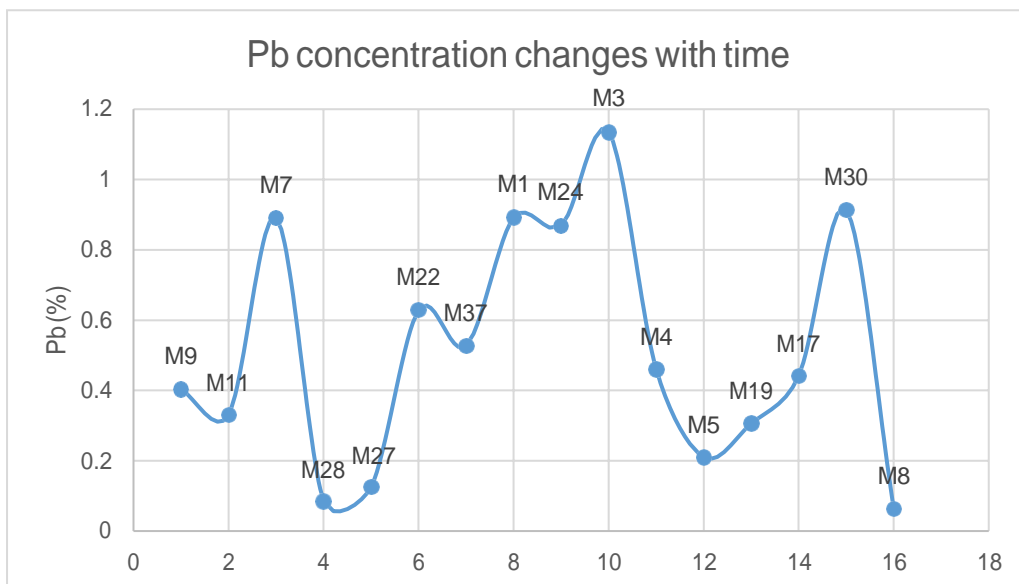


Figure 45: Pb concentration changes with time

Lead is almost totally insoluble in copper. During the Roman Period, it is well known that cheap lead was added to copper as high as 30% to increase volume. In such cases lead solidifies separately as lakes in the copper matrix and causes severe decrease in hardness and other mechanical properties of copper. Generally such mixtures cannot be hammered because they can easily crack. However, when lead is added into copper over 2%, it increases the fluidity and makes it much easier to handle during casting. Total 3 coins have lead concentrations over 1%: M3 (1.135%), M23 (6.6%) and M26 (12.501%). For the M23 and M26, lead is an alloying element in addition to tin to form leaded bronze. Lead is also found in the μ XRD analysis of the M23 and M26.

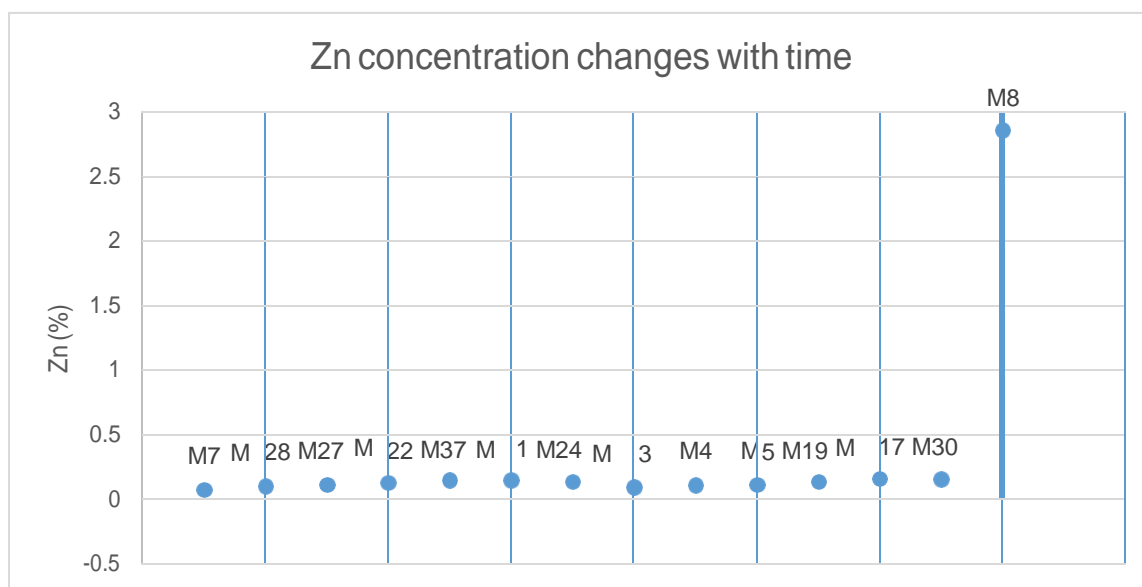


Figure 46: Zn concentration changes with time

The addition of zinc up to 30% makes a good alloy with copper which is known as brass. In the case of analysed coins, zinc is only observed in M8 more than trace amount as previously found in the μ XRD. Presence of zinc in copper as a trace element does not harm copper (Teylecote, 1962).

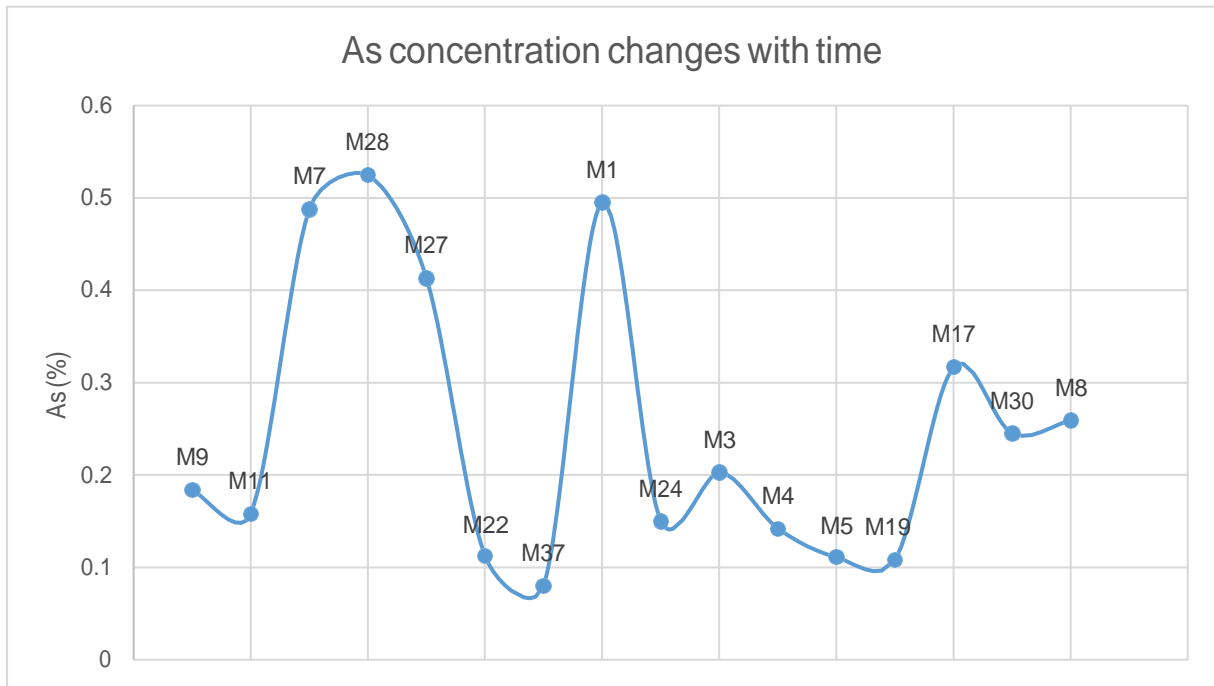


Figure 47: Zn concentration changes with time

The chronologically dated samples do not have high (more than 1%) concentration of arsenic and there is no pattern observed, which can confirm that the coins have As in trace amounts and it is not added intentionally. The sample with number M20 has arsenic concentrations 4.385%, which is the highest arsenic concentration in the group. If the arsenic concentration is higher than 1%, it is called “arsenical bronze”. It is interesting to see that arsenic is used as an alloying element, despite at quite low levels. Since arsenic as an alloying agent is highly toxic, especially when smelted, arsenic-rich copper might be the result of using polymetallic ores (Pernicka, 1995). High arsenic content might be the result of an arsenic enrichment of the coin’s surface

during the cooling down, and not necessarily mean the adding of a high amount it.

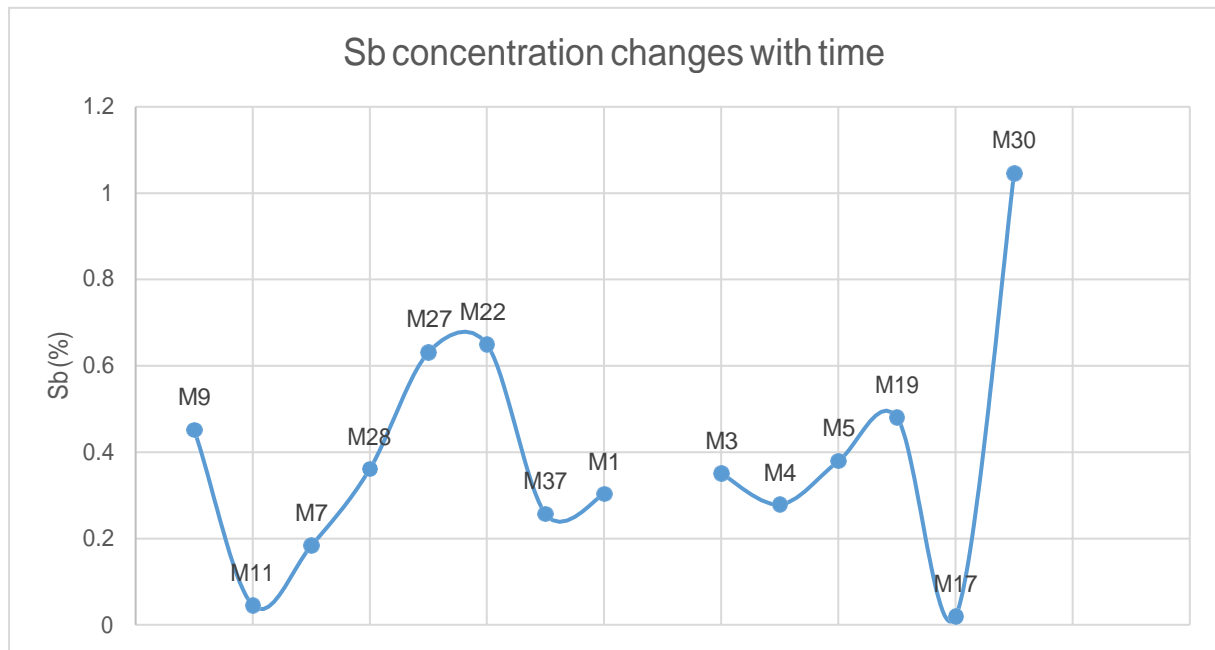


Figure 48: Sb concentration changes with time

In the copper based artefacts, antimony is one of the most important impurities. It accumulates in the metal during smelting. As a result, antimony has an important role to provide better information about the ore types and sources. Antimony mostly penetrates into copper as a result of smelting of antimony containing copper ores. Antimony is highly soluble in copper and is a volatile element, which is why its retention in copper depends on the smelting temperature and the reducing conditions of the furnace. Antimony as an impurity makes copper very hard and brittle (Teylecote, 1976).

There is only one sample with high antimony content, M30 (1.046%) which was considered to have antimony as compared to the other samples. It is highly probable that it was not an alloying element.

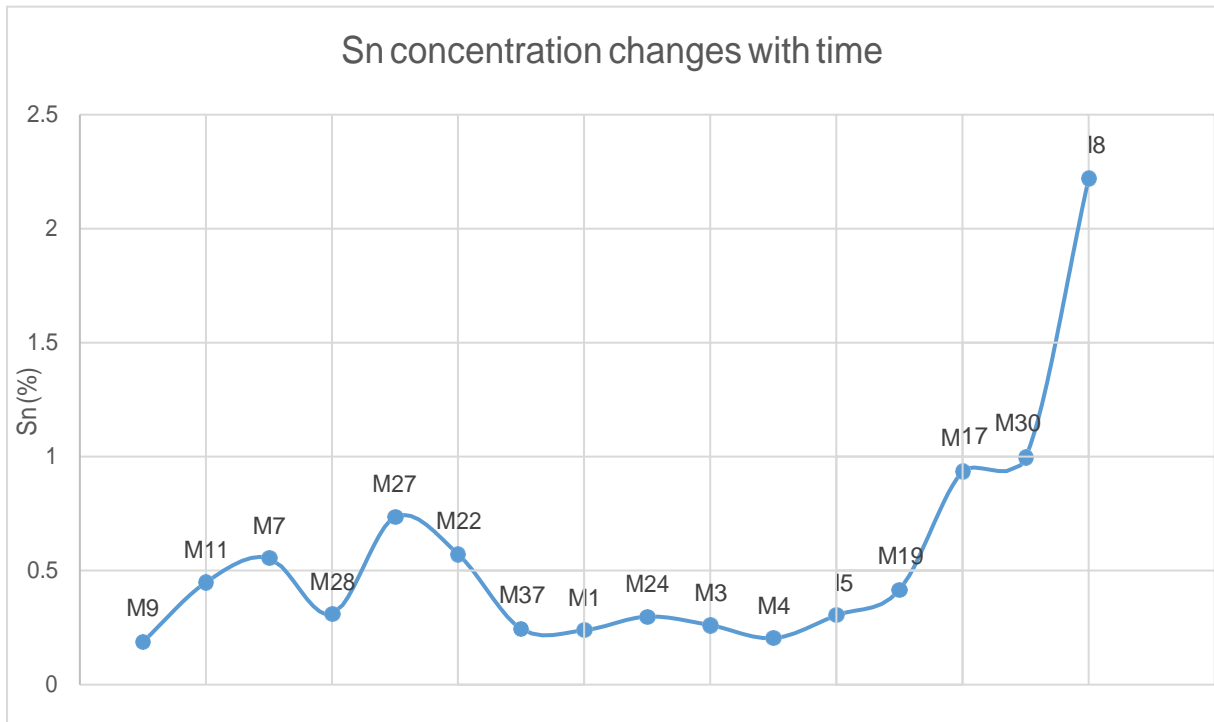


Figure 49: Sn concentration changes with time

Copper based artefacts that contain over 2% tin are considered to be an intentional alloy (Gomes et al., 2013). Higher than 2% tin was only observed in M8 (2.221%), M23 (8.539%) and M24 (7.499%).

All 23 coins are made of copper with the percentages changing from 98.876 to 78.687, average being 95.782%. Second important element is silver with an amount varying between 6.300% and 0.001%. Silver exists in all coins samples except M20. Another important element is arsenic with an amount varying between 0.087% and 4.385%, the average being 0.408%. Arsenic exists in all coin samples except M26. Lead and iron are present in all coin samples. Lead value is between 0.085% and 12.501% with the average being 1.253%, while iron percentage in coin samples varies from 0.012% to 0.506%, the average being 0.220%. In some coins, zinc is also present with a percentage of varying 0.027% to 2.584%, averaging at 0.291%. Antimony exists with an amount varying between 0.045% and 1.046%, with the mean at 0.365%. Tin, another important element in coin production was also found in amounts varying between 0.187% and 8.539%, at the mean of 1.254%. Copper is the main constituent with a varying proportion between 98.876% and 96.404 % and the mean at 97.952% for fifteen of the samples.

4. FINAL REMARKS AND FURTHER WORKS

In this study, SEM-EDS, μ XRD, EDXRF and Monte Carlo simulations were combined to obtain compositional data of the Portuguese copper coins. Since there were no cleaning treatment applied to samples, we faced some difficulties. The patina was very rough and uneven, covered with not only metal corrosion products also soil derived minerals, which made it hard to analyse the bulk and corrosion layer composition and thickness. Using only common methods (SEM-EDS, μ XRD, EDXRF) gave only limited results. To achieve the goal that was set for this study, a new method, Monte Carlo simulations were used. The EDXRF spectra modelled using C++ and run by XRMC. Origin, a computer program, used for graphing and data analysis of the results both from simulation and real. For the graphics, two data superimposed to each other and try to have the exact match between the real and simulation. In given time, our attempts did not fully succeed. Still it can be easily say that EDXRF/MC method is convenient method for metallic cultural heritage object.

The first method applied to coins was μ XRD, which allows examination of very small areas of a sample, focusing the incident beam on a certain spot (several micrometres) on a sample surface, providing the knowledge of crystalline structure of material. Choosing the spot for analysis was done very carefully to acquire the best and most accurate results. The cleanest section (section with the less patina) on the coin surface was found and after μ XRD performed. Since it was spot analysis, we only collected the results partly about the mineralogical composition of the coin. With the other methods (SEM-EDS and XRF), we gathered more information and/or confirmed the results of μ XRD.

Two different patina observed on all 37 coins: while first patina consist of metallic corrosion products of copper, second one has minerals from soil that they were stored. Having a soil patina on the surface was one of the problems that we encountered during our study because it was preventing us to reach the copper and/or alloy core and the corrosion layer while analysing samples. On the other hand, it is known that soil composition effects the corrosion process so if we had a detailed information about the soil, where coins stored, the problem of having a soil patina might have been overcome.

On the patina quartz is found on every sample. Calcium carbonate, calcite, is the second common soil mineral after quartz. 20 out of 37 coins have calcite on the patina. Dolomite and

ankerite, another carbonate with very similar composition to dolomite was also detected. From the mica group muscovite, biotite and illite were found on the corrosion patina infrequently. Another rare minerals that were on the patina are kaolinite, gypsum, gehlenite and montmorillonite. Cuprite and atacamite are the most common corrosion products on the surface. Cuprite is the first copper corrosion product after metal react with the gaseous environment and later on it acts as a chloride exchange layer for the copper surface and forms the atacamite/paratacamite. Tenorite, paratacamite, nantokite, malachite are other copper corrosion products that were presented in the patina. Copper sulphides, chalcocite, covellite and digenite and copper sulphate, connellite detected on the corrosion patina, which explained with the bacterial activities. Copper – zinc and corrosion products of silver and lead are also found. It can be concluded that these coins made from alloys not from pure copper, which only found in one sample. Iron oxides, from the soil or the copper were also found, because XRF results showed that Fe in the concentration is a trace element not belong original coin composition. Later on SEM-EDS method was used to compare the results.

After elemental and mineralogical analysis of all coins, Monte Carlo simulation was applied to the XRF results. The aim of the simulation was to find out the composition and patina thickness. When two spectras match, it means the simulated values are equal the real values. In the case of our samples, we faced multiple difficulties and not having the numerical results is the main one. One simulation takes 60-90 seconds to finish depending on the sample, which is a very short time, but to have the desired match, it needs lots of re-runs. Having 37 samples with a very rough patina and lack of experience with the simulation limited us to succeed in the simulation. The first problem we encountered was the patina, it was creating the background, because of the rough surface of it, on the spectra, which we couldn't find the parameters to solve it. That created the other problem: not having enough knowledge about the simulation to overcome the problems. If the elemental concentrations were known before, the simulation can be used as a double check method and also it saves time. In that case, it would have been easier to calculate/simulate the thickness. Overall it is an innovative method for archaeometry but it has limitations. Selection of the suitable sample may actually overcome most of the challenges we faced: sample with a flat surface and less patina.

Later on 23 selected coin samples from Largo das Olarias were partly cleaned and the elemental composition and trace elemental characteristics of the alloys were determined through XRF without patina restrictions. Except 8 of them, the rest of the coins are pure copper. First alloying

element was Ag, which found on samples M9, M11, M7 and M27. Samples M7 and M11 has the highest Ag concentration in the entire group. In other samples the Ag amounts drop drastically as low as trace levels. Another alloy consisting Cu-Sn-Zn, which is closer to modern day red brass/gunmetal alloy, is M8. Other bronze samples with differing combination of Cu and other alloying elements are M20, M23 and M26. Of these, sample M20 is arsenical and the samples M23 and M26 are leaded bronze. Almost all of the coins analysed were made of pure copper and the Cu values in the group did not exhibit significant amount of variation. Some impurities and/or trace elements observed on the pure copper coins can be linked to the original copper ores. The detected trace elements (or impurities) were Ag, Fe, Pb, Zn, As, Sb and Sn (except Ag, Pb, Sn and Zn being an alloying element rarely). It wasn't possible to have a chronological pattern of the coins in the elemental level. There were not any gradual decrease or increase in the composition of the coins.

5. REFERENCES

Angelini E., Bianco P., Zucchi F., 1993. On the Corrosion of Bronze Objects of Archaeological Provenance, Progress in the Understanding and Prevention of Corrosion, Institute of Materials. 14–23

Aragão A. T., (1877). *“Descrição Geral e Histórica das moedas cunhadas em nome dos Reis, Regentes e Governadores de Portugal”*, Tomo I, Imprensa Nacional, Lisboa.

Atlan, S., Baydur N., 1984. Grek ve Roma Sikkeleri, Arkeoloji Ve Sanat Yayınları, İstanbul.

Bardal E., 2004. Corrosion and Protection, Springer-Verlag, London. 24

Beck L., Alloin E., Berthier C., Reveillon S., Costa V., 2008. Silver surface enrichment controlled by simultaneous RBS for reliable PIXE analysis of ancient coins, Nuclear Instruments and Methods in Physics Research B, 266. 2320-2324.

Beckhoff, B.; Kanngießer, B.; Langhoof, N.; Wedell, R.; Wolff, H. 2006. Handbook of Practical X-Ray Fluorescence Analysis. 1 ed. Springer, Berlin-London.

Bottaini C., Mirão J., Figueredo M., Candeias A., Brunetti A., Schiavon N., 2015. Energy dispersive X-ray fluorescence spectroscopy/Monte Carlo simulation approach for the non-destructive analysis of corrosion patina-bearing alloys in archaeological bronzes: the case of

the bowl from the Fareleira 3 site (Vidigueira, South Portugal). *Spectrochim Acta, Part B* 103-104:9–13.

Bottaini C., Brunetti A., Bordalo R., Valera A., Schiavon N., 2017. Non-destructive characterization of archeological Cu-based artifacts from the early metallurgy of southern Portugal. *Archaeological and Anthropological Sciences*.

Bottaini C., Brunetti A., Montero Ruiz I., Valera A., Candeias A., Mirao J., 2017. Use of Monte Carlo simulation as a tool for non-destructive ED-XRF analysis of archaeological copper-based artefacts from the Chalcolithic site of Perdigões, Southern Portugal. *Applied spectroscopy*

Bouwer P., 2006. *Theory of XRF : Getting Acquainted with the Principles*. PANalytical B.V., The Netherlands.

Brunetti A., Golosio B, Schoonjans T., Oliva P., 2015. Use of Monte Carlo simulations for cultural heritage X-ray fluorescence analysis, In *Spectrochimica Acta Part B: Atomic Spectroscopy*, Volume 108. 15-20

Caley E. A., 1964. *Analysis of Ancient Metals*. Pergamon, London. 36-57.

Couture-Rigert D. E., Sirois P. J., Moffatt E. A., 2012. An investigation into the cause of corrosion on indoor bronze sculpture, *Studies in Conservation* Vol. 57 , Iss. 3. 142-163.

Cramer S.D., Covino B. S., 2006. *ASM Handbook, Volume 13B: Corrosion: Materials*, ASM International, Ohio.

Cramer S.D., Covino B. S., 2006. *ASM Handbook, Volume 13C: Corrosion: Environments and Industries Materials*, ASM International, Ohio.

Cronyn J.M., Robinson W.S., 1990. *The Elements of Archaeological Conservation*, Routledge.

Cullity B. D., 1978. *Elements of X-ray Diffraction*, Addison-Wesley Publishing Company Inc, Massachusetts.

Dexter S.C., 2003. Microbiologically Influenced Corrosion, *Corrosion: Fundamentals, Testing, and Protection*, Vol 13A, ASM Handbook, ASM International, Ohio. 398–416

Duncan S.J., Ganiaris H., 1987. Some Sulphide Corrosion Products on Copper Alloys and Lead Alloys from London Waterfront Sites, *Recent Advances in the Conservation and Analysis of Artifacts*, Summer Schools Press. 109–118

- Echlin P., 2009. Handbook of sample preparation for scanning electron microscopy and X-ray microanalysis, New York
- Einzig P., 1966. Primitive Money. 2nd Edition. Blackie and Son Ltd., Bishopbriggs, Glasgow.
- Exner H.E., Weinbruch S., 2004. Scanning Electron Microscopy, Metallography and Microstructures, Vol 9, ASM Handbook, ASM International, Ohio.
- Fabrizi M., Ganiaris H., Tarling S., Scott D.A., 1989. The Occurrence of Sampleite, a Complex Copper Phosphate, as a Corrosion Product on Copper Alloy Objects from Memphis, Egypt, Stud. Conserv., Vol 34 (No. 1). 45–51
- Farquhar M. L., Vaughan D. J., Hughes C. R., Charnock J. M., England K. E. R., 1997. Experimental studies of the interaction of aqueous metal cations with mineral substrates: Lead, cadmium, and copper with perthitic feldspar, muscovite, and biotite, In Geochimica et Cosmochimica Acta, Volume 61, Issue 15. 3051-3064.
(<http://www.sciencedirect.com/science/article/pii/S0016703797001178>)
- Fjaestad M., Ulle'n I., Nord A.G., Tronner K., Borg G.C., and Sandberg M., 1998. Are Recently Excavated Bronze Artifacts More Deteriorated than Earlier Finds?, Metal 98, W. Mourey and L. Robbiola, Ed., James & James Science Publishers. 71–79.
- Florian M., Florian L.E., 1987. The Underwater Environment, Conservation of Marine Archaeological Objects, C. Pearson, Ed., Butterworths. 1–20
- Frost, R. L., Williams, P. A., Martens, W. and Klopogge, J. T., 2003. Raman spectroscopy of the polyanionic copper(II) minerals buttgenbachite and connellite: implications for studies of ancient copper objects and bronzes. J. Raman Spectrosc., 33: 752–757.
- Fultz B., Howe J. M., 2007. Transmission Electron Microscopy and Diffractometry of Materials. (Third Edition). Springer , Heidelberg.
- Garrels R.M., Christ C.L., 1965. Solutions, Minerals, and Equilibria, Harper & Row.
- Gettens R.J., 1970. Patina: Noble and Vile, Art and Technology: A Symposium on Classical Bronzes, S. Doeringer et al., Ed., MIT Press. 57–72
- Ghoniem M., 2011. The characterization of a corroded Egyptian bronze statue and a study of the degradation phenomena. International Journal of Conservation Science Volume 2, Issue 2.

Goldstein, J., Newbury, D.E., Joy, D.C., Lyman, C.E., Echlin, P., Lifshin, E., Sawyer, L., Michael, J.R., 2003. Scanning Electron Microscopy and X-Ray Microanalysis, Springer US

Golosio B., Schoonjans T., Brunetti A., Masala G.L., Oliva P., 2017. XRMC: The definitive manual, Version 6.6.0, Università degli Studi di Sassari, Italy.

Gomes, S., Figueiredo, E., Araújo, M., Lopes, F., Senna-Martinez, J. C., (2013). Isotopic lead characterization of archaeological bronzes from fraga dos corvos (n Portugal). Internatinal Journal of Conservation Science. 4. 661.

Grobner P.J., Clark C.C., Andreae P.V., Sylvester W.R., 1980. Steamside Oxidation and Exfoliation of Cr-Mo Superheater and Reheater Steels. National Association of Corrosion Engineers.

Hamann, C. H., Hamnett, A., & Vielstich, W. (2007). Electrochemistry (2., completely rev. and updated ed).

Harris J.O., Eyre D., 1994. Soil in the Corrosion Process, Corrosion, Vol 1, 3rd ed., L.L. Shreir et al., Ed., Butterworth-Heinemann. 273–286

Heredotus. Histories I. YKY, İstanbul. 94.

Jambor J.L., Dutrizac J.E., Roberts A.C., Grice J.D., and Szymanski J.T., 1996. Clinoatacamite, a New Polymorph of $\text{Cu}_2(\text{OH})_3\text{Cl}$, and its Relationship to Paratacamite and “Anarakite,” Can. Mineralog., Vol 3472.

Jones, D.A., 2004. Principles and Prevention of Corrosion, 2nd edition, Prentice Hall. 40-350

Kaelble E. F., 1967. Handbook of X-Rays, McGraw-Hill Book Company, New York.

Kalos M.H., Whitlock P.A., 2008. Monte Carlo Methods. Second Edition. WILEY-VCH Verlag GmbH & Co. KGaA, Weinheim.

Keeley, H.C.M., 1981. Recent work using soil phosphorus analysis in archaeological propection. Revue d'Archéométrie Année Volume 5 Numéro 1 pp. 89-95.

Klug H. P., Alexander L. E., 1974. X-ray Diffraction Procedures, John Wily & Sons, New York.

MacLeod I.D., 1991. Identification of Corrosion Products on Non-Ferrous Metal Artifacts Recovered from Shipwrecks, Stud. Conserv., Vol 36 (No. 4). 222–234

Magro, F. A. C. (1986). “*Ceitis*”, Sintra: Instituto de Sintra.

Manso M., Schiavon N., Queralt I., Arruda A. M., Sampaio J. M., Brunetti A., 2015. Alloy characterization of a 7th century BC archeological bronze vase—overcoming patina constraints using Monte Carlo simulations. *Spectrochim Acta, Part B* 107: 93–96

Marques, M., 1982. *Introdução à Numismática*. D. Quixote, Lisboa.

Microbial Corrosion, Proceedings of the Conference, National Physical Laboratory, The Metals Society, 1983

Millman, E., 2015. The Importance of the Lydian Stater as the World's First Coin. *Ancient History Encyclopedia*. Retrieved from <https://www.ancient.eu/article/797/>

Moioli, P. and Seccaroni, C. (2000), Analysis of art objects using a portable x-ray fluorescence spectrometer. *X-Ray Spectrom.*, 29: 48–52.

Morrisson C., 2002. *Antik Sikkeler Bilimi Nümismatik Genel Bir Bakış*, 1st edition, Arkeoloji Ve Sanat Yayınları, İstanbul. 10-141.

Nienhuis J., Robbiola L., Giuliani R., Joosten I., Huisman H., Os B. v., Sietsma J., 2016. Curly Malachite On Archaeological Bronze: A Systematic Study Of The Shape And Phenomenological Approach Of Its Formation Mechanism.

North N.A., MacLeod I.D., 1987. Corrosion of Metals, Conservation of Marine Archaeological Objects, C. Pearson, Ed., Butterworths., 68–98.

Organ R.M., 1970. The Conservation of Bronze Objects, Art and Technology: A Symposium on Classical Bronzes, S. Doeringer et al., Ed., MIT Press. 73–84

Özbal, H. 1985. “Değirmentepe Metal-Cüruf ve Filiz Analizleri”.Tübitak Arkeometri Ünitesi Bilimsel Toplantı Bildirileri VI, No.622.

Pauling L., 1964. *General Chemistry*, Dover Publication, New York. 338–360

Pernicka, E., 1995. “Gewinnung und Verbreitung der Metalle in prähistorischer Zeit.” *Jahrbuch des Römisch-Germanischen Zentralmuseums Mainz* 37. pp. 21-129.

Pourbaix M., 1966. *Atlas of Electrochemical Equilibria in Aqueous Solutions*, Pergamon Press. 223

- Protopopoff E., Marcus P., 2003. Potential versus pH (Pourbaix) Diagrams, *Corrosion: Fundamentals, Testing, and Protection*, Vol 13A, ASM Handbook, ASM International, Ohio. 17–30
- Raiswell R., 2001. Defining the Burial Environment, *Handbook of Archaeological Sciences*, D.R. Brothwell and A.M. Pollard, Ed., John Wiley & Sons. 595–604
- Rowlands J.C., 1994. Sea Water, *Corrosion*, Vol 1, 3rd ed., L.L. Shreir et al., Ed., Butterworth-Heinemann. 260–272
- Schiavon N., De Palmas A., Bulla C., Piga G., Brunetti A., 2016. An energydispersive X-ray fluorescence spectrometry and Monte Carlo simulation study of Iron-Age Nuragic small bronzes (Navicelle) from Sardinia, Italy. *Spectrochim Acta, Part B* 123:42–46.
- Scott D.A., 1990. Bronze Disease: A Review of Some Chemical Problems and the Role of Relative Humidity, *J. Am. Inst. Conserv.*, Vol 29 (No. 2). 193–206
- Scott D.A., 2002. *Copper and Bronze in Art: Corrosion, Colorants, Conservation*, Getty Publications.
- Schweitzer P. A., 2009. *Fundamentals of Corrosion: Mechanisms, Causes, and Preventative Methods*, CRC Press, USA.
- Schweizer F., 1994. Bronze Objects from Lake Sites: From Patina to “Biography,” *Ancient and Historic Metals, Conservation and Scientific Research*, D.A. Scott et al., Ed., Getty Conservation Institute., 33–50
- Selwyn, L. (2004). *Metals and corrosion: a handbook for the conservation professional*. Ottawa, Ont: Canadian Conservation Institute.
- Tekin, O., 2000. *Eski Çağda Para Antik Nümismatiğe Giriş*, 4th edition, Eskiçağ Bilimleri Enstitüsü Yayınları, İstanbul.
- Trigueiros A.M., Friedberg A. L., 1995. Prince Henry and the Treaty of Tordesilhas. *The Numismatic*, Volume 108, Number 1, 48.
- Turgoose S., 1993. Structure, Composition and Deterioration of Unearthed Iron Objects, *Current Problems in the Conservation of Metal Antiquities*, A. Aoki, Ed., Tokyo National Research Institute of Cultural Properties. 35–52

- Tylecote, R.F., 1962. *Metallurgy in Archaeology*, Edward Arnold Ltd., London.
- Tylecote, R.F., 1976. *A History of Metallurgy*, The Metals Society, London
- Tylecote R.F., 1979. The Effect of Soil Conditions on the Long-Term Corrosion of Buried Tin-Bronzes and Copper, *J. Archaeolog. Sci.*, Vol 6 (No. 4). 345–368
- Walker, R. 1980. Corrosion and preservation of bronze artefacts. *Journal of Chemical Education* 4, 277-280
- Wilmott M.J., Jack T.R., 2000. Corrosion by Soils, *Uhlig's Corrosion Handbook*, 2nd ed., R.W. Revie, Ed., John Wiley & Sons., Massachusetts. 329–348.
- Dong G. J., Ford T., Mitchell R., 2011. *Uhlig's Corrosion Handbook*, Third Edition. John Wiley & Sons., Massachusetts. 338
- Woods T.L., Garrels R.M., 1986. Use of Oxidized Copper Minerals as Environmental Indicators, *Appl. Geochem.*, Vol 1 (No. 2). 181–187
- <https://www.google.com/maps/place/Largo+das+Olarias,+Lisboa/@38.716697,9.1356713,17z/data=!3m1!4b1!4m5!3m4!1s0xd1933888d057467:0x5371a10b412a71ec!8m2!3d38.7169544!4d-9.1333144>. Last Access: 17/ 09/ 2017.
- <https://upload.wikimedia.org/wikipedia/commons/c/c4/MicroscopesOverview.jpg>. Last Access: 25 / 08/ 2017.
- <http://pubs.usgs.gov/of/2001/of01-041/html/docs/images/xrdtube.jpg>. Last Access: 25 / 08/ 2017.
- http://science.duel.life/images/stories/virtuemart/product/Hitachi_S-3700N_SEM.jpg. . Last Access: 24 / 08/ 2017.
- Catalog of Portuguese coins in escudo and Euro.
<https://www.moedanutismatica.com/coins/portugal.html> (accessed 13 September 2017).
- <http://www.capcoat.be/sites/default/files/images/AES-pear.jpg>. Last Access: 25 / 08/ 2017.
- [https://www.azom.com/images/Article_Images/ImageForArticle_4722\(2\).jpg](https://www.azom.com/images/Article_Images/ImageForArticle_4722(2).jpg) . Last Access: 28/ 08/ 2017.
- <http://www-archive.mse.iastate.edu/microscopy/home.html> Last Access: 25/ 08/ 2017.

<http://www.minerals.net/mineral/quartz.aspx>. Last Access: 15/ 09/ 2017.

<https://fiskalloy.wpengine.com/wp-content/uploads/2012/03/C194-Copper-Fisk-Alloy.pdf>.

Last Access: 15/ 09/ 2017.

<https://qph.ec.quoracdn.net/main-qimg-25f0430082794993d29afe7bffa9b5d0>. Last Access:

17/ 09/ 2017.

ANNEX

WORKING PRINCIPLES OF APPLIED ANALYTICAL TECHNIQUES

X – Rays and Types

X-Rays were first observed and documented by German physicist W. K. Roentgen in 1895 and were so named because of their unknown nature at the time. In 1912, Max von Laue had proved the wave nature of x-rays by using a crystal as diffraction gratin and established the phenomenon of x-ray diffraction by crystals. X-rays are high energy electromagnetic radiation having exactly the same nature as light. The wavelengths of the x-rays used in diffraction lies between 0.5-2.5 angstrom (0.05-0.25 nm) whereas, the wavelength of visible light is approximately 600 nm. X-ray spectra can be classified as into two types; the continuous and characteristic spectrum.

Continuous spectrum is produced by the rapid deceleration of the electrons after series of collisions with the target's atoms. The energy which is lost by collisions is converted into the photon energy and a continuous x-ray spectrum (also known as white spectrum or heterochromatic spectrum) consist of a range of wavelengths is obtained. If the voltage applied to an x – ray tube is raised over a certain critical value which is characteristic for the target metal, an orbital electron is dislodged from the certain energy level according to critical voltage. The vacancy of the orbital electron is filled by an electron from a higher energy level. As the filling electron moves down to fill the vacancy, it gives up energy emitted in the form of an x-ray photon, which is called characteristic spectrum (Cullity, 1978).

X – Ray Tube

X – Ray tubes are evacuated and sealed off devices which are used to obtain high-intensity x rays. X-ray tubes have vacuum envelopes that are made of glass or ceramics. In the filament tubes, tungsten filament is used as electron source (cathode) and metals like Cu, Co, W metals are used as target metal (anode). Moreover, since significant part of the kinetic energy of accelerated electrons is converted to heat as a result of collisions of electrons with target metal, so that water-cooling system is used in the tubes in order to prevent melting of target metal. After heating of tungsten filament (cathode) with 10 – 40 μ A, electrons are directly accelerated

toward the target metal (anode) with the help of high potential difference (30 – 60 kV) between anode and cathode. When the high velocity electrons hit the water-cooled anode, the x-rays are emitted in all directions from a specific target called as focal spot. The x-rays escape from beryllium windows are focused on the sample for characterization process. A schematic view of the x-ray tube is shown at Figure 42.

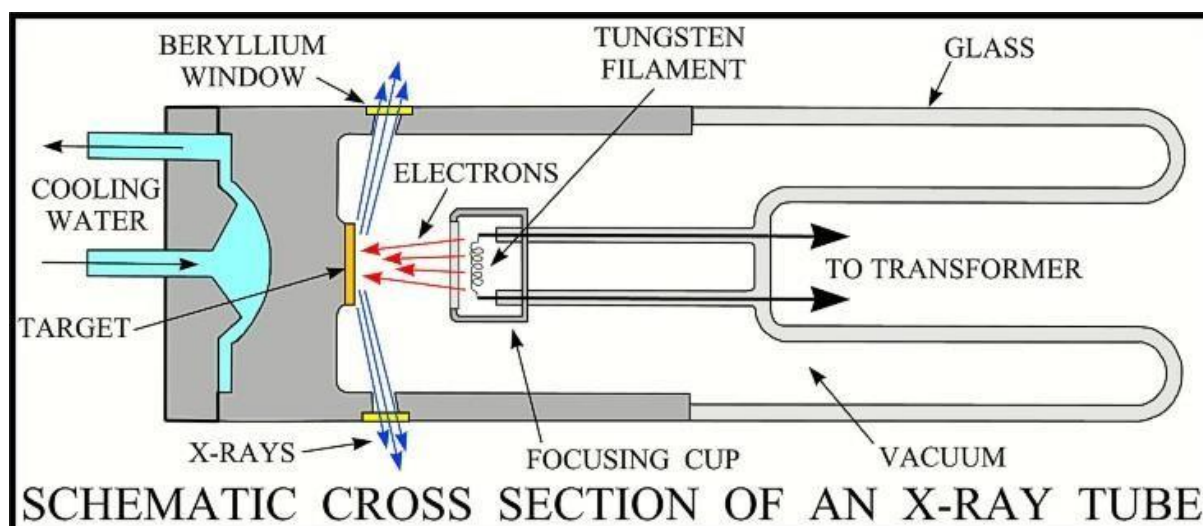


Figure 1: Filament X – Rays Tube (<http://pubs.usgs.gov/of/2001/of01-041/htmldocs/images/xrdtube.jpg>)

1. X-RAY FLUORESCENCE ANALYSIS

In XRF spectrometry, the material being examined is irradiated with X-rays, and as a result the atoms of each element emit a characteristic radiation of a particular wavelength. The emitted radiations are then separated by a diffraction crystal and can be detected and measured either by a photographic plate or by a Geiger counter. The technique is very similar to that of emission spectrometry. In XRF spectrometry there is no need to remove a sample from the sample holder, the results obtained will be an analysis of the surface only (Beckhoff 2006).

There are two types of XRF Spectrometer, one is energy dispersive (EDXRF), the other is wavelength dispersive (WDXRF). The EDXRF is more common than the WDXRF.

XRF spectrometry is a widely used technique for the analysis of archaeological artefacts, since it is relatively rapid, cheap, sensitive, and specific. The technique most commonly used involves the exposure of unprepared or minimally prepared surfaces to the X-ray radiation and

method is non-destructive. However, major errors can be present in the results, if the surface of the area exposed to the beam of X-rays is insufficiently flat (Beckhoff 2006).

XRF analyses can detect elements having atomic number 15 even less with some particular detectors.

In the field of authenticity, the XRF spectroscopy is one of the main techniques to determine the elements including in the alloy of the object like coins whether it is fake or not.

An important improvement in the method was the possibility of using a portable X-ray spectrometer starting in 1964. In this way a large number of measurements can be collected for statistical processing, comparison, and characterization of differences in the same work (Moioli and Seccaroni 2000).

The advantages of the portable XRF is listed below.

- There is no need for sample preparation
- Measurement is simple and rapid
- Analytical results are taken immediately
- Analysis of many areas in a single object can be possible
- Simultaneous multi-element analysis can be possible
- Detection limits is low (50-10 ppm) high sensitivity (Beckhoff 2006).

On the other hand portable XRF has same limitations since XRF analysis limited to sample's surface which can lead the problem of not having representative composition of the original alloy.

The archaeological metal artefacts' surface usually covered by patina (impurity layer) and surface loss due to corrosion. In some Cu-based alloys, effect of corrosion can be even seen by naked eye.

Surface enrichment effects and heterogeneity of the sample cannot be detected with XRF. For example, to increase the value of the coin, it is plated with the more precious metal than the core of the coin both today and the past. Because of the limitation of the XRF, it is hard to detect the effects.

2. X-RAY DIFFRACTOMETER TECHNIQUE AND μ XRD

In x-ray diffraction technique, every single phase in the structure of the analysed materials is characterized according to angular positions (2θ) and relative intensities of the patterns in the

diffraction diagram. Each pattern within the diagram occurs as a result of diffraction of x-rays from a particular plane. In 1913, English physicists Sir W.H. Bragg and his son Sir W.L. Bragg explained the interferences between X-ray scattered from a crystal and derived an equation known as “Bragg’s Law”;

$$\lambda = 2d_{hkl} \sin\theta \quad (1)$$

where:

λ is the wavelength of the rays, d_{hkl} is the spacing between the atomic planes, θ is the angle between the incident rays and surface of the crystals. Bragg Equation is used for determining the direction of the diffraction from a particular plane. As it seen from the equation, if the wavelength of the incident X-ray is known, diffraction angle ($\sin\theta$) directly depends on the d-spacing between the crystal lattice planes. The space between the atomic planes (d_{hkl}) is determined by crystalline structure (Bravais Lattices) and crystalline size (lattice parameters) of the material. The factors affecting d-spacing such as thermal and mechanical stresses, solid solution formation, can influence the positions of diffraction lines. Atomic positions within the unit cell determine the intensities of diffraction lines. Consequently, the intensity of diffracted x-rays at specific angles (2θ) is recorded during the XRD analysis. Phase characterization is achieved by calculating the relative intensities and the d-spacings of the diffraction peaks according to data shown in XRD diagram (Cullity, 1978; Kaelble, 1974).

Phase analyses which are performed according to the above mentioned principles, require accurate determination of intensity and d-spacing values. During the phase analysing, inconsistency between recorded data and standards could be occurred due to the equipment related problems (incorrect slit and filter selection during diffractometer calibration etc.), diffractometer related problems (energy applied to tube, speed rate of the analysis etc.) and sample related problems (thermal and mechanical treatments applied to analysed sample, impurities or solid solution existence and preferred orientation etc.) (Klug and Alexander, 1974).

2.1. QUALITATIVE PHASE ANALYSIS WITH X - RAYS DIFFRACTION (XRD)

Phase analysis with x-ray diffraction technique is based on identifying the characteristic diffraction patterns of all crystalline materials exist in the sample structure. If the analysed sample is the mixture of different phases, distinctive diffraction patterns of the every single

phase in the mixture should be detected in the diffraction diagram. Therefore, these distinctive diffraction patterns are considered as the identities or finger prints of the crystalline phases.

Micro X-ray diffraction (μ XRD) allows examination of very small areas of a sample, focusing the incident beam on a certain spot (several micrometres) on a sample surface, providing the knowledge of crystalline structure of material. The conventional XRD instrument is more bulky and it has a high power requirements, while the intensity of a μ XRD beam can be reached in a lower power source (Klug and Alexander, 1974).

3. SCANNING ELECTRON MICROSCOPE

Microscope is used for imaging the samples that are too small to see with naked eye. There are 4 main groups of microscopes: optical, acoustical, scanning probe and electron microscopes.

Optical microscope uses visible light for imaging. It is a fast but resolution-limited method. Etching may be needed to identify the phases, observing grains or grain boundaries. Acoustical microscopes uses sound waves with high frequency. Since sound waves can be absorbed by the matter; internal structure, such as defects, of the solids can be analysed by those microscopes. In order to have atomic resolution, electrons are used since they can be controlled much easier than electromagnetic waves (lights, X-rays) under electric or magnetic fields (Exner and Weinbruch, 2004)

There are different kind of microscopes that uses electrons, some of them are Scanning Electron Microscope (SEM), Transmission Electron Microscope (TEM), and Scanning Tunneling Microscope (STM).

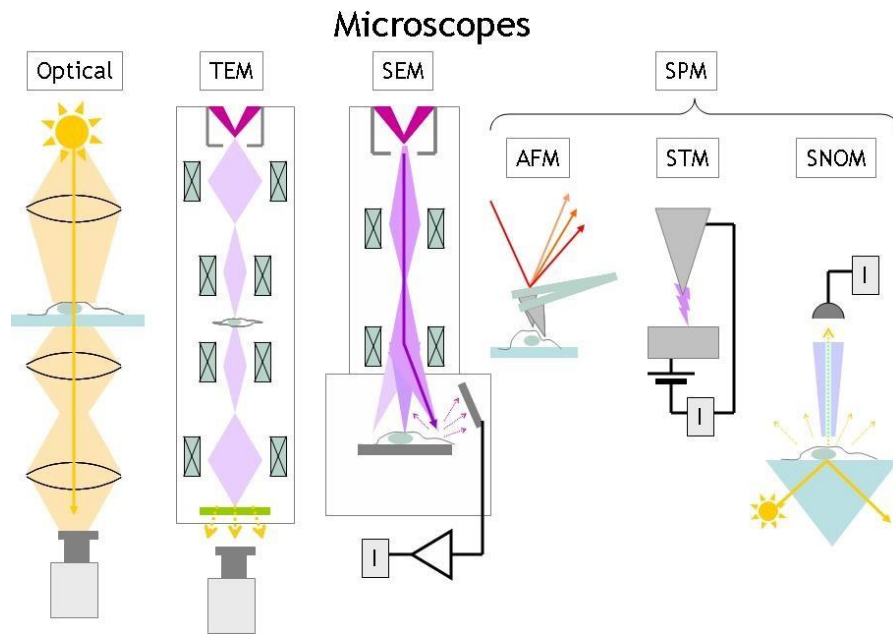


Figure 2: Different kinds of Microscopes

(<https://upload.wikimedia.org/wikipedia/commons/c/c4/MicroscopesOverview.jpg>)

Transmission Electron Microscopy (TEM) is a microscopy technique in which an ultra-thin (100 nm) specimen is exposed by an electron beam, interacting with the specimen as it passes through. An imaging system under the specimen gives images with very high resolution. TEM may also give electron diffraction patterns for crystallographic information of the specimen. However, sample preparation is very hard for TEM (Echlin, 2009).

Scanning Tunneling Microscope uses ultra-sharped tips where it is approached to the sample surface by piezoelectric materials. As the voltage applied between the tip and the specimen a tunneling current occurs. Tunneling current changes as the piezo material moves the tip. Changing current is transformed to an image with atomic resolution. STM technique needs a lot of time for analysing very narrow areas (Goldstein et al. 2003).

Scanning Electron Microscope (SEM) is a desktop-sized device that gives high resolution images of the surfaces, as well as the elemental analysis of any desired point.



Figure 3: A complete SEM system

(http://science.duel.life/images/stories/virtuemart/product/Hitachi_S-3700N_SEM.jpg.)

There are 4 main parts of SEM: Column, vacuum pump, sample stage, and the imaging system. On top of the column, a tungsten filament is used as the electron source. Since tungsten has high thermal emissivity, it emits electrons when heated. Electrons emitted by the filament is called primary electrons. In order to avoid the collision between electrons and air inside, column must be in vacuum around 10^{-4} Pa, where gauge and diffusion pumps may be used. Primary electrons beam is accelerated by anode under and focused by magnetic lenses located inside the walls of column. Scanning coils moves the beam to the each point on a desired area of the sample. When focused beam reaches the sample and the collision causes:

1. Auger electrons,
2. Secondary electrons (SE),
3. Backscattered electrons (BE),

4. X-rays, to emit (Goldstein et al. 2003).

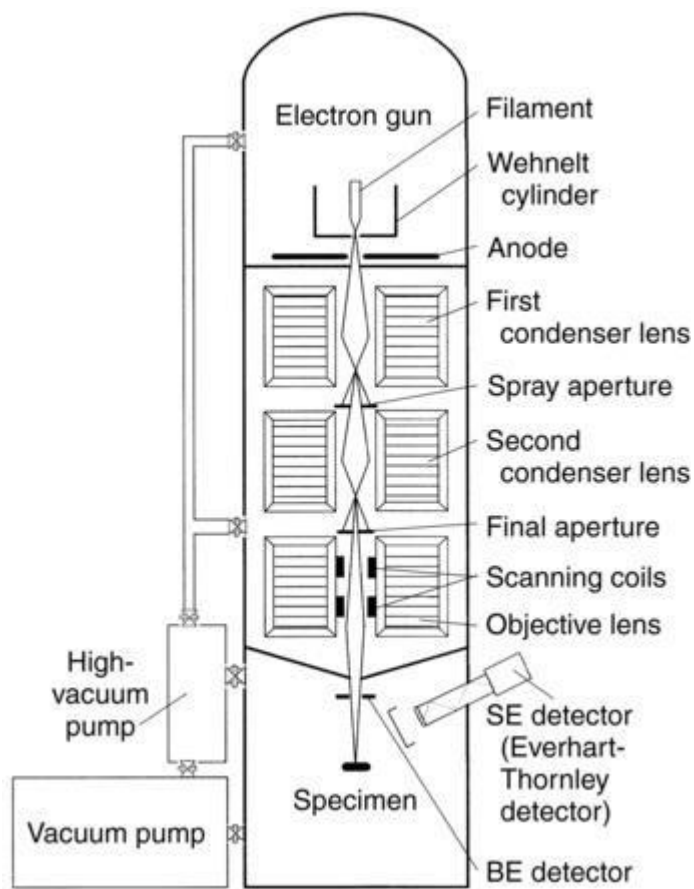


Figure 4: Inside column of a SEM for secondary and backscattered electron imaging. SE, secondary electron; BE, backscattered electron (<http://www-archive.mse.iastate.edu/microscopy/home.html>)

Auger electrons come directly from the surface atoms and give information about the top 3 monolayers of the surface. Auger electrons have different energy than any other electrons used in SEM and are only used in Auger Electron Microscopes which have their own Auger detector.

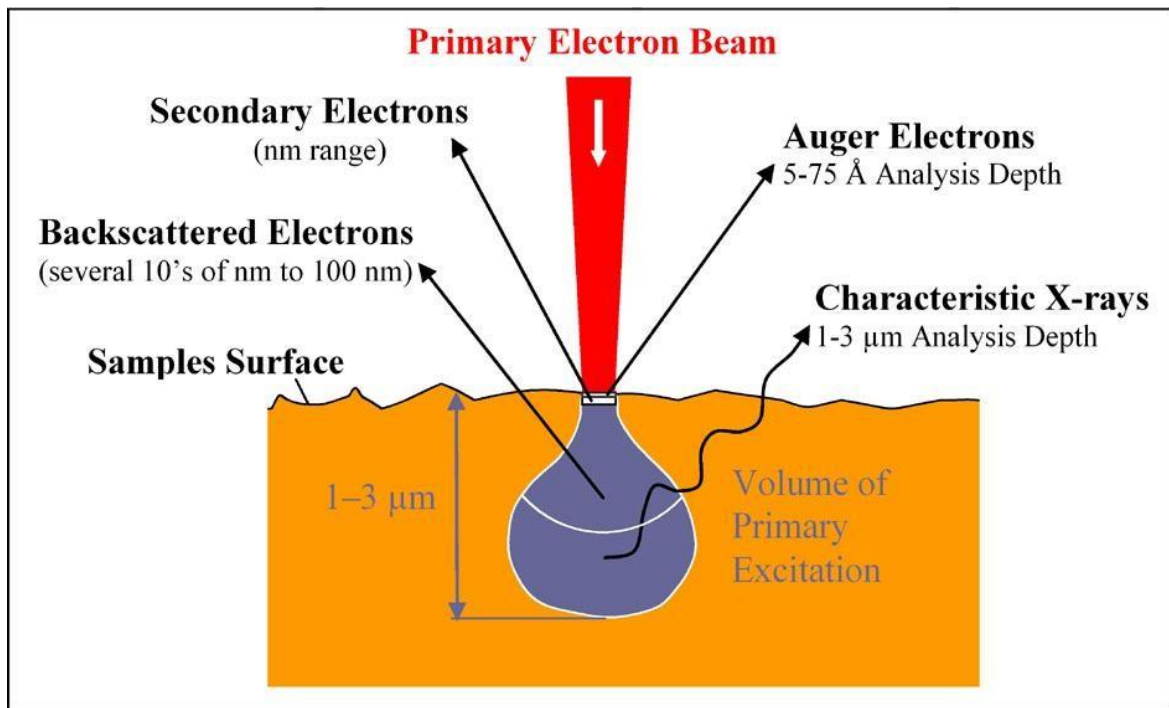


Figure 5: Electron beam – Sample interaction
 (<http://www.capcoat.be/sites/default/files/images/AES-pear.jpg>.)

When the energy of primary electrons are enough to remove electrons from sample atoms, secondary electrons (SE) are emitted (top 10 nm). These electrons are collected by secondary electron detector in the column. Secondary electrons gives contrast according to the topological information about the sample surface (Fultz and Howe, 2002).

Some of the primary electrons collide with the atoms deeper (around 450 nm) in the sample surface and scattered back. These characteristic electrons called backscattered electrons and give contrast according to atomic number of the atom collided with. In the image, areas with higher atomic number is brighter, vice versa. BE detector is needed for detect these electrons.

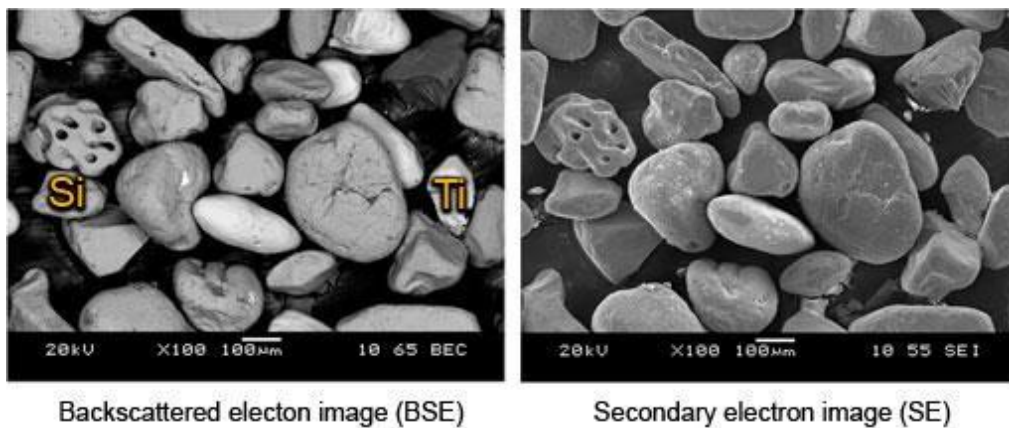


Figure 6: Secondary electron image (SE) and backscattered electron image (BSE) of the same area of a sample.

Formation of characteristic x-rays are another product of the collision between primary electrons and the sample. If an electron in its K, L or M level is excited to a higher level, when going back to its original level, it radiates x-ray within an energy equals to the difference between these levels. These characteristic x-rays are used to determine the elements in any point on the image. This technique is called as Energy Dispersive X-ray Spectroscopy (EDS or EDX). X-rays are emitted from much deeper (1 –3 μm) depths from the surface (Fultz and Howe, 2002).

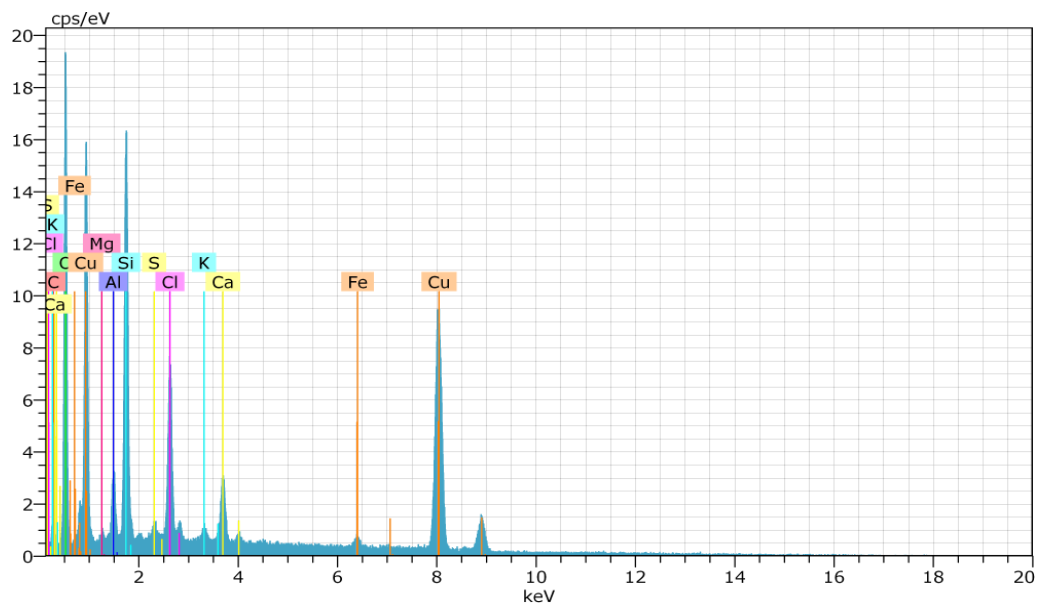


Figure 7: EDS peaks and analysis result of an alloy.

Images may be taken by using x-ray information of each point on the image can also be obtained. This method is called as x-ray mapping.

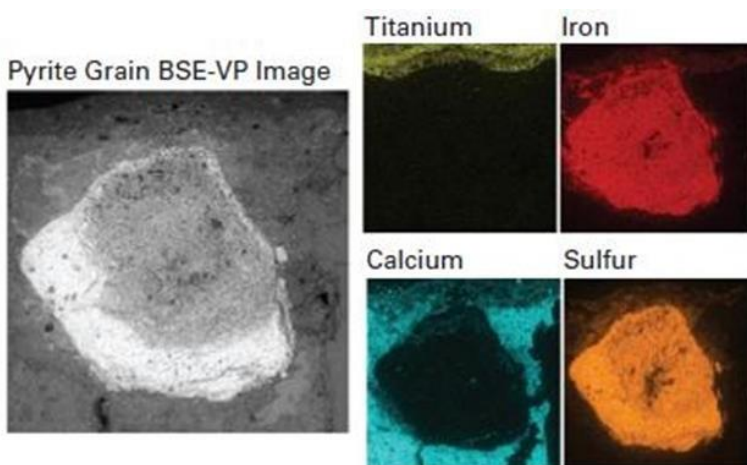


Figure 8: X-ray mapping of a pyrite sample

([https://www.azom.com/images/Article_Images/ImageForArticle_4722\(2\).jpg](https://www.azom.com/images/Article_Images/ImageForArticle_4722(2).jpg))

As the primary electrons accelerated more in the column by acceleration voltage, penetration depth increases; which also means that information obtained comes from deeper volumes of the surface (Fultz and Howe, 2002).

4. MONTE CARLO SIMULATION

MONTE CARLO

First application of Monte Carlo simulation was for nuclear weapon development in Los Alamos in 1940s (Kalos and Whitlock, 2008). It is a probabilistic method for problems with large number of parameters and cannot be solve with analytical methods (Brunetti et al., 2015). Since the first application, simulated results showed progress in the connection with modern computer technology because now it is easier and faster to do multiple calculations in a same amount of time(Kalos and Whitlock, 2008). Even for some authors believe that Monte Carlo is nothing more than rough estimation, still we can have justifiable results.

To understand better and distinguish what can and cannot be done with Monte Carlo it is useful to give a general example. Let's consider a circle and its circumscribed square. The ratios of the area of the circle and square is from $\pi r^2/4r^2$ equals to $\pi/4$. It is probable that the fraction $\pi/4$ of might lie inside the circle, if the points were replaced randomly in the square. If this assumption is true, then one might be able to measure $\pi/4$ by placing a round cake pan with diameter L and square cake pan with side L and collecting rain in both. Also to represent random points in the square and calculate the fraction that lies in the circle, a program can generate the random pairs of Cartesian coordinates. The calculated fraction should be approximately around $\pi/4$ and name as an estimation for $\pi/4$. In 1000000 experiments, it is highly probable (95% chance) that the number of points inside the circle would range between 784 600 and 786 200, yielding estimates of $\pi/4$ that are between 0.7846 and 0.7862, compared with the true value of 0.785398 (Kalos and Whitlock, 2008).

The example showed that random sampling can be used to solve mathematical problem with the defined integral below,

$$I = \int_0^1 \int_0^{\sqrt{1-x^2}} dx \cdot dy$$

The example that defined in the previous paragraph is statistical and related to the laws of chance. In a way Monte Carlo is a drawback to check the accuracy of the answer and to get more accurate answer by repeating the experiments. The determination of the π value can be obtained faster and more precise by non-Monte Carlo methods but Monte Carlo usually is the effective method of integral evaluation (Kalos and Whitlock, 2008).

EDXRF-MC

Every archaeological metallic artefact displays a multilayered structure characterized by the presence of three layers: soil-derived crust, corrosion patina and metal substrate. Monte Carlo (MC) simulation/energy dispersive X-ray fluorescence (EDXRF) spectroscopy combined analytical setup developed to provide the quantitative and reliable information about the layers (Brunetti and Golosio 2014). This methodology was tested on archaeological binary (Cu/Sn) bronze artefacts earlier (Bottaini et al. 2015; Manso et al. 2015; Brunetti et al. 2016; Schiavon et al. 2016). It is, however, the first time that the same combined analytical approach is tested on Cu-alloy (with variable concentrations of impurities) artefacts.

As mentioned earlier, Monte Carlo is a probabilistic technique that can simulate the real phenomenon. For the EDXRF/MC technique, according to the real X-ray source a set of photons was generated and their interaction with the sample material was determined. It is important to have an accurate X-ray source characterization but unfortunately this is not always possible. To overcome this problem a direct measurement of the X-ray emission should be done. In the case of exact match of simulated and experimental spectrum, the composition and structure of the sample can be determined (Bottaini et al., 2017)

To obtain a fast simulation, various variance reduction techniques were introduced, which can simulate and measure the spectrum in a couple of minutes. XRMC and XMI-SIMS were developed to predict the spectral response of EDXRF spectrometers using MC simulations. In this work XRMC software package, which allows user to consider the effect of rough surface, was used (Bottaini et al., 2017).

All the measured XRF spectra were modelled as a two-layered structures: the inner bulk layer and the outer superficial layer formed by the blue-green oxidized corrosion patina.

XRMC is a Monte Carlo program developed by the Bruno Golosio, Tom Schoonjans, Antonio Brunetti, Giovanni Luca Masala and Piernicola Oliva from University of Sassari for accurate simulation of X-ray imaging and spectroscopy experiments in heterogeneous samples. The program is written using C++ and has been tested on different computer operating systems; Linux, Mac OS X and MS Windows.

To run the XRMC, input files (a main input file, a parameter file and some device files) that describe the experimental setup must be prepared. A device doesn't have to be a physical device, the phase array and the sample can be considered as a devices. The title that explains the type and name of the device, a list of commands or variable named and "End" command must be included on every device file. The class of command or name of the variables usually is not important, as long as they are not from the same group (the atomic number and weight percent of the elements in a material). After the each command or variable name, one or more argument should be introduced (real values, integer values or strings, depending on the command).

The main input file

The main input files describes the commands for loading all device files, the command for running the simulation and the command for saving the output in a file. The file creates the device and load the parameters with the command:

- Load *filename*

where *filename* is the name of the device file.

A general setup for X-ray imaging/spectroscopy simulations is written below:

1. a source (*source* device);
2. a spectrum (*spectrum* device);
3. a detector (*detectorarray* device);
4. a sample (*sample* device);
5. a phase (material) composition array (*composition* device);
6. a quadric array (*quadricarray* device);

7. a three-dimensional object geometry description (*geom3d* device).

The order of the “Load” commands is not important. The simulation can be started by the

- Run *devicename*

where *devicename* is the name of the device that controls the acquisition of the simulation results.

The result of the simulation is saved by the command

- Save *devicename dataname filename*

where *devicename* has the same meaning, *dataname* is the name of the data that should be saved, and *filename* is the name of the file used to save the results.

The source file

The current version of the code assumes that the x-ray beam is produced by a point source or by an extended source with a three-dimensional Gaussian distribution. The vector position of the origin \mathbf{r}_s and the orthonormal unit vectors \mathbf{i}_s , \mathbf{j}_s and \mathbf{k}_s , the directions of the local x, y, and z axis, are specified to local coordinate system. Where the local z axis represents the main source direction, the local x and y axes define the beam polarization and angular aperture.

If the θ_s and ϕ_s are the polar and azimuthal angle relative to the source coordinate system. The angular apertures θ_x and θ_y in the x and in the y direction can be specified by the inequality:

$$\theta^2 \leq \theta_x^2 \cos^2 \phi_s + \theta_y^2 \sin^2 \phi_s \quad (\text{I})$$

Within the solid angle limited by this angular aperture, the source intensity distribution is assumed to be uniform.

source device file header

- Newdevice source
- *name* (string)

Commands

- SpectrumName *name*
 - *name* (string): spectrum input device name;
- X *val1 val2 val3*
 - *val1 val2 val3* (real values) source x, y, z coordinates
- uk *val1 val2 val3*
 - source orientation: \mathbf{k}_s components (local z axis direction, i.e. main source direction);
 - *val1 val2 val3* (real values): k_{sx}, k_{sy}, k_{sz}
- ui *val1 val2 val3*
 - source orientation: \mathbf{i}_s components (local x axis direction);
 - *val1 val2 val3* (real values): i_{sx}, i_{sy}, i_{sz}
- Divergence *val1 val2*
 - beam divergence;
 - *val1 val2* (real values): θ_x, θ_y
- Size *val1 val2 val3*
 - Source size; the source is modeled as a three-dimensional Gaussian distribution:
 - *val1 val2 val3* (real values): $\sigma_x, \sigma_y, \sigma_z$;
- Rotate *val1 val2 val3 val4 val5 val6 val7*
 - rotation of the source around the axis passing through \mathbf{x}_0 and with direction

u:

- *val1 val2 val3* (real values): x_0, y_0, z_0 ;
- *val4 val5 val6* (real values): u_0, u_0, u_0 ;
- *val7* (real value) rotation angle θ (degrees);
- End

– End of file.

The spectrum file

The source spectrum is modelled as the sum of two components: a set of discrete lines and a continuous component. The radiation can be unpolarized, partially polarized or totally polarized. The lines can have a Gaussian or a Dirac δ distribution. Each line has its mean energy E_l , its intensity I_l and σ_l . In case of (partially or totally) polarized radiation, the intensity of the two components polarized along the local x and y directions are specified separately for each line.

spectrum device file header

- Newdevice spectrum
- name (string)

Commands

- PolarizedFlag *val*
 - specifies is the beam is polarized;
 - *val* = 0: unpolarized beam;
 - *val* = 1: polarized beam;
- LoopFlag *val*
 - energy extraction method:
 - *val* = 0: extract random energies on the whole spectrum;
 - *val* = 1: loop on all lines and sampling points;
- ContinuousPhotonNum *val*
 - *val* (integer): multiplicity of events for each interval in spectrum;
- LinePhotonNum *val*
 - *val* (integer): multiplicity of events for each line in spectrum;
- RandomEneFlag *val*
 - enable/disable random energy in each interval of the continuous spectrum;

- $val = 0$: random energy disabled;
 - $val = 1$: random energy enabled (recommended);
 - Lines
 - specifies the discrete energy lines of the spectrum;
 - energies and σ are expressed in keV:
 - N_l (integer): Number of lines in the spectrum
 - $E_1 \sigma_1 I_1$ (real values): energy, width (rms) and intensity of the 1st line
 - ...
 - $E_{Nl} \sigma_{Nl} I_{Nl}$ (real values): energy, width (rms) and intensity of the N-th line
 - for polarized beams, or
 - $E_1 \sigma_1 I_{x1} I_{y1}$ (real values): energy, width (rms) and intensities of the two polarization components of the 1st line
 - ...
 - $E_{Nl} \sigma_{Nl} I_{xNl} I_{yNl}$ (real values): energy, width (rms) and intensities of the two polarization components of the N-th line
 - ContinuousSpectrumFile
 - continuous component of the spectrum;
 - N_l (integer): Number sampling points in the continuous spectrum
 - *filename*: name of the file containing the continuous spectrum;
 - in the case of unpolarised beam, the file has the following format:
 - $E_1 I_1$ (real values): energy and intensity of the 1st sampling point
 - ...
 - $E_{Nl} I_{Nl}$ (real values): energy and intensity of the N-th sampling point
 - while for polarized beam it has the following format:
 - $E_1 I_{x1} I_{y1}$ (real values): energy and intensities of the two polarization components
- of the 1st sampling point
- ...

- E_{NI} I_{xNI} I_{yNI} (real values): energy and intensities of the two polarization components of the N-th sampling point
- ContinuousSpectrum
 - same as ContinuousSpectrumFile, but the spectrum is loaded inline rather than from an external file. The *filename* parameter is not used in this case
- Resample *val*
 - *val* = 0: do not resample continuous spectrum;
 - *val* = 1: resample continuous component of the spectrum;
 - If *val* = 1, the following arguments must also be provided:
 - NR (integer): number of resampling points;
 - E_{min} (real): minimum resampling energy (keV);
 - E_{max} (real): maximum resampling energy (keV);
 - End
 - End of file.

The total number of generated events is given by the product of the multiplicities in the spectrum, in the interactions with the sample and in the detector pixels.

The detector file

The XRMC can simulate two-dimensional array detectors with energy binning for each pixel. A single element detector can be simulated as a special case of array detector with only one pixel, which the shape can be defined as rectangular or elliptical. The latter possibility is particularly useful when a round, single element detector has to be simulated. A local coordinate system is associated to the detector, specified by the vector position of its geometric center \mathbf{r}_d and by the orthonormal unit vectors \mathbf{i}_d , \mathbf{j}_d and \mathbf{k}_d . The local z axis is perpendicular to the detector surface, while the local x and y axes are parallel to the detector rows and columns, respectively.

detectorarray device file header:

- Newdevice detectorarray
- *name* (string)

Commands

- SourceName *name*
 - *name* (string): source input device name;
- NPixels *val1 val2*
 - pixel number ($N_x \times N_y$);
 - *val1 val2* (integers): number of columns (N_x) and rows (N_y);
- PixelSize *val1 val2*
 - pixel size ($L_x \times L_y$, cm);
 - *val1 val2* (real values): rectangle sides (L_x, L_y);
- Shape *val*
 - pixel shape:
 - *val* = 0: rectangular;
 - *val* = 1: elliptical;
- dOmegaLim *val*
 - cut on ε (if this entry is 0, then ε is set to the default value 2π);
 - *val* (real value) ε ;
- X *val1 val2 val3*
 - *val1 val2 val3* (real values) detector geometric center coordinates x, y,

z;

- uk *val1 val2 val3*
 - detector orientation: \mathbf{k}_d components (local z axis direction, i.e. normal with respect to the detector surface);
 - *val1 val2 val3* (real values): k_{dx}, k_{dy}, k_{dz}
- ui *val1 val2 val3*
 - detector source orientation: \mathbf{id} components (local x axis direction);

- *val1 val2 val3* (real values): i_{dx}, i_{dy}, i_{dz}
- ExpTime *val*
 - *val* (real value): exposure time (seconds)
- PhotonNum *val*
 - *val* (integer): multiplicity of simulated events per pixel;
- RandomPixelFlag *val*
 - *val* (integer): enable random point on pixels (0/1)
- PoissonFlag *val*
 - *val* (integer): enable Poisson noise on pixel counts (0/1)
- RoundFlag *val*
 - *val* (integer): round pixel counts to integer (0/1)
- HeaderFlag *val*
 - *val* (integer): use header in output file (0/1)
- AsciiFlag *val*
 - *val* (integer): use binary or ascii output file format (0/1)
- Rotate *val1 val2 val3 val4 val5 val6 val7*
 - rotation of the detector around the axis passing through \mathbf{x}_0 and with direction \mathbf{u} :
 - *val1 val2 val3*(real values): x_0, y_0, z_0 ;
 - *val4 val5 val6*(real values): u_x, u_y, u_z ;
 - *val7* (real) rotation angle θ (degrees);
- PixelType *val*
 - Pixel content type:
 - *val* (integer): 0, 1, 2 or 3;
 - 0: fluence;

- 1: energy fluence;
- 2: fluence with energy binning;
- 3: energy fluence with energy binning;

Only if energy binning is used, i.e. if pixel content type is 2 or 3:

- *Emin val*
 - *val* (real): minimum binning energy;
- *Emax val*
 - *val* (real): maximum binning energy;
- *NBins val*
 - *val* (integer): number of energy bins;
- *SaturateEmin val*
 - *val* (integer): saturate energies lower than *Emin* (0/1)
- *SaturateEmax val*
 - *val* (integer): saturate energies greater than *Emax* (0/1)
- End

End of file.

The sample file

When a photon exits from the source, produced by a scattering or fluorescence emission process, its trajectory is characterized by its position \mathbf{r}_{ph} and direction \mathbf{u}_{ph} vector. The XRMC evaluates the intersection of this trajectory with the quadric surfaces delimiting the objects, and divide it in N_s steps with uniform phases. Each step is a segment of the trajectory delimited by its intersection with different objects.

sample device file header

- Newdevice sample

- *name* (string)

Commands

- SourceName *name*
 - *name* (string): source input device name;
- Geom3DName *name*
 - *name* (string): geom3d input device name;
- CompName *name*
 - *name* (string): composition input device name;
- WeightedStepLength *val*
 - setting that determines the algorithm used for the extraction of the next interaction position:
 - *val* = 0 : method 1 described above;
 - *val* = 1: method 2) described above;
- FluorFlag *val*
 - activate Fluorescence (0/1); it can be useful to deactivate it in imaging experiments where fluorescent emission is not relevant, and thereby to save computational time;
- ScattOrderNum N_I
 - N_I (integer): maximum scattering order (0: transmission, 1: first order scattering or fluorescence emission, 2: second order scattering or fluorescence emission, ...)
- M_1
 - multiplicity of simulated events for order 0;
- ...
- M_{N_I}
 - multiplicity of simulated events for order N_I ;
- End

– End of file.

The composition file

The materials that form the sample are called *phases*. A composition file is used to list all the phases and to characterize them by their mass density and by their composition, i.e. the chemical formulas and weight fractions of the compounds that form them. Each phase is assumed to be homogeneous. There is a predefined phase named *Vacuum*, the phase that fill the *universe*, with mass density equal to zero and no elements.

composition file header

- Newdevice composition
- *name* (string)

Commands

- Phase *name*
 - *name* (string): material name; define a new material;
- NCompounds *val*
 - *val* (integer): number of compounds N_c in the phase;
- Compound1 *w1* (string, real): chemical formula and weight percent of the 1st compound;
- ...
- Compound N_c *w N_c* (string, real): chemical formula and weight percent of the N-th compound;
- Rho *val*
 - *val* (real): mass density of the phase (g/cm^3);
- End
 - End of file.

The quadric array file

The sample geometry is described with a set of quadrics that are defined the surfaces of solid objects. A quadric is a surface in the three-dimensional space defined as the locus of zeros of a quadratic polynomial. The general quadric is defined by the algebraic equation

$$\sum_{i=1}^3 a_{ii} x_i^2 + \sum_{i=1}^3 a_{i4} x_i + a_{44} = 0$$

If $x_4 = 1$ defined, then the general quadric may be compactly written in vector and matrix notation as:

$$xAx^T = 0$$

where $x = (x_1, x_2, x_3, x_4)$, x^T the transpose of x (a column vector) and A is a 4 x 4 matrix with A_{ij} for $i, j = 1, \dots, 3$, $A_{4i} = A_{i4} = P_i$ and $A_{44} = R$. The matrix A must be symmetric, thus $A_{ij} = A_{ji}$, $i, j = 1, \dots, 4$.

A quadric divides the space in two regions, one with $xAx^T > 0$, the other with $xAx^T < 0$ called space *outside* the quadric (or *external space*) and space *inside* the quadric (or *internal space*), independently the quadric is closed or not.

quadricarray file header

- Newdevice quadricarray
- *name* (string)

Commands

- Quadric $A_{11} A_{12} A_{13} A_{14} A_{22} A_{23} A_{24} A_{33} A_{34} A_{44}$
 - Generic quadric defined by its elements contents. Since the matrix has to be symmetric, only 10 elements are used.
- Plane $x_0 y_0 z_0 u_x u_y u_z$
 - Plane containing the point (x_0, y_0, z_0) with normal vector (u_x, u_y, u_z) .
- Ellipsoid $x_0 y_0 z_0 R_x R_y R_z$
 - Ellipsoid with principal axis parallel to the main axis, centred in (x_0, y_0, z_0) with semi-axes R_x, R_y, R_z .
- Cylinder $X y z R_y R_z$

– Cylinder having the main axis parallel to the x axis with coordinates y, z on the yz plane, and having elliptical section with semi-axes R_y, R_z .

- CylinderY $x z R_x R_z$

– Cylinder having the main axis parallel to the y axis with coordinates x, z on the xz plane, and having elliptical section with semi-axes R_x, R_z

- CylinderZ $x y R_x R_y$

– Cylinder having the main axis parallel to the z axis with coordinates x, y on the xy plane, and having elliptical section with semi-axes R_x, R_y .

- Translate $\Delta_x \Delta_y \Delta_z$

– Translate the position of the last defined quadric by $(\Delta_x \Delta_y \Delta_z)$.

- Rotate $x_0 y_0 z_0 u_x u_y u_z \theta$

– Rotate the last defined quadric around the axis passing through the point (x_0, y_0, z_0) and directed as (u_x, u_y, u_z) by an angle θ (expressed in degrees).

- TranslateAll $\Delta_x \Delta_y \Delta_z$

– Translate the position of all previously defined quadrics by $(\Delta_x \Delta_y \Delta_z)$.

- RotateAll $x_0 y_0 z_0 u_x u_y u_z \theta$

– Rotate all previously defined quadrics around the axis passing through the point (x_0, y_0, z_0) and directed as (u_x, u_y, u_z) by an angle θ (expressed in degrees).

- End

– End of file.

The three-dimensional object geometry description file

A solid *object* is defined as a solid shape delimited by a set of quadric surfaces that separates the space inside from the space outside it. The quadrics delimiting an object must be properly oriented, in such a way that their normal vectors are directed outward with respect to the object itself.

geom3d device file header

- Newdevice geom3d

- *name* (string)

Commands

- *QArrName name*
 - *name* (string): quadricarray input device name;
- *CompName name*
 - *name* (string): composition input device name;
- *Object name*
 - *name* (string): 3d object name; defines a new object;
- *phase-in-name*
 - name of the phase (material) inside the object;
- *phase-out-name*
 - name of the phase (material) surrounding the object;
- N_q
 - number of quadrics that define the object surface;
- *quadric-name-1 quadric-name-2 ... quadric-name- N_q*
 - names of the quadrics that define the object surface;
- End
 - End of file.

The output file

As default, the output file is saved in raw binary format. The detector bin contents are written in C *double* format (64 bit real).

The total number of entries is:

$$\text{N. of scattering orders} \times \text{N. of energy bins} \times \text{N. of columns} \times \text{N. of rows}$$

with the rows *running faster*.

If the *HeaderFlag* is set to 1 in the detector file, then the bin contents are preceded by a 60- bytes-long header, also in binary format, containing the following information:

- N. of scattering orders (C int format, 32 bit integer)
- N. of columns (C int format, 32 bit integer)
- N. of rows (C int format, 32 bit integer)
- Pixel size S_x (C double format, 64 bit real)
- Pixel size S_y (C double format, 64 bit real)
- Exposure time in sec. (C double format, 64 bit real)
- Pixel content type (C int format, 32 bit integer)
- N. of energy bins (C int format, 32 bit integer)
- Minimum bin energy (C double format, 64 bit real)
- Maximum bin energy (C double format, 64 bit real) (Golosio et al., 2017).

APPENDIX



Figure 1 :M1



Figure 2: M2



Figure 3: M3

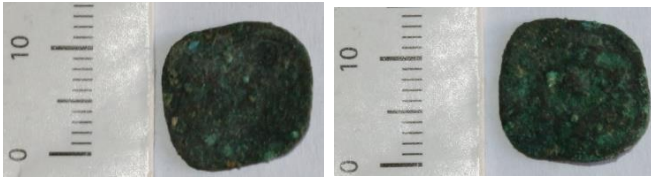


Figure 4: M4



Figure 5: M5



Figure 6: M6



Figure 7: M7

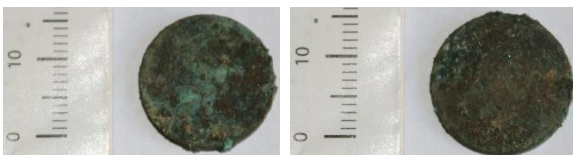


Figure 8: M8



Figure 9: M9

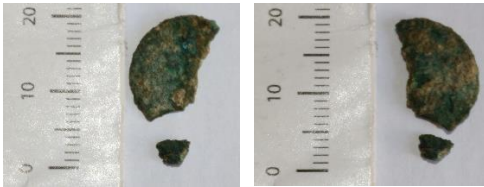


Figure 10: M10

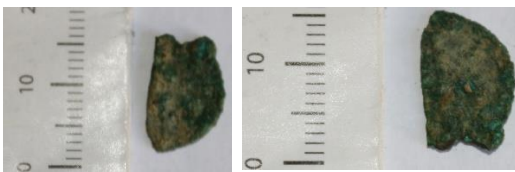


Figure 11: M11



Figure 12: M12

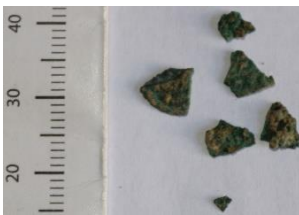


Figure 13: M13



Figure 14: M14



Figure 15: M15



Figure 16: M16



Figure 17: M17



Figure 18: M18



Figure 19: M19



Figure 20: M20



Figure 21: M21



Figure 22: M22

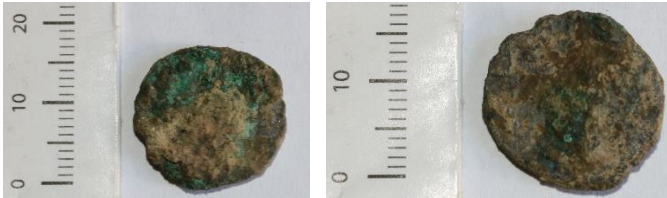


Figure 23: M23



Figure 24: M24



Figure 25: M25



Figure 26: M26



Figure 27: M27



Figure 28: M28



Figure 29: M29



Figure 30: M30



Figure 31: M31



Figure 32: M32



Figure 33: M33



Figure 34: M34



Figure 35: M35



Figure 36: M36



Figure 37: M37